Additive Manufacturing of Liquid Crystal Polymers

Interlayer features:
formation & impact on interlaminar shear strength

Master Thesis

Caroline Houriet

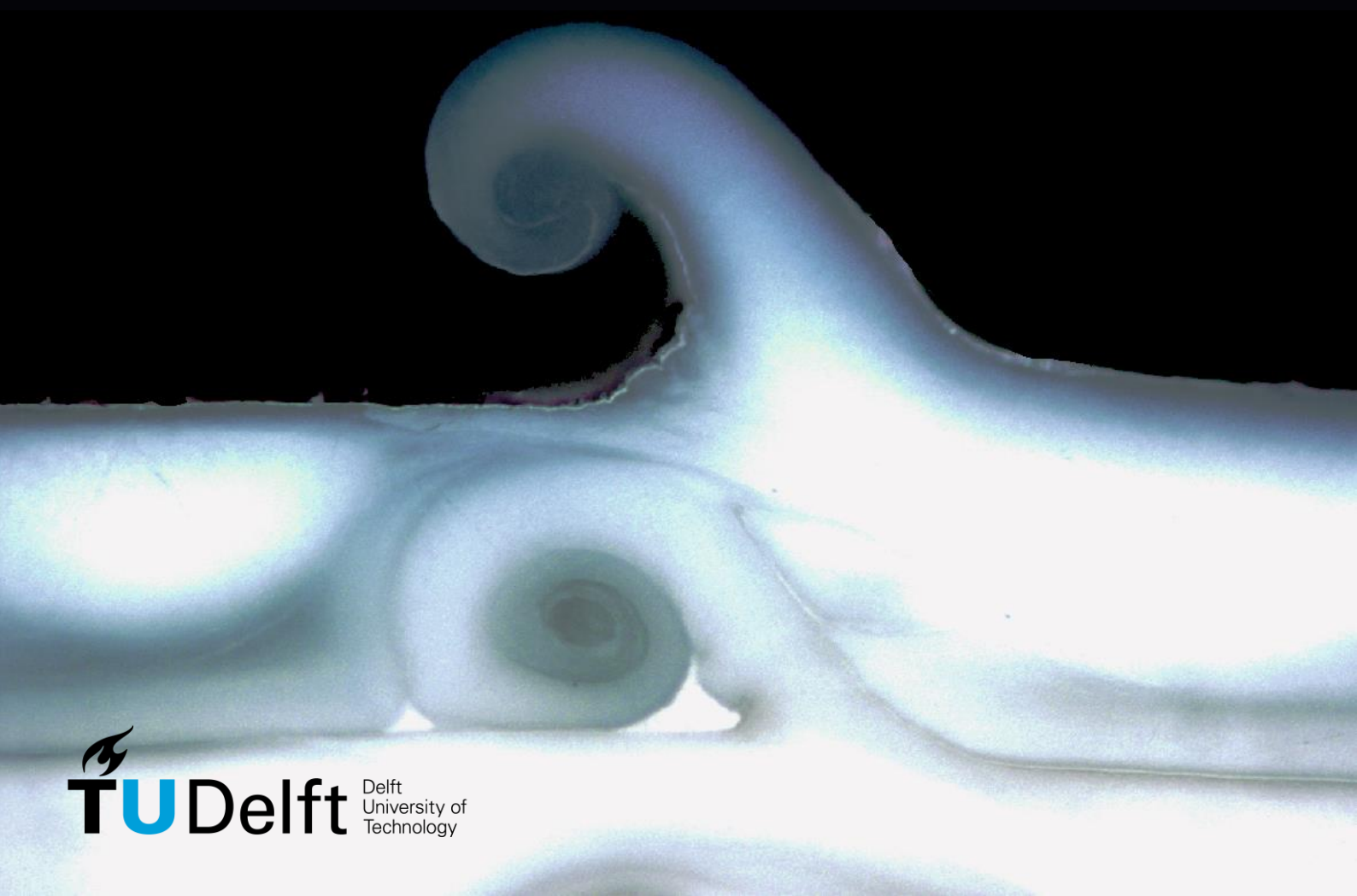

TU Delft Delft University of Technology

Additive Manufacturing of Liquid Crystal Polymers

Interlayer features: formation & impact on interlaminar shear strength

Master Thesis

Caroline C. M. C. A. G. P. Houriet

to obtain the degree of Master of Science
at the Delft University of Technology,
to be defended publicly on Thursday December 19, 2019 at 09:00 AM

Student number: 4748654

Thesis committee:		
	Dr. Calvin D. Rans,	TU Delft, Chair & daily supervisor
	Dr. Clemens A. Dransfeld,	TU Delft, co-supervisor
	Dr. Otto K. Bergsma,	TU Delft, examiner
	Dr. Saullo G.P. Castro,	TU Delft, external examiner

An electronic version of this thesis is available at `http://repository.tudelft.nl/`.

TU Delft

Acknowledgments

With this thesis comes an end to my master at the Delft University of Technology. I would like to express my gratitude to every person who provided their help, insights and time during this thesis. First of all, I would like to thank Calvin Rans, my thesis supervisor, for helping me throughout this work. Thank you for the helpful discussions, and for your enthusiasm and trust. I appreciate that you have given me all the freedom I wanted to explore my interests, while helping me understand along the way how to prioritize and shape a thesis. I would also like to thank Clemens Dransfeld, my co-supervisor, for the great insights he provided, as well as his enthusiasm. But beyond this, I am thankful to my two supervisors for the opportunity they have provided me to start my thesis on such a novel and exciting topic. Throughout my studies, I have never really been able to choose between structures and materials, and in short always found the greatest interest at intersections between concepts. After a bit short of one year working in this field, it is a great feeling to be still convinced that we find ourselves in the right place and time to explore new ideas.

About ideas, I would like to thank Kunal Masania and Silvan Gantenbein for the great ones they had when trying to print liquid crystal polymers. It has shown to be an exciting journey with a lot of new idea waiting to be explored. I look forward to continue this work in the future. I am thankful to them for the helpful discussions throughout my thesis, and for the material help provided, by giving us filaments of Vectra ready to be printed. My thanks also go to Ugo Lafont of the European Space Agency for his enthusiasm and support. This thesis took an unexpected *twist* as the presence of interlayer features was established, but I am convinced that the ideas gathered in the initial phases of this thesis will be implemented in the near future.

Thanks are also due to the DASML team and especially to Gert-Jan Mulder for his enthusiasm and for sharing his experience and knowledge with Fused Deposition Modelling. Thank you also for your help with printing additional polycarbonate parts. Finally, my thanks go to the members of a certain study club who will recognize themselves, and to my friends of TU Delft, aerospace and elsewhere who contributed to make this journey an happy one. I would also like to express my gratitude to my parents, without whom nothing would have been possible. And last but not least, special thanks to Thomas, mon meilleur allié.

Caroline Houriet,
December 5, 2019

Abstract

The emerging field of continuous fiber printing has shown how anisotropy could open up possibilities for topology optimization in additive manufacturing, never before achieved with conventional manufacturing processes. So far, creating anisotropy has been focused on having composites in mind, thus employing dual fiber-matrix systems. The pertinence of this latter point is challenged by liquid crystal polymers. Indeed, these polymers are composed of short, rod-like molecules self-assembling into highly-oriented domains during extrusion, for instance via the nozzle of the printer. These molecules, oriented in the printing direction by the nozzle, confer to the printed part an anisotropy akin to that of composites, without the added processing complexity of a dual matrix/fiber material system. A key challenge for further development, inherent to the anisotropy of the part, is the enhancement of interlaminar properties of printed parts.

In this context, the mesostructure of a liquid crystal polymer (LCP) printed with Fused-Deposition Modelling (FDM) is observed for the first time at the scale of a printed specimen with several layers. The observation of features under the form of regular notches or spiraling patterns named *swirls* is reported on optical microscopy of cross-sections. These features, located between two layers of the print, are referred to as *interlayer features*. A formation mechanism is proposed: interlayer features may be formed as a result of an offset in placement of material, partially obstructing the nozzle each time it is printing a new line. The lack of space for the extruded material may provoke a pressure-build up in molten material, and its flow outwards, resulting in an interlayer feature stemming from an extremity of the nozzle. A body of microscopic evidence is gathered to support this formation mechanism.

Another central question is raised by the observation of the crenelated shapes formed by these interlayer features: by providing mechanical interlocking between layers, they are expected to enhance interlaminar shear strength of a part, A comparative study of interlaminar shear strength is carried via short-beam shear tests. Results indicate that when interlayer features are tall with respect to the layer height, and oriented perpendicular to the shear loading direction, the interlaminar shear strength of the 3D-printed part is enhanced by up to 112%. Microscopic evidence further indicates that these interlayer features may act as crack-arrest. Beyond the improvement in interlaminar shear, two main advantages emerge with this technique: reinforcements are intrinsic to the part printed and thus, no additional step is required for their formation. Furthermore, in contrast to other methods such as annealing, the recyclability potential of the liquid crystal polymer is maintained – which is a crucial feature for its future use in a sustainable industry.

Contents

I

Background

1

Introduction

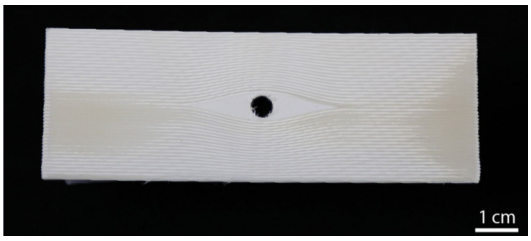

Figure 1.1 – *Directional Open Hole test sample with print lines guided around the hole, in the spirit of a wood knot, to follow the load path within the material under tensile stress. Extracted from (Gantenbein et al., [1])*

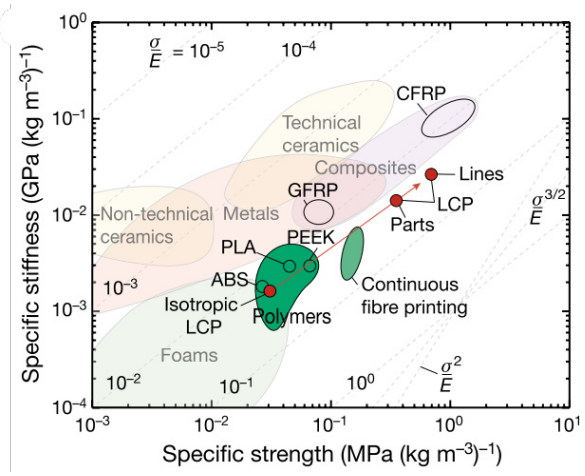

Figure 1.2 – *Ashby diagram indicating the specific stiffness and strength of liquid crystal polymers, tested as printed lines or parts, compared to carbon-fiber reinforced plastics (CFRP), additive manufactured continuous fiber composites and other 3D-printed materials. Extracted from (Gantenbein et al. [1])*

Fused Deposition Modelling (FDM) is a simple, popular and widespread method for the Additive Manufacturing (AM) of polymers, not only among hobbyists but also increasingly aiming at producing engineering components. FDM uses a continuous polymer filament that is fed and molten into an extruder to pass through an extruding hole called nozzle, guiding it onto the print surface. Through successive building up of layers, the 3D objects are fabricated.

The possible range of applications of non-metal additive manufacturing techniques, such as FDM, has been for a time restricted to the hobbyist market or for prototyping purposes, because of the low mechanical properties of materials. Possibilities have however broadened in recent years with the advent of engineering plastics such as PEEK, but also, increasingly, with the rise of the field of additive manufacturing of continuous fiber composites. Anisotropy created by the continuous fibers further increases the possibility of tailoring structures. However, this technology faces multiple challenges often tied to the dual material system, such as printability issues, or poor impregnation between matrix and fibers.

In this context, recent findings by Gantenbein et al. in [1] have highlighted the potential of a 3D-printable high-strength Liquid Crystal Polymer (LCP), whose anisotropy can be fostered for topology optimization intents. Indeed these polymers, neither thermoplastics, nor thermosets, are composed of short, rod-like molecules gathered into so-called *nematic domains* in the same orientation. The domains themselves have different, random orientations. When the material is subjected to shear – for instance along the nozzle wall, through elongational shear flow, or when smeared by the nozzle tip – these oriented domains tend to orient in the same macro-scale direction. As a result, these short molecules, all oriented in the printing direction by the nozzle, confer to the printed part an anisotropy akin to that of composites, without the dual matrix/fiber material system. The properties of this material are inherently determined by the manufacturing process. As a monolithic material, it is readily recyclable, while at the same time benefiting from the same advantages as composites related to the tailoring of structures. The design freedom is all the more enhanced as highly curvilinear "fiber" patterns can

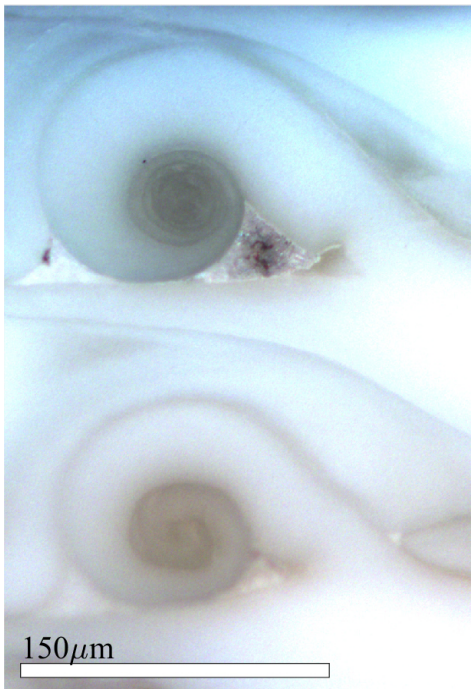

Figure 1.3 – *Longitudinal cross-section of a specimen seen under polarized light, showing two swirls.*

be explored without the constraint of a physical fiber, which must be interrupted and has a certain stiffness.

PROBLEM STATEMENT

In order to unlock the full potential of liquid crystal polymers as 3D-printed materials, a key challenge is the enhancement of interlaminar adhesion. Poor interlaminar adhesion is an issue inherent to 3D printing, linked to the layer-wise approach, but the anisotropy of the material heightens this issue. In this context, a preliminary study of the mesostructure of the LCP printed parts has unraveled the existence of regular features between layers of the print in some conditions. These features are named *interlayer features*. Among these interlayer features appear mainly two kinds: *notches* (Figure 1.5) and *swirls* (Figures 1.3 and 1.4), the difference between them being the presence of a spiraling pattern within the swirl. To the author's knowledge, these features have never been reported in the frame of additive manufacturing. Their presence naturally triggers interrogations on their formation mechanism, and on their potential usefulness as reinforcement for interlaminar shear via mechanical interlocking.

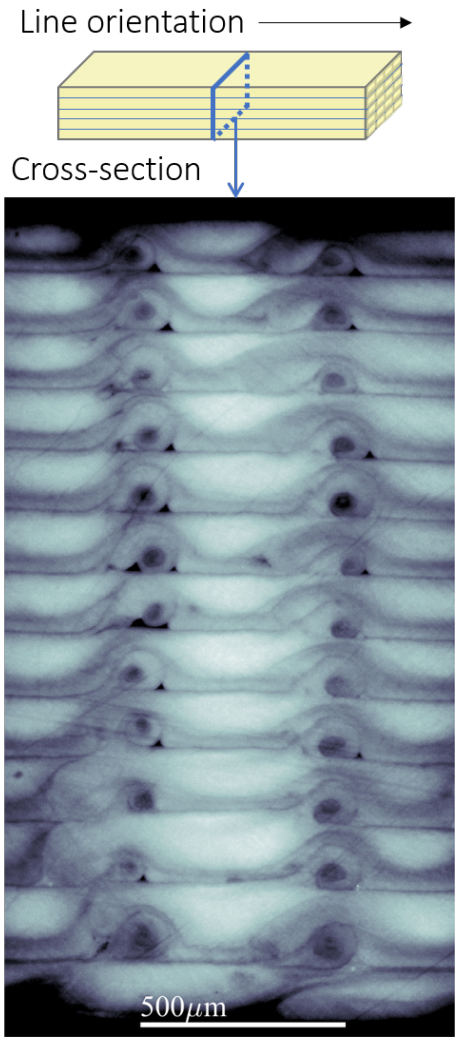

Figure 1.4 – *Longitudinal cross-section of a specimen seen under polarized light. Swirls are always gathered on the same vertical line. Colors have been altered for better visibility.*

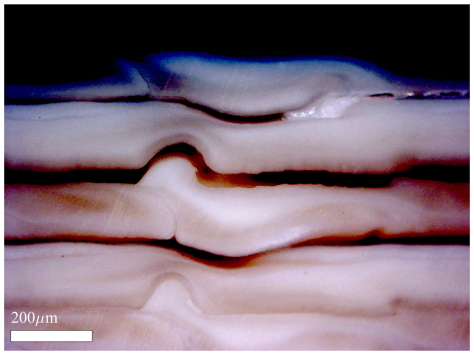

Figure 1.5 – *Micrograph of Sample F85 0.5 090 1 in longitudinal cross-section, seen under polarized light with a ×10 objective. This sample displays notches instead of swirls, also in a semi-circular shape*

2

Literature Study

Outline

The goal of this literature study is two-fold: first, to be a non-exhaustive introduction to thermotropic liquid crystal polymers, which are scarce in the field of aerospace. Second, this literature study is also a dialog between the body of literature, and two works: that of (Gantenbein et al. [1]) in which Vectra was significantly reported as a 3D-printed material for the first time, and secondly, a preliminary work, mentioned in the previous section and presented in Section A, that has brought to light the presence of interlayer features. This dialog has one purpose: through literature, attempt to provide answers for the presence and applications of such interlayer features.

In Section 2.1, the thermal, rheological and mesostructural characteristics of Vectra – the liquid crystal polymer used in this thesis – are discussed. These characteristics have a great importance in Fused Deposition Modelling, but have only been studied in the context of extrusion and injection-moulding. Section 2.2 then shows how 3D-printing of Vectra is part of a broader context carried by the emerging field of 3D-printed continous fiber composites, and faces similar challenges.Preliminary work highlights that the weakness of 3D-printed Vectra lies in its interfaces between beads and layers. Literature shows how this challenge is addressed in other laminated materials. Several remediation methods are presented, including interlocking mechanisms enhancing the interlaminar shear strength of 3D-prints, or composites. These interlocking mechanisms echo with the existence of interlayer features in the 3D-printed Vectra: drawing a parallel with existing successful attempts, they may also act as reinforcing features.

Liquid Crystal Polymers have been showing promise as materials to be 3D-printed using Fused Deposition Modelling (FDM) by a recent study from (Gantenbein et al., [1]). Their potential resides in combining geometrical freedom with molecular orientation, going even beyond the tailored anisotropy of composites. Indeed, mechanical properties are significantly higher in the direction of the print path, enabling the design of complex two-dimensional shapes, for instance following specific load paths, as shown in Figure 1.1.

The anisotropy of this material comes from its liquid-crystalline behaviour: in the melt at rest, rigid molecular segments are organized into ordered, so-called 'nematic' domains: locally, the rod-like molecular chains are aligned in the same direction within the same domain, while globally the orientation of domains is random. However, during extrusion, the shear and elongational stresses tend to align the domains in the direction of the flow (Burghardt et al. [2]). This process is illustrated in Figure 2.9. As a result, the molten material is deposited onto the substrate as oriented in the direction of the nozzle movement, or print path, as shown in Figure 1.1. According to Gantenbein et al. [1], the final skin-core mesostructure is formed as the aligned polymer exits the nozzle and is exposed to colder ambient temperatures: the exterior of the filament solidifies the fastest, with virtually the same high molecular order as in the flow, providing high stiffness and strength. Deeper into the material, cooling is slower, which allows time for molecular relaxation to happen, thus disrupting the molecular alignment and making the core less stiff, as shown in Figure 2.1. This results in a bi-layered mesostructure of the printed filament, presented in Figure 2.6.

In the next section, the main characteristics of the liquid crystal polymer used in this thesis, Vectra, will be presented.

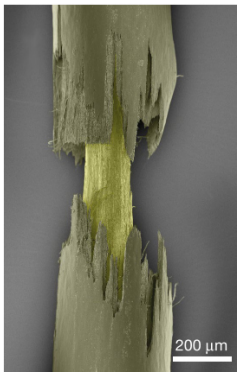

Figure 2.1 – *Skin-core mesostructure of a printed filament seen under scanning electron microscopy with false colors. Extracted from (Gantenbein et al., [1])*

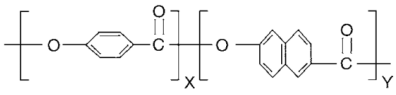

Figure 2.2 – *Chemical backbone of Vectra A950, or HBA/HNA. In the case of Vectra, the rigid monomer is HBA (hydroxybenzoic acid) while HNA (hydroxynaphtoic acid) is the flexible monomer. Extracted from (Chung et al., [5])*

2.1. Description of Vectra

The material under study in the frame of this thesis is Vectra A950, commercially available from Ticona and Hoechst–Celanese. Vectra is a thermotropic liquid crystalline polymer, and as such, the anisotropic behaviour of the material highly depends on environmental conditions. The aim of this part is to provide insight into the internal structure of the additively manufactured LCPs.

Vectra is a copolymer made of two units, HBA (1.4-hydroxybenzoic acid) and HNA (2-hydroxy-6-naphtoic acid), as shown in Figure 2.2. Depending on the grade, the proportion of one to the other is different. As in all commercial LCPs, one of the monomer is considered rigid and imparts high mechanical properties and high temperature capability, while the other, flexible, enhances processibility by lowering the melting temperature. [3, p.423] Focus is drawn on the grade Vectra A950 which is comprised of 73 mol% HBA and 27 mol% HNA. This polymer is a random co-polymer as X-ray diffraction study show. (Chivers et al. [4]). The molar mass of the average repeating unit is 133.5 g/mol. [3]

Vectra is also a thermotropic aromatic copolyester. Thermotropic refers to their liquid crystalline behaviour being triggered by temperature variations, as opposed to lyotropic liquid crystalline polymers such as Kevlar, where the liquid crystalline mesophase is enabled at a certain concentration of material dissolved in solvents (Kwolek et al. [6]).

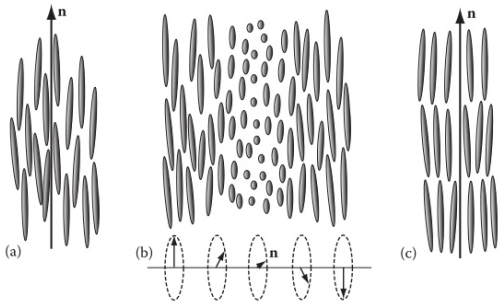

Figure 2.3 – *Liquid Crystallinity can display different molecular orientation types: (a) Nematic, (b) Cholesteric, (c) Smectic, from (Young & Lovell, [3])*

Liquid crystallinity is a state of matter that shows properties of both crystals and liquids. [3, p.421]. In the liquid crystalline phase, liquid crystal polymers can display three different states of order: nematic, cholesteric and smectic, as described in Figure 2.3. The nematic phase is the one displayed by Vectra polymers in the melt. The mesogens, i.e. the parts of the molecule capable of forming the liquid crystalline phase, are aligned imperfectly in one direction and the center of the molecules are arranged randomly. No long-range order exists in the melt at rest, however, within a microscopic volume element called 'domain', the axes of the molecules are oriented in the same direction. In this state, intermolecular forces are sufficiently small to allow molecules to easily slide along each other. [7].

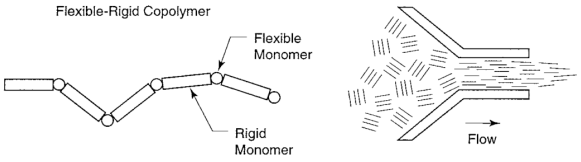

Figure 2.4 – *Liquid crystal polymers have rigid (also called mesogenic) segments which tend to align during flow. Extracted from [7]*

2.1.1. Cristallinity of LCPs

Liquid crystallinity refers to a liquid phase between isotropic melt and solidification where the molecules are ordered in the same direction. The molecular alignment is partially frozen-in on cooling, but this does not mean that the polymer itself will be fully crystalline in its solid state. A portion of the domains

will always rearrange and become amorphous. (Wunderlich & Grebowicz, [8]). A study from (Antipov et al., [9]), describing the 73:27 HBA/HNA, estimates however that the content of crystallinity is lower, with 5-10% in as-spun fibers and 25% in annealed fibers.

Flexible linear macromolecules crystallize from the melt through heterogeneous nucleation, followed by spherulitic, chain-folded crystal growth. The lamellae are organized radially, which effectively means that there is no preferred orientation within the material. However, the rigidity of the molecules of random copolymers like Vectra lead to an impossibility of chain folding. The mesophase transition occurs via aggregation of the rigid chain molecules, with axial orientation and a three-dimensional order. [10, 11] They display an extended chain cristal structure. (Wang et al., [12]). According to (Antipov et al., [9]), Vectra A950 appears to act as a semicrystalline material, where the non-crystalline phase is not amorphous but mesomorphous, identified as an ordered liquid crystalline smectic or nematic state. A summary is offered in Table 2.1, gathering important differences between semi-crystalline, amorphous and liquid crystal polymers.

2.1.2. Thermal Characteristics

A discussion on the different thermal characteristics of Vectra has been carried in a literature study available in Supplementary Data [14].

In (Pisitsak et al., [15]), the heat of fusion of Vectra A950 is reported to be 0.99 J/g, associated to a melting transition at 279°C. As a comparison, the value is closer to 122.5 J/g for fully crystalline PEEK [16], 230 J/g for Nylon6 [17], and 34 to 46 J/g in Poly(Lactic) Acid depending on the processing history [18]. This lower value in Vectra can be explained by the small change in the state of order within the material between solid and liquid, as the melt retains the high orientation of the solid. As a result, compared to semi-crystalline thermoplastics, the energy needed to melt material already close to the transition temperature is from one to 2 orders of magnitude lower. For the same reasons, [13] report that the specific heat (c_p) of Vectra grades is lower than those of semi-crystalline thermoplastics, in the range of amorphous thermoplastics. The thermal conductivity (λ) however, is in the same range as semi-crystallines thermoplastics. As a result, its thermal diffusivity ($\alpha = c_p/\rho\lambda$) does not greatly differ from other commonly 3D-printed polymers.

2.1.3. Rheological characteristics

When solidifying from the nematic melt, thermotropic LCPs (TLCPs) such as Vectra display a hierarchy of structures, which is roughly characterized by two regions: a stiff skin whose molecular orientation is high, and a more flexible core, with less oriented to random molecular order. The formation of this mesostructure is entirely linked to the characteristics of the flow to which the nematic melt is subjected. Beyond the direct effect on mechanical performance (see Section 2.1.4), observations in this thesis are directly tied to the flow history leading to the distribution of material across the cross-section.
TLCPs sometimes display a unique flow behaviour consisting of 3 regions: a shear-thinning plateau at low shear rates, then a Newtonian plateau at intermediate rates and finally shear-thinning again at high shear rates. Shear-thinning is explained by the rigid molecular structure which makes the mesogens orient easily in the shear direction [19]. A consistent rheological study of Vectra A900 is available in (Guskey et al., [20]), covering a wide range of shear flows: dynamic, steady and transient. Although such features adds complexity for the understanding and modelization of the rheological behaviour of TLCPs, it is also a strength allowing them to be used in injection moulding of thin parts such as connectors for computers or miniature connection devices. As reported in [13], it is possible to fill very thin walls down to less than 0.2mm, with lower injection pressures than in amorphous or semi-crystalline resins. From experiments carried by Celanese also in [13, Fig. 3.5.3], Vectra A950 has a melt viscosity of around 170 Pa·s at 280 °C to less than 50 Pa·s at 300°C, at shear rates of 1000/s. Shear rates vary a lot depending on the printing parameters in FDM, depending on the injection speed and the nozzle size, from orders of magnitude of 10/s to 10^3/s. Since the materials are shear-thinning, the viscosity changes as well, for example from 283 Pa · s to 1850 Pa · s for PLA (Poly(Lactic) Acid) between a nozzle diameter of 0.3 mm and one of 2 mm, at fixed flow rate and temperature (Bakrani-Balani et al., [21]).

2.1.4. Mesostructure

As evoked in earlier sections, the nematic behavior of LCP in a liquid state allows the formation of a highly oriented extended chain structure thanks to elongational flow fields triggered during the processing step. Upon solidification, this complex molecular behaviour leads to a complex solid state mesostructure, with various scales of structures, hence the recurring term of 'hierarchical structures' found in lit-

	Amorphous	Semi-cristalline	Liquid Crystal
Melting point	No sharp melting point: softens gradually	Relatively sharp melting point	Melts over a range of temperature with a low heat of fusion
Polymeric chains arrangement	Random in solid and liquid phases	Ordered arrangement and regular crystalline structure in solid phase only	High chain continuity, extremely ordered molecular structure in melt and solid phase
Flow behaviour	Does not flow as easily as SC polymers during molding	Flows easily above melting point	Flows very well under shear within melting range
Examples	ABS, Polycarbonate, PEI	Polyamide (Nylon), PEEK	Vectra LCP

Table 2.1 – *Qualitative comparison of Amorphous, Semi-Crystalline and Liquid Crystal polymers. Adapted from [13, p.37]*

erature [1, 22]. This section aims at describing the mesostructures seen in Vectra, with a focus on dependency with processing technique.

Structural models to divide skin and core

Because of the apparent link between skin-core ratio architecture of TLCPs and fabrication processes, effort have been made in the literature to document the supramolecular structure of melt-processed TLCPs in this respect. An analogy is frequently drawn with conventional short-fiber reinforced thermoplastics, since the mechanical properties of both strongly depend on how the flow-induced orientation developed. (Zülle et al., [23]). A review of the common models proposed has been made in [19] and the relevant ones are presented in this paragraph.

The hierarchical fibrillar model is proposed for drawn fibers by (Sawyer & Jaffe, [24]). The hierarchical order stems from the three different scales of fibrillar structures as can be seen in Figure 2.5. Later on, using field emission scanning electron microscopy in [22], the authors have further detailled the nature of the microfibrillar hierarchy down to 2 nm, with tape-like macrofibrils.

Several other models have been developed in the literature. The hierarchical sheet model is presented by Weng et al. in [25], for an injection-molded bar of HBA/HNA in a 58:42 mol-ratio. It states that the bar is made of three main regions: skin, boundary layer and core. The core is oriented perpendicular to the flow direction, while the skin layer is parallel with it. The skin layer itself is divided in three subregions: a 20 μm-thick top layer, followed by sublayers, each made of microlayers, and then less ordered microlayers. Another model using five distinctive regions, describing a conic flow surface, has been developed for Vectra A950 injection moulded in (Plummer et al., [26]) and (Zülle et al., [23]). Kaito et al. [27] suggest a model for extruded sheets of Vectra A950 having undergone a similar thermal treatment as in (Gantenbein et al., [1]). In a similar manner as (Weng et al., [25]) the authors report 3 main regions: a skin, thinner than 20 μm ; outer layers which account for 80% of the sheet thick-

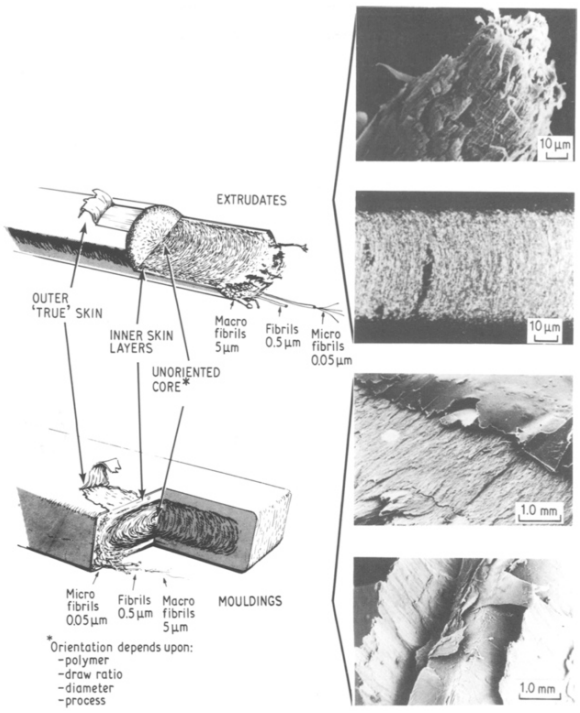

Figure 2.5 – *Selected images from top to bottom: Scanning Electron Microscope and optical micrograph of an extrudate part, Scanning Electron Micrographs of a moulded part. From (Sawyer & Jaffe, [24])*

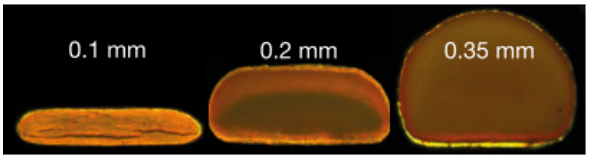

Figure 2.6 – *Polarized Light microscopy of horizontal filaments printed with different layer heights. Extracted from (Gantenbein et al., [1])*

ness, and central layers whose molecular orientation increases with draw-down ratio. Differences between these models can be attributed to the specificity of the flow front between the different samples, as investigated by Liu et al. in [28] or Burghardt et al. in [2].

Figure 2.6 shows the skin-core distribution in additively manufactured Vectra depending on the layer height. Transmitted Polarized Light microscopy allows to see the skin-core distribution as both regions have different optical properties and thus polarize light differently. One can see on the thinnest sample printed with a thickness of 0.1mm, that it is virtually exclusively made of skin, while the thickest sample displays a bright, and very thin outer layer, followed by another, less bright layer, and then a core. The 0.2mm-thick sample also displays similar features, with some asymmetry. These differences are due to a varying exposure to shear caused by the nozzle, and time elapse before full solidification. [1].

Formation of spirals in liquid crystals

In light of the preliminary work described in Chapter A, in which the observation of spiraling patterns are observed in the cross-section, a survey of the literature is carried on the topic of spiral formation in LCPs. A review is carried in [29] on the macroscale mechanical responses, such as bending, bucking or twisting, of liquid crystal polymer networks (LCNs) and liquid crystal elastomers (LCE). These differ from the liquid crystal polymers studied in this work by the amount of cross-links between molecules, between none in the present case, to moderate and high in the other cases. For these materials, appropriate stimuli can generate large changes in order, which itself creates macroscopic shape changes. Sawa et al. [30] work on nematic elastomers, which possess the elastic properties of rubber and the orientational properties of liquid crysals. In their work, they offset the nematic director to the principal axes of a LCN sample to generate shear upon heating, forming an helix, as shown in Figure 2.7. The helix right- or left-handedness is a consequence of the material's chirality. The presence of macroscopic mechanical responses of this order in LCPs has, to the best of the author's knowledge, not

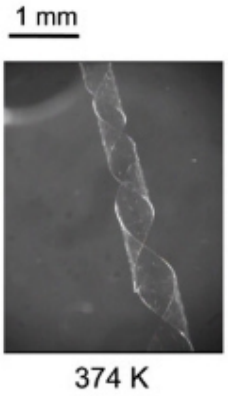

Figure 2.7 – *Spiral ribbons formed by twist-nematic elastomer films. The films are approximately 6–10 mm in length and 0.5–2 mm in width. Extracted from (Sawa et al., [30])*

been reported in the literature. A reason for them not being considered for these applications is that the ΔS, change in entropy on heating, is very low, as suggested by [29], thus no specific change of order triggered by external stimuli has been reported.

Mechanical properties of layers

In some studies, the mechanical properties of the different layers have been investigated in more details. Zülle et al. in [23] studied both Vectra A950 and Vectra A515, the same HBA/HNA ratio with 15 wt% wollastonite, a mineral generally used to disrupt the orientation in TLCPs. The authors performed a study of the mechanical properties of each layer. A stress-strain curve is given for the different layers of the A515 grade. Tensile strength values are given for the skin (0.3mm thick: about 245 MPa), core (1mm thick: around 118 MPa) and whole sample (150 MPa) of Vectra A950. The skin was found to exhibit relatively high tensile strength but a small deformation before failure, while the core showed the exact opposite. This last observation was also confirmed by (Gantenbein et al., [1]) in additively manufactured samples, albeit the skin and core layer properties were not identified. Distribution of Young's modulus and tensile properties of different layers are shown in Figure 2.8. Another study provided a distribution of Young's modulus across the sample distance for injection-moulded samples of Vectra A950 (Plummer et al., [26]), although errors up to 30% are reported between bulk modulus and modulus computed with the rule of mixture from the different layers.

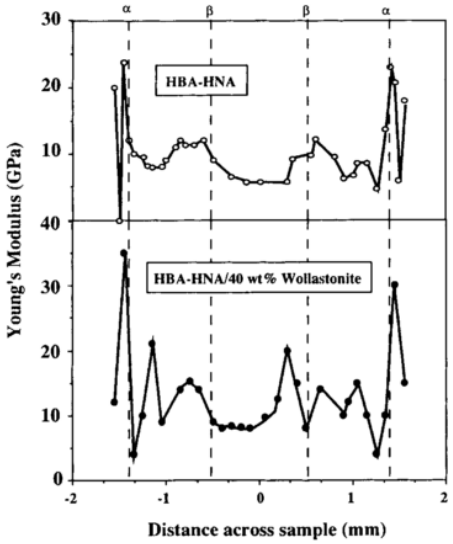

Figure 2.8 – *Modulus profiles for filled and unfilled injection mouldings for Vectra (3x6 mm2 cross-section). The approximate position of the boundaries skin/intermediate region and intermediate region/core are shown by α and β respectively. From Zülle et al. in [23]*

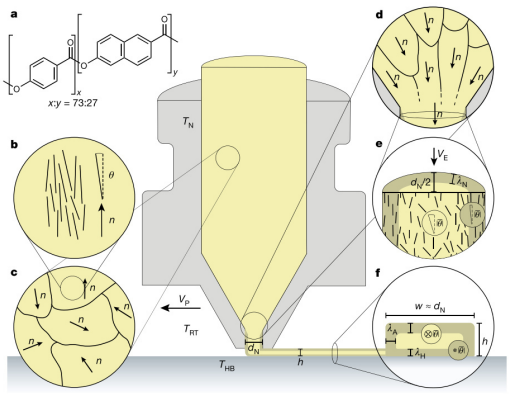

Figure 2.9 – *Schematics of the FDM printing of Vectra. (a) Vectra polymer repeat unit (b) Rigid rods align within the director of a nematic domains, (c) themselves randomly oriented. (d) Elongational and shear forces through the nozzle align the directors (e) (f) Material looses gradually its orientation when extruded, while at the same time solidification freezes the nematic order of the external shell, leading to a skin-core microstructure. Extracted from (Gantenbein et al., [1])*

2.2. Influence of the AM process on mesostructure and strength of printed parts

At the core of design of aerospace structures is the 'trinity' of the interaction between shape design, base material and manufacturing. Each of these aspects are intertwined in order to design a functional lightweight structure. For metals, process has a influence on the end properties of the part, but since metal is isotropic, this influence is limited. The link between material and manufacturing is stronger in composites, since the base material is only made composite by the process, by stacking layers of unidirectional fibers in a way determined by the design step. In additively manufactured liquid crystal polymers, the influence of process becomes even more prominent on the final part, as the material is truly 'created' during the printing, via the skin-core distribution and the print path.

2.2.1. Interaction between process, structure and material in 3D printed LCPs

The same material can be processed in ways which makes its mechanical properties differ by several orders of magnitude. For instance Vectra can be commercialized under the form of a melt-spun fiber, known as Vectran. Vectran is a high strength fiber comparable in yarn tenacity to aramid fibers such as Kevlar, coincidentally another liquid crystal polymer (Cadogan et al., [31]). Although the polymer used is the same, Vectra and Vectran display very different mechanical properties due to different processing techniques. Indeed, Vectran displays a tensile modulus as high as 75 GPa [32], while the highest tensile modulus for Vectra spun fibers so far was 69 GPa. For injection moulded plaques of Vectra, 14 GPa were measured [33], and for FDM parts in the longitudinal direction a maximal value of 6 GPa was reported (Gray et al., [34]). In (Gantenbein et al., [1]), the FDM parts produced with the same material under different process conditions showed a maximum Young's modulus at 34 GPa, with a ultimate tensile strength of 800 MPa, depending on the skin-core ratio established. Figure 2.9 shows how the printing parameters are directly linked to the mesostructure.

2.2.2. Influence of process parameters on interlayer adhesion and interlaminar shear strength

In spite of the large tensile strength reported in the literature, preliminary work in Appendix A highlights how adhesion between layers can be considered poor in the printing setup established (heated bed at 120°C, metallic enclosure around the printer ensuring an

ambient temperature of 30°during the print). In this section, the mechanisms of adhesion in additive manufacturing will first be investigated. A description of techniques to improve interlayer adhesion via heating is carried, followed by techniques improving interlaminar shear strength via mechanical interlocking, having in mind the resemblance they may bear with the shape of interlayer features shown in Figure 6.7.

Classically, bonding between two distinct surfaces can be categorized into three main mechanisms:

- Mechanical interlocking
- Physical attractions due to secondary bonds (e.g. Van der Waals forces, hydrogen bonds)
- Chemical bonding (covalent bonds)

In (Gantenbein et al., [1]), annealing is performed on the Vectra A950 printed parts at 270°C. In this work, bonding is achieved through chemical bonding. Indeed, annealing is reportedly performed in order to establish cross-links between molecules through the esterification between two end chains of the co-polymers 4-hydroxybenzoic acid and 6-hydroxynaphthalene-2-carboxylic acid, as shown in Figure 2.10. If this reaction happens in polymer chains belonging to two distinct layers, this may enhance interlayer adhesion. The authors also study the impact of annealing on strength of the printed LCP filaments, reporting a twofold increase in tensile strength for horizontally printed filaments. Similarly, they report significant improvements for transverse adhesion of printed laminates, such as 100% in tensile strength for 90°laminates. Annealing also changes the fracture mode of the printed laminates, from a disordered mix of distinct broken fibers, to a sharp and clean fracture surface.
While this is an asset for the use of Vectra in demanding conditions, cross-linking greatly undermines its potential as a recyclable material. Indeed, (Gantenbein et al., [1]) compare the melt flow index (MFI) of pristine pellets to that of printed samples and annealed samples. The MFI seems to drop only slightly from pellets to printed samples but decreases significantly after annealing, due to the higher molecular weight achieved through cross-linking. In spite of the gains in mechanical performance, annealing could therefore be an obstacle to recyclability.
In a nutshell, the poor adhesion between layers in 3D printed Vectra is a challenge that may be solved by annealing but at the cost of recyclability. Therefore, other methods to enhance adhesion in 3D printed parts should be investigated.

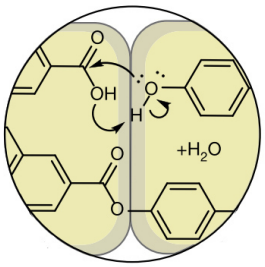

Figure 2.10 – *Esterification reaction between end-groups of polymer chains of two layers creates cross-links and increases molecular weight and stress-transfer between filaments. Extracted from (Gantenbein et al., [1])*

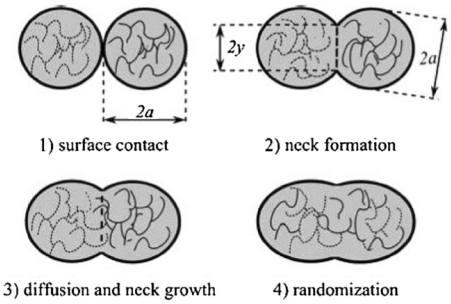

Figure 2.11 – *Polymer sintering process steps during the deposition of two filaments. Extracted from (Turner et al., [36])*

Study of interlayer adhesion in 3D printed parts

As reported in (Duty et al., [35]), poor layer adhesion is a challenge not only met with Vectra but also with any commonly printed material like PLA or ABS. The authors report a drop between ultimate tensile strength in the z-direction and in the longitudinal direction ranging from 25% in large parts to 90% in the case of anisotropic materials such as short fiber-reinforced grades of ABS. As a result, efforts have been carried in the past decade in this respect: on the one hand to understand and model the adhesion between beads during print, which will be the focus of this first paragraph. On the other hand, various remediation methods have been investigated, which will be discussed in the next paragraph.

In the FDM process, the formation of bonds is described in Figure 2.11, where the filaments are seen through their cross-section. The first step of the so-called sintering process is the establishment of interfacial molecular contact by wetting. Motion is then activated towards preferred configurations, and molecules diffuse across the interface, either forming an interfacial zone, or reacting to form primary chemical bonds at the interface. Bellehumeur et al. in [37]

study closely this phenomenon and highlight the importance of cooling conditions. During printing, the estimated order of magnitude for the deposited ABS bead to reach its glass transition is 2 seconds (Sun et al., [38]), which makes the time available for the bond length to develop rather short. More recently, attemps have been made to model the adhesion phenomenon. As highlighted in [39], three aspects have be taken into account in a complete study: thermal exchanges during the deposition step, through convection with the environment and conduction with neighbouring beads and supports ; rheological changes linked to the temperature-dependant molecular processes ; and lastly consequences in mechanical performance. [39], [40] and [41] are examples of such studies, focused on ABS.

In additive manfuacturing of LCPs, the transverse adhesion mechanism is unknown. Since the molecule are rigid chains and not coil-like, it is unknown to what extent they are comparable to ABS which sinters. Especially, the fact that every bead deposited is in contact with the anisotropic skin of its neighbour is likely to limit their intermolecular diffusion, regardless of the nozzle temperature. No published work has been carried so far on the inter- or intra- layer adhesion in 3D printed Vectra.

Remediation approaches

Two main approaches are carried to enhance the interlaminar adhesion in 3D-printed parts: thermal approaches leading to higher mechanical interdiffusion, and mechanical approaches.

Heating approaches for interlayer adhesion

An example of a heating approach is the annealing of Vectra described earlier. In [42] and [43], prior to deposition of material, the location close to the nozzle is heated with a near-Infrared laser above the glass transition of ABS, leading to a 50% enhancement of interlayer bond strength measured with flexural tests. Other approaches focus on statistical evaluation of printing parameters such as nozzle temperature, layer height and bed temperature. The exact measurements differ from one study to another, highlighting the broad meaning of "interlayer adhesion". In [44], Double-Cantilever Beam specimens are used to measure interlayer adhesion via the delamination energy $G_{I,c}$. In [45], the J-integral is extracted from DCB tests to measure interlaminar fracture resistance. Caminero et al. in [46] measure the interlaminar shear strength of 3D-printed carbon-reinforced nylon composites with short beam tests, depending on layer thickness and fiber content. Another radically different approach is used by Sweeney et al. [47]: instead of a variation of printing parameters, a carbon-nanotube coating localized in bead perimeters heats their interface when subjected to microwave radiations, and thus increases the fracture strength of the 3D-printed parts by 275%.

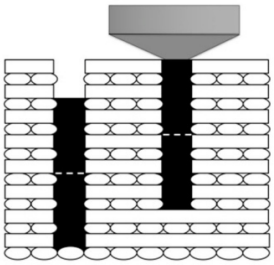

Figure 2.12 – *Schematics of the z-pinning approach applied to Fused Deposition Modelling. PLA is filled inside a hole left during printing, in the z-direction. Extracted from (Duty et al., [35])*

Mechanical approaches for interlaminar shear strength

Improvement of interlaminar strength is a concern that is shared both in composites and additive manufacturing development, thus several remediation approaches in the former may be inspiring for the latter. By mechanical approaches is meant here physical interlocking mechanisms, in contrast to mechanisms occurring at molecular scales discussed above. As shown in [48] where a comprehensive list of examples can be found, interlocking mechanisms are often found in nature as they are firmly linked to the concept of building blocks and hierarchical structures.

In composites, improvement of interlaminar shear strength can be performed by z-pinning, in which pins of a foreign material are inserted through the thickness of a laminate. The same approach is used by Duty et al. [35] applied to Additive manufacturing, as shown in Figure 2.12. In this manner the authors manage to obtain an ultimate tensile strength in the z-direction roughly equal to that in the longitudinal direction. Other approaches, have not been applied to additive manufacturing yet, such as stitching (for instance in [49]), or addition of carbon nanotubes aligned with the z-direction between layers [50].

In a study by Islam et al. ([51]) PLA patterns are printed on pre-preg layers in order to enhance the interlaminar shear strength, as shown in Figure 2.13. Short beam shear tests are conducted on pristine and reinforced laminates. Up to 28.35% improvement in ILSS was reported for laminates reinforced in this manner, compared to the pristine laminate. The delaminations lines are reported to be undulated in the latter compared to the former, which the authors

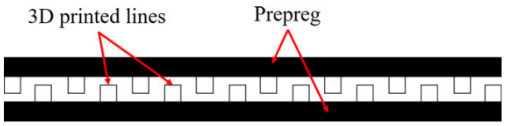

Figure 2.13 – *Cross-section of pre-pregs with 3D-printed interlaminar reinforcement. Extracted from (Islam et al., [51])*

report as an important contributor to the improved ILSS value, due to the higher area of new surfaces formed. The success met with this method indicates that the interlayer features observed and described in Chapter A may also act as a strengthening mechanism for interlaminar shear.

2.3. Conclusion

In this literature study, a dialog has been established between literature and the preliminary observations gathered in Appendix A. In Section 2.1, the characteristics of Vectra essential for a good understanding of its behaviour as a 3D-printed material are presented: among its thermal characteristics, the most significant one is its heat of fusion, one to two orders of magnitude lower than that of other 3D-printed materials. Its rheological characteristics may also make Vectra stand out with respect to other commonly 3D-printed materials. Like PLA or ABS, Vectra displays a shear-thinning behaviour, but technical data available from the manufacturer ([13]) indicates drops in viscosity of several orders of magnitude within shear rates representative of the printing environment.
This literature survey does show the existence of an helix pattern established in liquid crystal polymer networks and elastomers, which belong to a different class than Vectra, a liquid crystal polymer. These helicoidal patterns are triggered by thermal stimuli due to the chirality of the molecules. In contrast, the numerous works on the mesostructure of Vectra do not report the existence of coiling patterns such as those seen in 1.3.
Section 2.2 highlights how the additive manufacturing process influences the mesostructure and the mechanical strength of Vectra, but in light of observations on poor interlaminar adhesion, literature studying this aspect on other 3D-printed materials is reviewed. Indeed, this weakness is inherent to the layer-wise approach. Remediation methods to poor bond strength are first described, but a focus is drawn on methods of improvement of interlaminar shear strength by mechanical interlocking. Similarities are drawn between the interlayer features illustrated in Figure 1.3, and some methods showing increases in performance.

3

Research Definition

3.1. Research Question and Objectives

The existence of a gap in the literature has been identified in the previous chapter. Since interlayer features shown in Figures 1.3 and 1.5 have not been reported in previous works, their peculiar shape calls for the following research questions, which this thesis will attempt to answer. The first one focuses on the cause of their presence, the second one on its consequence:

- How are interlayer features formed during additive manufacturing?
- Can the presence of interlayer features in a 3D-printed part act as reinforcement and enhance interlaminar shear strength?

The research objective is to assess the use of interlayer features as reinforcements in additively-manufactured LCPs by investigating their formation mechanisms in order to control their presence, and subsequently by studying the impact of their presence on interlaminar shear strength of samples, through polarized light microscopy analysis and interlaminar shear strength tests.

3.2. Scope

The conceptual scope of this thesis is defined as the determination of the influence of the presence of interlayer features on interlaminar shear strength of 3D-printed LCP samples. The main parameters varied in this thesis are the orientation of the printed lines, leading to different orientations for the interlayer feature, the pitch between two neighbouring lines, called line width, and the extrusion rate. These parameters are described in more details in Chapter 4.
The experimental scope of this thesis is naturally that in which interlayer features have been described for the first time, in Appendix A. In other words, parameters are chosen for their pertinence in reproducing the interlayer features as described in this preliminary work, and not for the potential higher mechanical performance of samples.

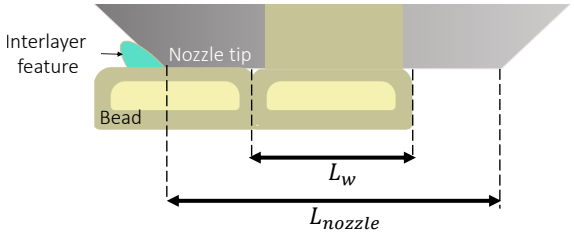

Figure 3.1 – *Schematics illustrating Hypotheses H1: the interlayer feature located on one bead is hypothesized to be formed at the corner tip of the nozzle as it deposits a neighbouring bead.*

3.3. HYPOTHESES

The first set of hypotheses is linked to the first research question, on the formation of interlayer features :

Hypotheses on formation of interlayer features

H1.1 The interlayer features form because the material is over-extruded by the nozzle.

H1.2 Material belonging to a just-deposited line gets molten again as the nozzle passes over it to deposit the neighbouring line. As the new bead is being deposited, it expands against the molten material, pushing it outwards.

H1.3 The exit path for the molten material is situated at one of extremities of the nozzle, which creates a notch in the otherwise flat layer, as illustrated in Figure 3.1.

a) The distance between the interlayer features corresponds to the distance between two lines created by the nozzle, the line width L_w.

b) The location of the nozzle derived from the presence of an interlayer feature on the image also corresponds to the presence of a bead centered with respect to this nozzle position. In other words, the bead pattern on the image should match with that of the nozzle passes indicated by the interlayer features.

These hypotheses will be tested in Chapter 5 and their validity discussed in Chapter 6.

The second set of hypotheses is linked to the second research question, on the potential of interlayer features as reinforcement for interlaminar shear strength :

Hypotheses on interlayer features as reinforcement material

H2.1 The direction of interlayer features with respect to the delamination propagation front determines whether or not the interlaminar shear strength is enhanced.

H2.1a) Interlayer features oriented in the direction parallel to the shear force direction do not enhance the interlaminar shear strength of printed specimens.

H2.1b) Interlayer features oriented in the direction perpendicular to the shear force direction do enhance the interlaminar shear strength of printed specimens.

H2.2 When the two directions are perpendicular, the geometrical characteristics of the interlayer features at the location where delaminations occur may influence the level of increase in interlaminar shear strength.

H2.2a Interlaminar shear strength is highest in samples in which delaminations happen on a 90° layer presenting tall interlayer features with a steep outward slope.

H2.2b In contrast, the influence of interlayer features on interlaminar shear strength does not scale up with their number.

These hypotheses will be tested in Chapter 5 and their validity discussed in Chapter 7.

II

Results

4

Methods

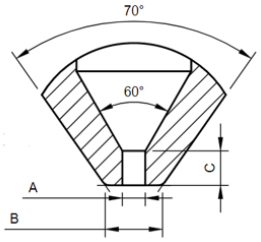

Figure 4.1 – *Manufacturing drawing of the E3D V6 0.4mm nozzle. A = 0.4mm, B = 1mm. Nozzle tip angle is 125°.*

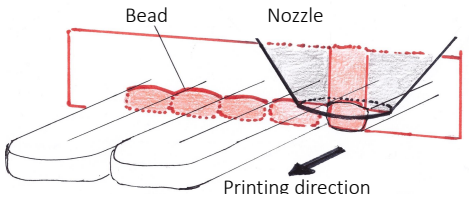

(a) 3D rendition: 3D-printing of an unidirectional infill.

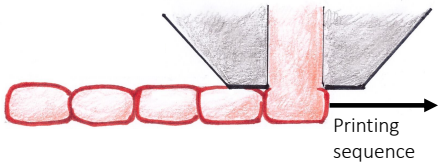

(b) 2D rendition: schematics of the corresponding cross-section, perpendicular to the nozzle movement direction.

Figure 4.2 – *Schematics explaining the movement of a nozzle during FDM, with the corresponding representation of a cross-section in two-dimensions. A line seen in its cross-section is called a bead.*

Introduction

A research methodology is designed to address the two research questions established in the previous chapter: first, how interlayer features are formed during printing, and second, whether their presence enhances the interlaminar shear strength of samples. Samples are printed, then measured for mass and dimensions, and mechanically tested for interlaminar shear. Then, they are prepared for microscopy observation and finally, observed with an optical microscope under polarized light. Cross-sections of the samples give information on the presence or absence of these interlayer features depending on the parameters chosen for the second research question, but also enable to answer the first research question.
In this chapter, a theoretical background is first gathered in order to describe the relevant parameters described throughout this work. Then, the printing facility is presented. A test matrix with the parameters used is then described, along with the corresponding samples, with the settings with which they are printed. The short-beam test method through which they are submitted is presented. Finally, microscopy observation techniques used are described.

4.1. Theoretical background

Throughout this work, several terms common in additive manufacturing will be employed. Among all three-dimensional (3D) manufacturing methods, the one elected is Fused Deposition Modelling (FDM). Fused Deposition Modelling is a 3D printing process in which the filament of a material is fed from a coil into an moving extruder. In this extruder, the filament is molten, and deposited onto the print surface in a pre-defined shape in two dimensions, until the layer is finished. Layer by layer, an object is thus constructed.

The moving extruder consists of two main parts: a cold-end and a hot-end. In the cold-end, the filament is gripped by rollers bearings, driven by a stepper motor according to the amount of material needed for the current extruded line. It is fed into the hot-end, in which it is molten. Temperature is controlled via a thermocouple. The filament can be seen as a plunger, as the volume of filament gripped by the bearing is equal to the amount that flows out. This set-up is presented in Figure 4.5. The metallic part in which the molten material exits the extruder is called the nozzle. The geometry of the nozzle used in this work

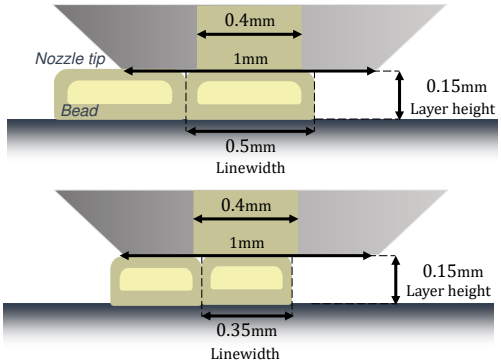

Figure 4.4 – *Difference in bead geometry between setting a 0.5mm linewidth (top) and a 0.35mm linewidth (bottom) in the slicer.*

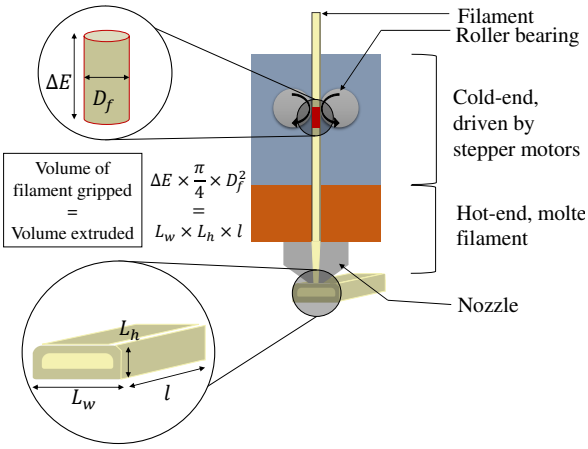

Figure 4.5 – *Schematics of a direct drive extruder. The amount of material extruded during one toolpath is equal to the volume of filament extruded.*

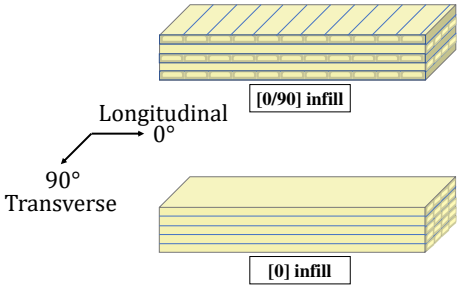

Figure 4.3 – *Two infill types used in this work, with angle convention*

is depicted in Figure 4.1.

In order to print a part, the following workflow is needed: first, the part must be drawn with a Computer Aided Design (CAD) software, for instance CATIA or Solidworks (Dassault Systems). This part can be exported as an .STL file, which contains the surface geometry of the object. Then, this .STL file can be opened in a slicer software. In this work, Cura 4.2.1 (Ultimaker) was used. This software is tasked to convert the 3D-surface described by the .STL file into specific instructions readable by a 3D-printer, called g-code. In order to do this, it splits the object into horizontal layers. Each layer is further split into two main zones: walls and infill. Walls are the printed lines part of the perimeter of the part. In this work, the number of contours making the wall is set to one. The inner part of the print consists of infill, which can have several patterns and densities. In this work, the density is 100%, therefore the part is solid. The infill pattern chosen is made of parallel lines, aligned in a direction called infill direction or infill angle. In this work, two directions are used : [0] and [0/90]. As shown in Figure 4.3, the [0] infill consists of lines oriented longitudinally, while the [0/90] infill is a stacking sequence of longitundinally and transversally oriented lines.

The nozzle hole through which the material is extruded measures 0.4 mm in diameter. However, the width of one printed line does not necessarily equal this value: by varying the amount of material extruded, one can effectively change its width. This width is called line width L_w, and represents the width of a printed line as seen in the cross-section. In this work, two different line widths are used: 0.35mm and 0.5mm. The difference between them is illustrated in Figure 4.4.

The g-code separates the shape to be drawn into a series of toolpaths. As shown in Figure 4.5, for each toolpath, the volume of filament gripped by the roller in the cold-end corresponds to the volume extruded out of the nozzle, with the following relationship:

$$V_{\text{extruded}} = L_w \times L_h \times l \tag{4.1}$$

$$= \Delta E \times \frac{\pi}{4} \times D_f^2, \tag{4.2}$$

where L_h is the layer height, equal to 0.15mm in this work, and l is the length of the line extruded. ΔE is the length of filament gripped by the rollers for this corresponding move, D_f is the diameter of this filament. The filament diameter is therefore a crucial value which must be measured and set in the slicer. Based on this value, the slicer calculates the length of filament ΔE needed to equal the desired V_{extruded} calculated from the geometry of the part, and the line width and layer heights set by the user.

Another parameter is of great importance in this work: the extrusion rate F, also named extrusion percentage, flow rate or flow multiplier in some slicing

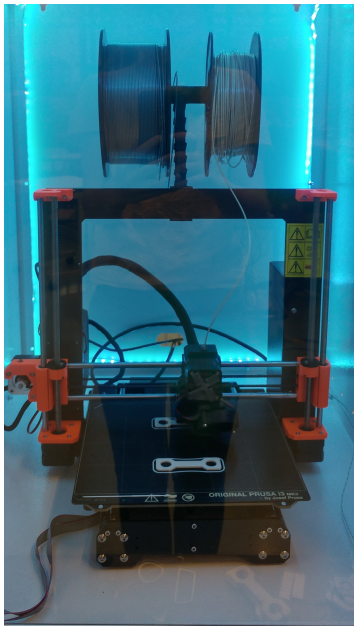

Figure 4.7 – *Prusa i3 MK3S printer in its metallic enclosure*

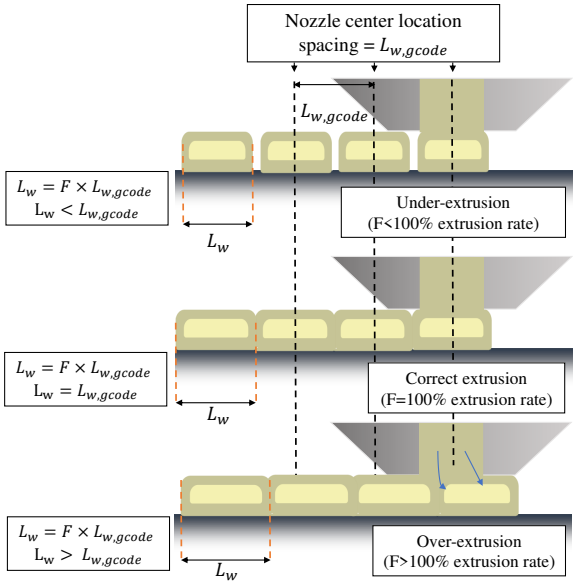

Figure 4.6 – *Underextrusion vs. Overextrusion: impact on linewidth*

software. Normally set to 100%, this setting controls the amount of material extruded V_{extruded}: the effective volume extruded will be $F \times V_{\text{extruded}}$. In the g-code, the length of filament gripped by the rollers for a move will be $F \times \Delta E$. As a result, since $V_{\text{extruded}} = L_w \times L_h \times l$, the line width will be equal to $F \times L_w$. The impact of the extrusion rate on the printed part is illustrated in Figure 4.6. If $F < 100\%$, the part is said "under-extruded", while if $F > 100\%$, it is said "over-extruded.

Other parameters are kept constant throughout this thesis. The layer height especially is kept at 0.15mm, even though best values in stiffness and tensile properties have been reported in [1] for a value of 0.05mm. At such a thin layer height, as already shown in Figure 2.6, highly aligned skin may be found throughout the thickness of a bead, therefore the presence of interlayer features would be more difficult to assess with polarized light microscopy.

4.2. Printing Facility

An open-source FDM Prusa i3 MK3S printer is used in this work. It is built, calibrated and modified: as the printing temperature recommended in [1] is 285°C, modifications are required in order to not damage the printer during long prints. 3D-printed extruder parts, made of PETG are replaced with 3D-printed polycarbonate parts with a higher glass temperature. The thermocouple in the heater cartridge are replaced with a PT100 resistance thermometer. The firmware is updated accordingly, and also updated in order to raise the maximum temperature of the heater bed to temperatures of 120°C (set on the printer) or 90°C (effectively measured with K-type thermocouples). The printer is installed in a metallic enclosure with a front glass, to protect the print from drafts and other perturbations in the thermal environment. A thermometer is installed on the walls of the enclosure near the print bed to measure the ambient temperature. Thanks to the heated bed, temperatures from 28 to 32°C are maintained throughout the print.

As shown in Eq. 4.2, the filament diameter D_f is an important value to provide to the slicing software, as it will determine the correct amount of material needed for extrusion. Commercial filaments display a diameter of 1.75mm or 3mm depending on the printer, with a very good accuracy and circularity. In contrast, the Vectra filament used is an experimental type provided by the authors of [1], which tends to be elliptical. Figure 4.8 represents the diameter of a section of 5.5m of the filament, with data measured every 10cm along its length. For each location, two data points are taken with a hand-caliper: a minor axis a and a major axis b. The equivalent diameter $\sqrt{ab}$ of a circle of the same area is also plotted on this graph. The mean equivalent diameter is found to be 1.81mm, and accordingly set in the slicing software.

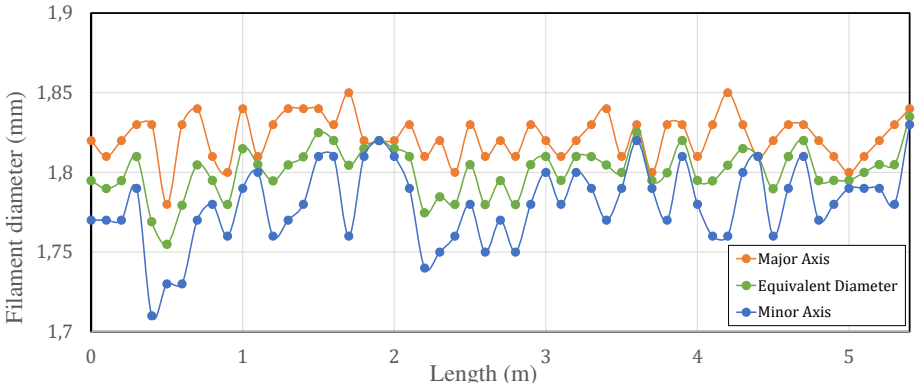

Figure 4.8 – *Measurement of the filament over 5.5m with data every 10cm, showing the variability of its diameter. The average of the equivalent diameter is used throughout this work.*

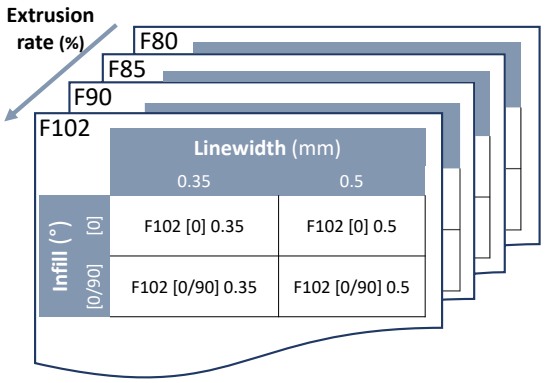

Figure 4.9 – *Schematics of the parameters and nomenclature used throughout this work.*

4.3. Samples description

4.3.1. Test matrix and Nomenclature

As summarized in Figure 4.9, a total of $4 \times 2 \times 2 = 16$ sample configurations are tested, for three types of parameters tested: respectively, extrusion rate, infill pattern and line width. In Table 7.1, the reasoning behind the choice of these parameters is explained in great details.

For each configuration, 5 to 7 samples are printed. For conciseness and clarity, each sample is named in the present work by the sequence of parameters that applies to it, as follows:

$$\overbrace{F80/85/90/102}^{\text{extrusion multiplier (\%)}} \quad \overbrace{0.35/0.5}^{\text{line width (mm)}} \quad \overbrace{0/090}^{\text{infill angle (°)}} \quad \overbrace{[1-7]}^{\text{sample number}}$$

4.3.2. Sample geometry

As shown in Figure 4.10, the targeted dimensions of the specimens are L18×W6×H2.85 mm in the [0/90] configuration (19 layers, balanced symmetric lay-up) and L18×W6×3mm in the [0] configuration (20 layers).

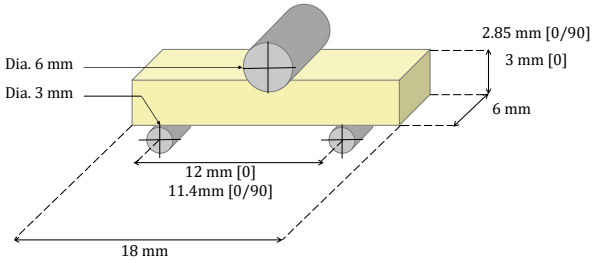

Figure 4.10 – *Dimensioned drawing of the short beam sample according to ASTM D2344 [52] and corresponding 3-point bending fixtures.*

4.3.3. Printing of the specimens

Specimens are printed in the printing setup described in the previous section ,with a bed temperature set to 120°C, and a nozzle temperature at 285°C. The print is started when the enclosed area has reached an ambient temperature of 30°C in its bottom side wall. Print speed is set at 30 mm/s, except the first and second layers which are set respectively to 20 mm/s and 25mm/s. From 3 to 9 parts are printed at once on the bed, one at a time. The layer height is 0.15mm. The hot-end fan runs at 10% capacity. Parts are oriented with their longitudinal dimension along the X-axis of the printer. The infill is set to 100% with 0% overlap with the walls,

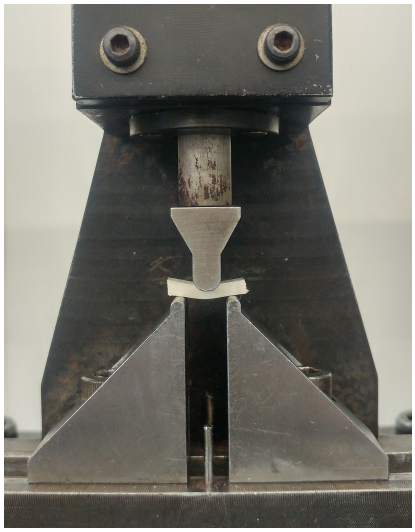

Figure 4.12 – *Specimen in the 3-point bending fixture under test*

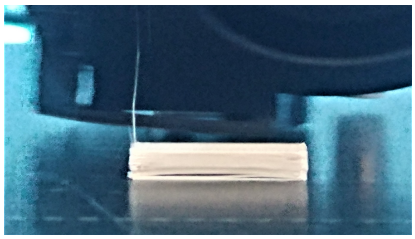

Figure 4.11 – *A specimen showing delamination during print in this manner is discarded.*

which are made of only 1 perimeter. Bed adhesion is enhanced by a fixative spray (Dimafix) triggered by temperature. The uppermost layer of the print is ironed over by the nozzle so that both top and bottom surfaces of the test samples are smooth according to the test standard ASTM D2344 [52].

4.3.4. Specimen inspection

Printing of the specimens is closely monitored. Indeed, for specimens with under-extrusion, delaminations during print are common and inevitable in the current state of the printing setup, due to a poor adhesion between layers. Such delaminations are linked to the thermal gradients between the print bed and the environment, and the coefficient of thermal expansion of Vectra. The latter being negative and close to 0, specimens can sometimes still continue to be printed after the parts have delaminated as they do not necessarily detach from the bed. Delaminations tend to occur in the first layers, except the first one. Indeed, adhesion between the print bed and the first layer is high thanks to the fixative spray.

A quality criterion is applied to assess the viability of each specimen: if a delamination can be noticed in the middle of the print, as for instance in Figure 4.11, the print is aborted and the specimen discarded. If the specimen is fully printed, but delaminates in the first to fourth layer as it is removed from the print bed, it is not discarded, but the number of layers that have been removed is recorded. If a delamination can be seen above layer 5, the specimen is discarded.

As a result, every specimen has a different thickness, with the difference linked to the delaminations that have occurred in manufacturing. The thickness, width and length of each specimen is measured in 3 different points with a hand digital caliper. The mass of each specimen is also measured using a precision Toledo scale.

4.4. Short-beam test method

All samples are tested according to ASTM Standard D2344 [52], *Standard Test Method for Short-Beam Strength of Polymer Matrix Composite Materials and Their Laminates*. This standard leads to the calculation of a short beam strength, which is the apparent interlaminar shear strength of a sample.

A schematics of the load case and shear load diagram can be found in Figure 4.13. Via three-point bending, a short beam is submitted to shear stresses with opposite signs in its left and right sides. According to the ASTM D2344 standard, the short beam strength is

$$F_{SBS} = 0.75 \times \frac{P_m}{b \times h} \tag{4.3}$$

where b is the width, h is the height of each specimen. P_m is the maximum load experienced during the test, which, according to the standard, should be stopped when one of the following criteria is met: a load drop-off of 30%, two-piece specimen failure, or cross-head travel exceeding the specimen thickness (in this case, approximately 3 mm). For the purpose of this test however, the test is stopped when cross-head travel exceeds 1 mm, or 60% load drop-off.

Specimens are tested on the 20-kN universal test machine (Zwick) of the DASML Laboratory, with the corresponding 3-point bending fixture in which side supports diameters are 3mm, and center load introduction head is 6mm in diameter. A picture of a specimen during test can be found in Figure 4.12. The span is adjusted according to the thickness of the specimens in agreement with the standard, with a precision of ±0.3mm, as shown in Figure 4.10.

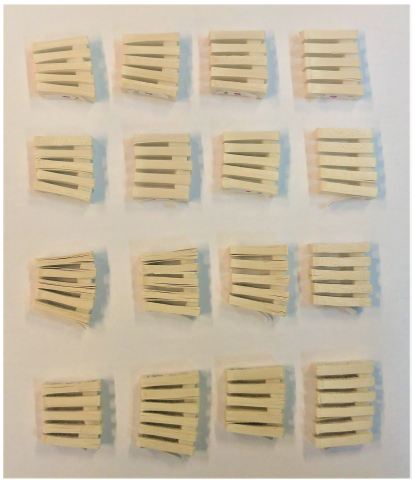

Figure 4.15 – *Short beam test specimens ready to be potted prior to grinding on their longitudinal cross-section*

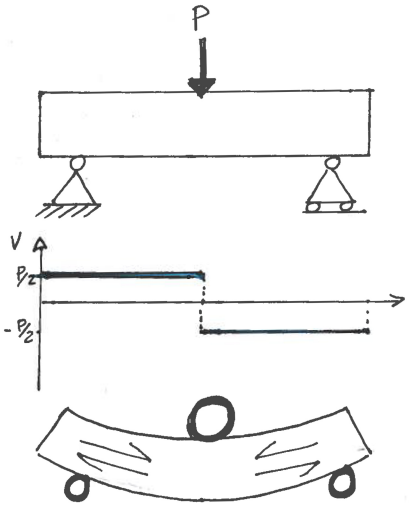

Figure 4.13 – *From top to bottom: short beam shear test load case, shear load diagram, deformed shape with expected shear resultants.*

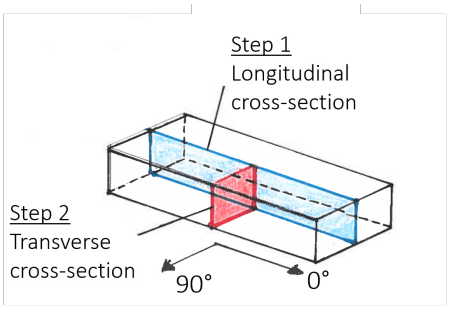

Figure 4.14 – *Representation of the cross-sections observed on every specimen.*

4.5. Microscopy

For each specimen, gathering data of the mesostructure of the specimen is performed both in the longitudinal and transverse cross-section (see Figure 4.14), as on both sides, delaminations and distribution of interlayer features are informative. However, the microscopy methods available are destructive as specimens should be cut in half to reveal their mid-section. The following workflow has been developed to gather this data for each sample.

4.5.1. Workflow

After having been subjected to short beam shear tests, the specimens are potted in resin. Indeed, specimen cannot be sawed or cut without risking to damage them as this step has shown to trigger or propagate delaminations. As a result, all specimens, as shown in Figure 4.15, are potted in an optically transparent epoxy resin with a curing time of 12 hours and a low coefficient of thermal expansion.

Once embedded in resin along their longitudinal side, the specimens are then grinded off about 3mm with the grinding steps described below in order to observe the longitudinal cross-section at half the width of the specimen.

In order to observe the transverse cross-section of the same specimens, the samples, which are still enclosed in resin, are cut in half with the resin using a sawing machine, a diamond blade at 4000 rpm with water. One of the resulting half cylinders is potted again in fast-curing resin, grinded in the same manner so that the cross-section is situated at about half the length of the specimen, and observed with the same method under the optical microscope. The two different cross-sections that are observed are illustrated in Figure 4.14.

4.5.2. Grinding method

Before each microscopy observation, samples are grinded using a Tegramin 20 grinding machine, in a batch of 2 or 4 sample holders per row. The grinding method is the following:

- SiC Foil 500 with water for 1:30min
- SiC Foil 1000 with water for 1:10min
- SiC Foil 2000 with water for 1:30min
- SiC Foil 4000 with water for 2:00min
- SiC Foil 4000 with water for 2:00min, once more

Between each step, the specimens are cleaned under running water and dried with compressed air, and the grinding foil is changed. Since specimens should be grinded up to their center, the amount of material grinded is measured after each step with a caliper, and

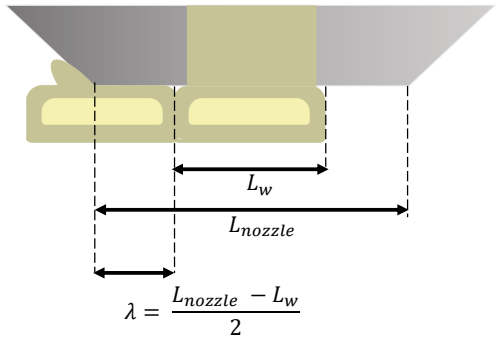

Figure 4.16 – *Schematics of important lengths used throughout this paragraph. λ is the distance between a swirl and the start of the bead generated by the corresponding nozzle movement.*

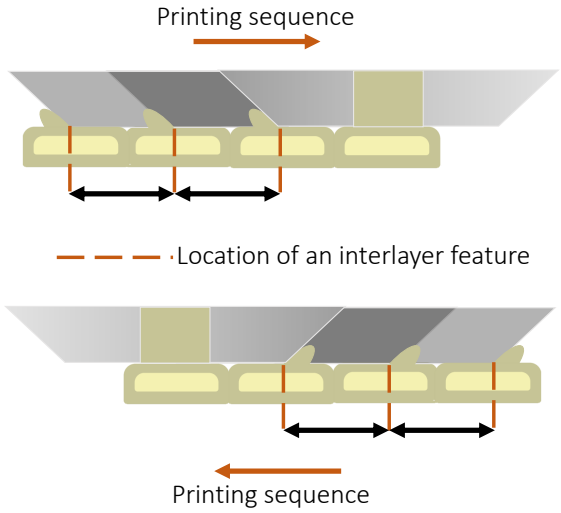

Figure 4.17 – *Consequence of the printing sequence on the location of a swirl: its root can be in opposite direction. The user manually points the location of these interlayer features at the corner where the nozzle has passed.*

the third step is prolonged if needed until the center is reached. Before microscopy observation, the sample surfaces are cleaned with ethanol.

4.5.3. Specimen observation

Observation of specimens is performed with a Leica DM100 optical microscope mounted with a polarizer and an analyzer. The analyzer is set at 90°in order to observe the specimen under polarized light. The resulting image is captured onto a Axio Zeiss CCD camera in colors. Variations in color tones are artifacts due to different automatic white balance levels.
For the longitudinal cross-section, about 5 to 7 frames are taken to cover the whole length of the specimen with a ×2.5 objective. These frames are then stitched using Photoshop (Adobe).

4.6. Image Analysis

An analysis of the micrographs is carried in two phases, each separately verifying an aspect of the hypotheses on the formation of an interlayer feature. What they respectively attempt to verify, along with the method employed, is described in this section:

Phase 1 – In order to evaluate the hypothesis stating that the swirls are created by the side of the nozzle when it passes onto already-deposited material, the swirl location data can be compared to known features of the print. Hypothesis *H1.2a* is tested.
Distances between these features are calculated and plotted for every sample. According to the hypothesis, since they are generated by nozzle paths, the interlayer features should be spread apart by the same distances that separated two nozzle paths, i.e., by the distance of one linewidth L_w.

Phase 2 – The known nozzle geometry can be used to retrieve, for each swirl, the corresponding nozzle movement that created it, and the bead that was deposited by it at the same time. The corresponding bead that should have been deposited if the interlayer feature was created by a nozzle movement can be overlapped with the picture, and should match with the experimental position of a bead. This is hypothesis *H1.3b*.
According to this hypothesis, the distance λ between the side of a swirl at a location x_S and the nearest boundary of a bead at a location x_B should be:

$$\lambda = x_S - x_B = \frac{L_{\text{nozzle}} - L_w}{2}, \tag{4.4}$$

where L_{nozzle} is the width of the nozzle flat side, taken from the manufacturing drawing as 1 mm (see Figure 4.1), and L_w is the width of a bead, which is equal to the linewidth set in the g-code. Therefore, the hypothesized bead can be located at a distance determined by Eq. (4.4) to the spotted interlayer location, with a width of the linewidth. This is a way of testing hypothesis *H1.3b*: the bead pattern on the image should match with that of the nozzle passes indicated by the swirls.

Micrographs are exploited with Matlab (Mathworks), for which a processing script is written. The user manually points the location of the interlayer feature on the image. Since interlayer features tend to align along a vertical line on the micrograph, only one point is asked from the user for each column of interlayer feature. Since interlayer features have a certain width, the pointing is performed in a consistent manner to avoid scatter. As illustrated by Figure 4.17, the

pointed coordinate corresponds to that of the root of a swirl, or, as the hypothesis *H1.3* states, to that of the tip of the nozzle:

- the right corner angle of the interlayer feature if printing sequence goes from left to right on the image,
- the left corner angle of the interlayer feature if printing sequence goes from right to left on the image.

5

Results

INTRODUCTION

This chapter gathers experimental results, divided into four sections: microscopy observation, in which the observations are presented, subsequent image analysis, macroscopic observations, and finally mechanical tests. For each section, the hypotheses tested will be recalled briefly, and rephrased in a quantifiable manner when possible or needed. However, the philosophy of the test, such as the reasoning behind the parameters changed, is described in much more details in the two following chapters: Chapter 6 in which the question of the formation of interlayer features is addressed by using Sections 5.1 to 5.3, and Chapter 7 in which the improvement in interlaminar shear through the presence of interlayer features is discussed with the results gathered in Sections 5.1 and 5.4.

5.1. MICROSCOPY OBSERVATION

Microscopy observations enable to see the cross-section of samples which have been mechanically tested. The interest in these observations is two-fold: first, the distribution of material can help understand how it was deposited, and thus give elements of answer to the first research question established, on the formation of interlayer features. Second, the location of delaminations can be spotted on the images, and also give insight on the behaviour of the part subjected to the shear loading, especially regarding whether interlayer features behave as crack-arrest features. As such, this microscopic data is the base on which most hypotheses gathered in Chapter 3 are tested.

However, the data available is consequent, as in total 174 micrographs are taken from the totality of the 87 short-beam tests samples. This calls for several levels of visibility and synthesis of this data. For the reader's convenience, three possible ways of viewing it are available through this thesis:

- Raw data consisting of the 174 micrographs taken from the totality of the 87 short-beam tests samples, available through a Supplementary Data [14] (online),
- Text description of images by configuration: available in the appendix in Sections C.1.1 and C.1.2
- Selection of four images representative of the trends that can be spotted, shown in this section. They are found in Figure 5.1.

From these images, three observations are made in relation to Hypothesis *H1.1*: *"The interlayer features form because the material is over-extruded by the nozzle"*. This hypothesis can be tested by simply comparing the presence of interlayer features in samples with under-extrusion (F < 100%) and samples with over-extrusion (F> 100%), relative to the F = 100% extrusion rate derived from the measured diameter of the Vectra filament used, as described in Chapter 4.

5.1.1. Interlayer features in under-extruded samples

As represented in Figure 5.1, or more systematically in Supplementary Data [14], a general trend can be noticed: within one sample configuration (e.g.: 0.5mm linewidth, 0° infill) interlayer features are more numerous and systematic with increasing extrusion rates.

However, according to Hypothesis H1.1, one should be able to notice interlayer features only in the over-extruded sample type. As shown in Figure 5.1, this is not verified for samples with a 0° infill: interlayer features can be seen at varying degrees even on the lowest extruded samples (F80, Figure 5.1a). A striking common point in the 3 under-extruded samples represented is the sharp separation between two zones. On the first bottom layers, under-extrusion is noticeable, which is expected. It is also expected that the void content decreases between F80 (Figure 5.1a) and F90 (Figure 5.1c). However, it is not expected that in these 3 cases, a sharp transition occurs, leading to a zone in which no gap between beads can be seen. In this upper zone, interlayer features can be noticed, either as notches of varying heights in F80, or as regular swirls in F85 and F90 samples. Their presence is also accompanied by what appears to be a shift in the bead distribution with respect to the under-extruded zone. This point is also addressed in the Appendix, Section B.3.

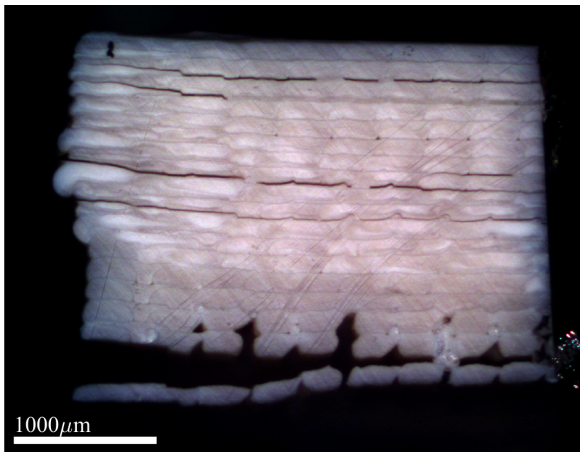

(a) F80 0.35 0 3

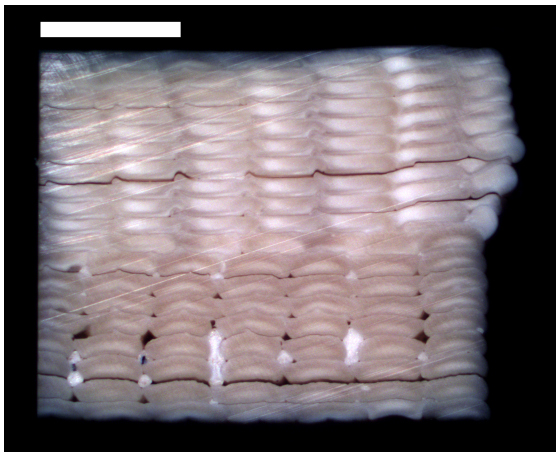

(b) F85 0.5 0 1

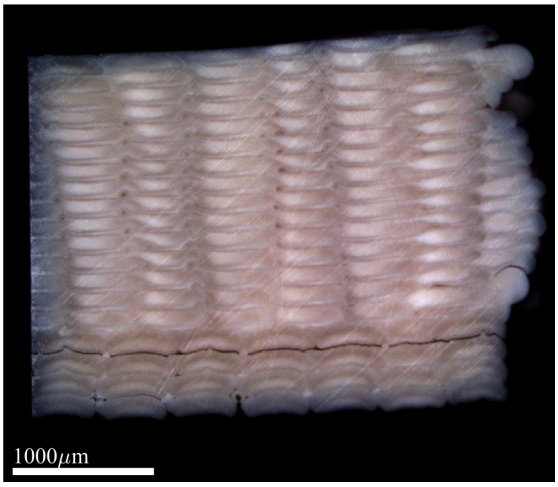

(c) F90 0.5 0 4

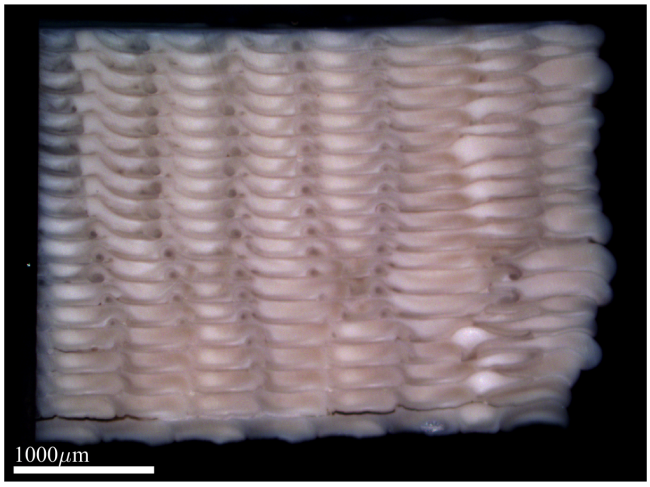

(d) F102 0.5 0 6

Figure 5.1 – *Micrographs of a sub-selection of short-beam tests samples. Scalebar is 1 mm. These cross-sections are representative of each sample configuration. F80 (a), F85 (b) and F90 (c) are all samples which should display under-extrusion, indicated by voids and gaps between beads. Indeed, this seems to be the case, but only for the first layers. A transition happens in these three cases in upper layers, beyond which interlayer features can also be seen. The only true over-extruded sample is F102 (d). This sample displays fully formed swirls, which, in contrast to the other samples represented, grow with increasing layer height.*

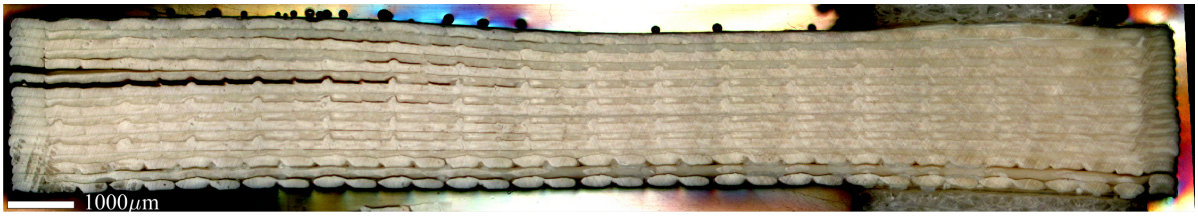

(a) F85 0.5 090 4

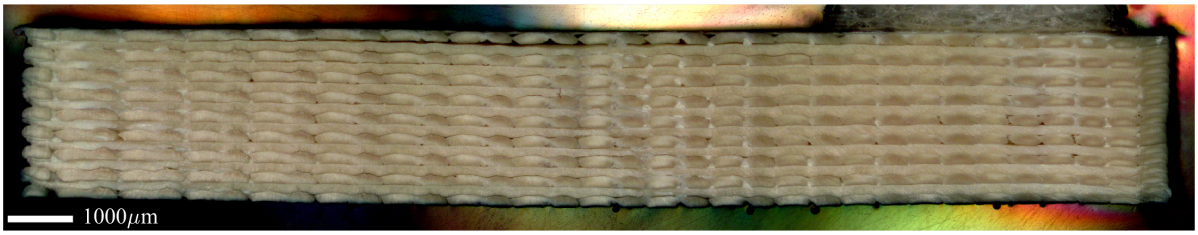

(b) F85 0.5 090 6

Figure 5.2 – *Micrographs of longitudinal cross-section of samples.*

5.1.2. Evolution of swirl geometry in over-extruded samples

In contrast to the under-extruded cases, the F102 unidirectional samples feature swirls which increase in size with higher layers. For instance, Figure 5.4a show a sample which has been printed with 102% extrusion rate and an unidirectional infill. The swirl pattern evolves with the layer height. This can also be seen in Figure 5.1d, a close-up of which is available in Figure 5.3 highlighting this remark. The volume of material gathered in a swirl seems to increases from bottom to top layers, altering its geometry in the following way:

- While the starting corner, that of the nozzle tip location according to Hypothesis *H1.3*, does not move, the center of the swirl is further pushed towards the start of the print sequence. The horizontal distance between two swirl centers (a tall one in the upper layers, and a small one in the lower layers) in Figure 5.3 is up to 0.2mm. This is why, in Section 5.2, the swirls locations are pointed at the root of small notches or swirls rather than tall ones, to avoid errors.
- The height of a swirl gradually increases, until it is as tall as a layer height: as it grows in diameter, the top of the swirl is cropped by the nozzle upon its passage, taking away more material.

Only unidirectional infills are shown in Figure 5.1. Interlayer features can also be seen in the other infill direction, [0/90]. For this configuration, the same general trends holds - i.e. interlayer features are increasingly found with higher extrusion rate. However, a difference is noted for over-extruded samples in Figures 5.4a and 5.4b. Two specimens are shown, which have been printed with same parameters except for the infill, set at [0] for the former and [0/90] for the latter. It is noticed that for the former, interlayer features grow, become taller and taller as the layers are printed, in the manner described in the previous paragraph, while for the latter, their size remains constant throughout the print.

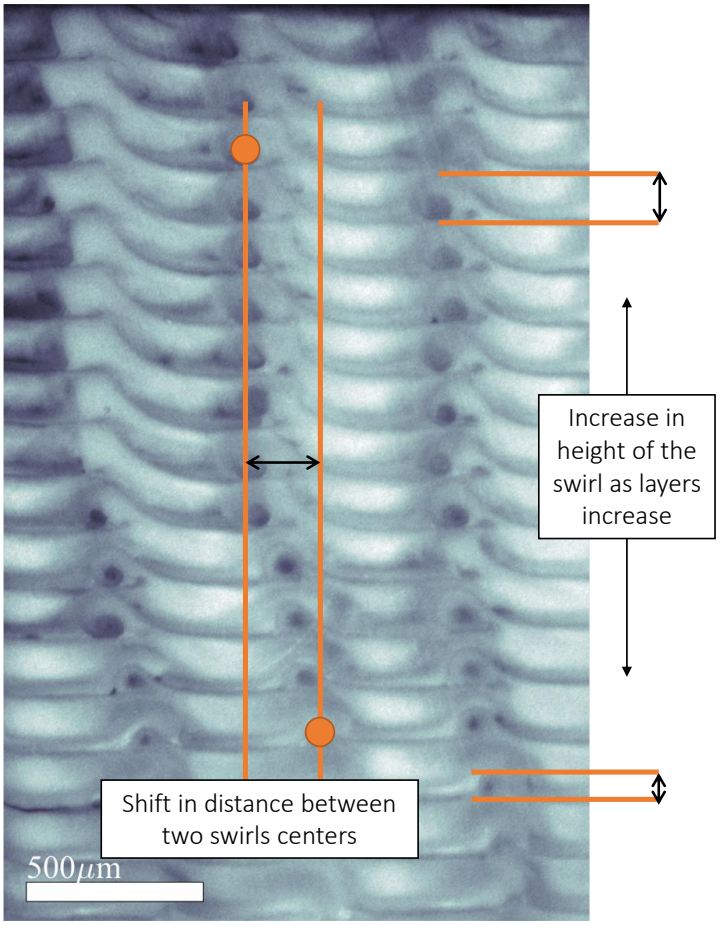

Figure 5.3 – *Close-up of F102 0.5 0 6 in which colors are changed for visibility. The shift in distance between swirl centers is illustrated by the horizontal orange lines, while the increase in height of a swirl is highlighted by the vertical lines.*

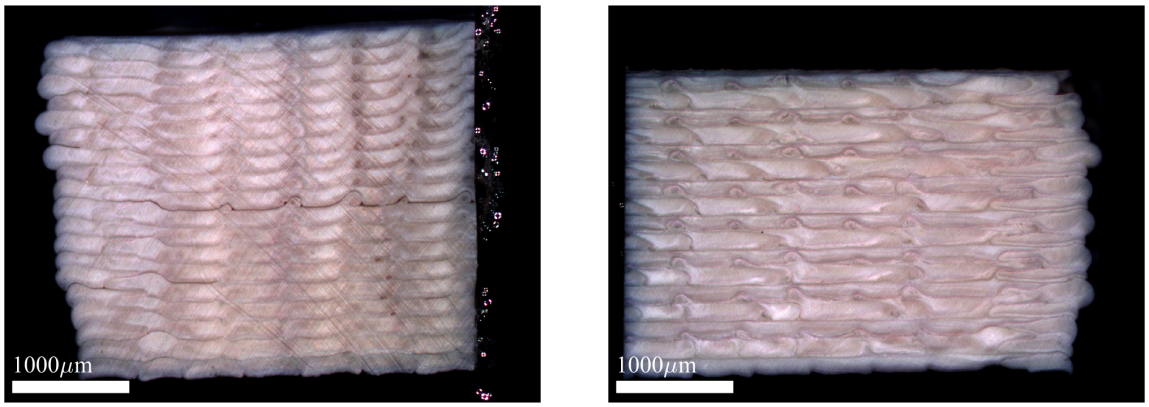

(a) F102 0.5 0 3 **(b)** F102 0.5 090 5

Figure 5.4 – *Micrographs of transverse cross-section of samples displaying regular and tall swirl features. Print parameters are identical except for the infill direction, set at 0° on the left-hand side and [0/90] on the right-hand side.*

5.2. Formation of interlayer features: image analysis

The aim of the image analysis procedure in this section is to verify Hypothesis *H1.3: The exit path for the molten material is situated at one of extremities of the nozzle, which creates a notch in the otherwise flat layer*, illustrated in Figure 5.6. Verifying this hypothesis can be done in two phases: in Phase I, the distance between interlayer features can be compared to the distance between two nozzle passes set in the g-code, corresponding to one linewidth, as illustrated in Figure 5.6. In Phase II, the bead pattern on the image is compared to the theoretical bead pattern indicated by the position of the swirl, as illustrated in Figure 5.7. Methods are described in more details in Section 4.6.

This image analysis is carried on a subselection of 13 of the short beam test samples, which possess two attractive characteristics for the purposes of this phase: a noticeable interlayer pattern thanks to delaminations, simultaneously with noticeable bead boundaries, thanks to either voids due to under-extrusion, or delaminations. These samples are listed in Figure 5.5. Indeed, in order to verify Hypothesis *H1.3b* in a convincing manner, the boundaries between beads should be spotted without a doubt. However, spotting them is not always straightforward: as highlighted in Chapter B of the Appendix in more details, color differences (skin/core patterns) are not reliable to distinguish between bead boundaries under polarized light. The presence of voids or delaminations in some samples, caused by the mechanical tests or by the under-extrusion, is in fact a convenient tool that avoids this difficulty. Indeed, voids or delaminations isolate beads one from another, which results in them being visually highlighted.

Phase 1 – Graphs showing distances between interlayer features are gathered in Figure 5.5 according to the line width set for each sample. In all these cases, one can see that in spite of the scatter which can partially be imputed to the human factor, the average distance between interlayer features matches very well the line width set for the sample.

Phase 2 – Figure 5.7 contains 4 of samples from the sub-selection in which the bead boundary is clearly visible due to under-extrusion or delaminations. The 9 other pictures are available in the Supplementary Data [14]. In these images, the locations of beads are symbolized by a colored transparent rectangle and derived from (4.4), itself directly derived from Hypothesis *H1.3b* and recalled in Figure 5.6. The reader is invited to assess how the perimeter of these rectangles matches with the beads on the bottom layers of the specimens, whose boundaries are noticeable thanks to voids and delaminations. It can be concluded that on the samples studied, the bead locations overlaps well with the one derived from the location of the interlayer features.

5.3. Formation of interlayer features: macroscopic observations

A video (external link available in [53]) records an early sample during print. A USB microscope is used to film the print inside the printing enclosure. The microscope is installed before the print starts, and before the pre-heating phase, in order to not disturb the thermal environment during print. In this video, the interlayer features can be seen as parallel trails, left on the side of the nozzle which overlaps on material deposited in the previous pass. These trails are indicated in a snapshot from this video in Figure 5.8b. Figure 5.8a shows a picture with the same USB microscope, of a layer detached from an earlier print, in which swirls can be seen. The nozzle path is also noticeable.

This macroscopic evidence shows that interlayer features appear during the printing process, when the nozzle passes on top of deposited material. The video [53] indicates that the nozzle creates two interlayer features as it deposits a line, but that one of them is ironed over in the next pass.

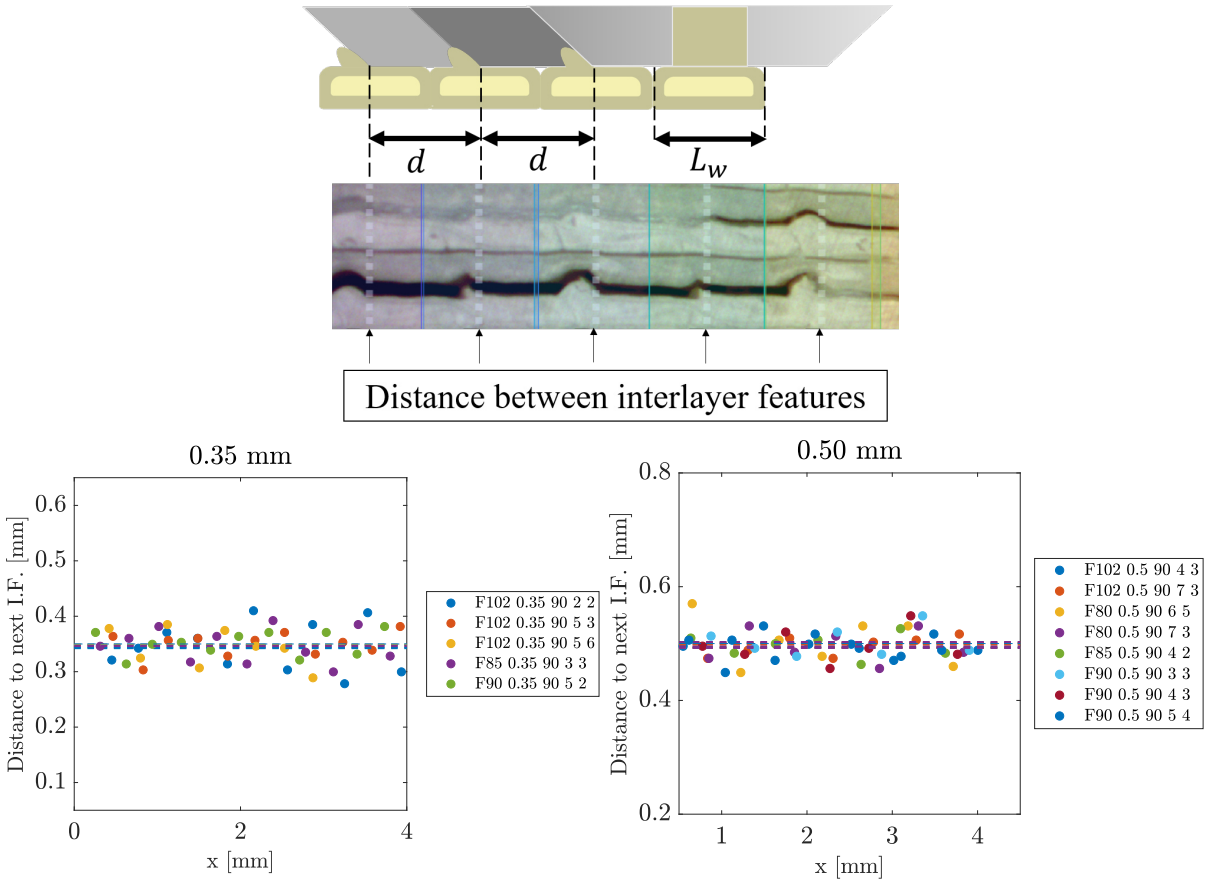

Figure 5.5 – *Scatter plot of the distance between swirls for a sub-selection of short-beam tests samples (Phase 1). The x-coordinate of each point represent the location of an interlayer feature on the image, and its y-coordinate represents the distance between this swirl and its right neighbour on the micrograph.*

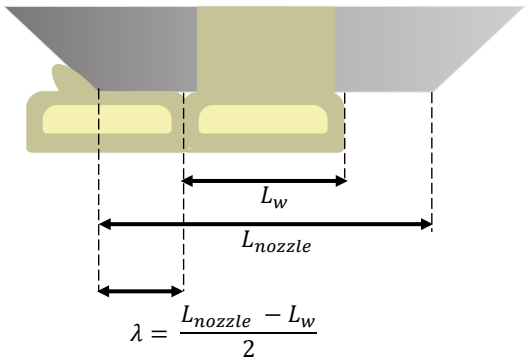

Figure 5.6 – *Representation of Equation* (4.4)*. According to Hypothesis H1.3, the swirls are created by the nozzle extremity due to over-extrusion. To verify this hypothesis, one can plot the nozzle location indicated by the corner of the swirl, and see whether the bead that would have been created by this nozzle pass is effectively noticeable on the image. The theoretical distance λ between a swirl and the bead creating it, depends on the line width L_w set in the g-code, and the nozzle tip diameter L_{nozzle}, two known parameters.*

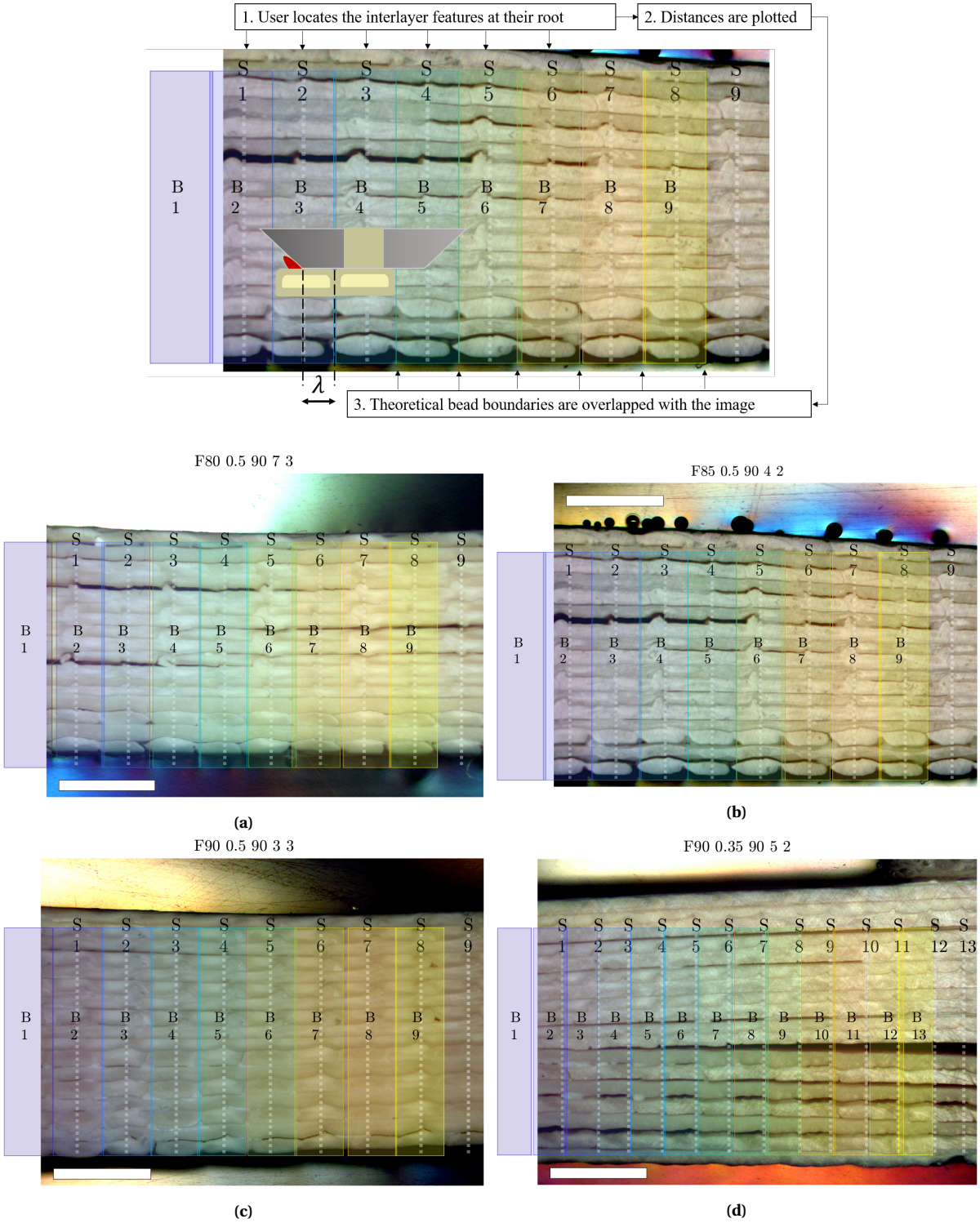

Figure 5.7 – *Micrographs of a sub-selection of short-beam tests samples (Phase 2). Scalebar is 1 mm. Location of swirls is indicated by white dotted lines. The corresponding nozzle pass is shown in a transparent rectangle with matching number. The reader is invited to compare the beads on the bottom layers, for which boundaries are easily visible, to the overlapped rectangle, indicating their location derived from the swirl position according to Eq. 4.4.*

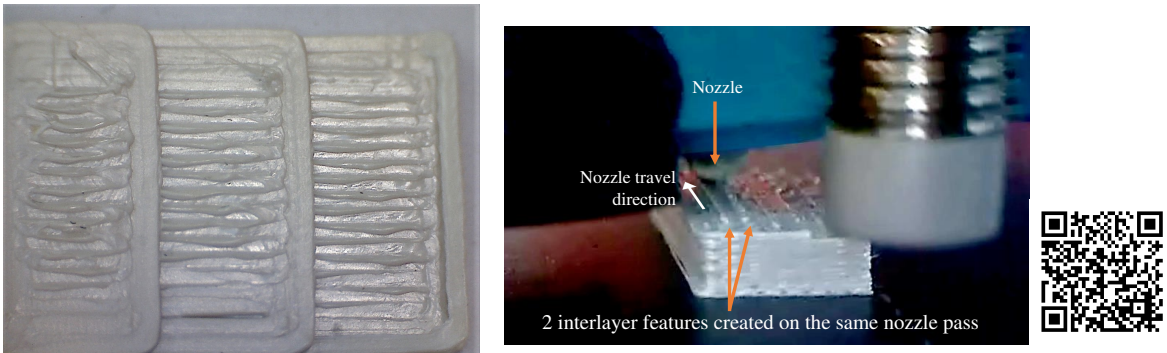

(a) (b)

Figure 5.8 – *Macroscopic observations: images and video of early samples.(a) Layer displaying swirls detached from a print, observed with a USB optical microscope. (b) Snapshot of the video available in [53] and through the QR-code, captured with a USB optical microscope. On this video, the interlayer features can be seen as parallel trails left by the nozzle. In this snapshot, the nozzle has left two interlayer features, one on each of its sides.*

5.4. Reinforcing potential of interlayer features: Mechanical tests

The second research question addressed in this thesis focuses on the performance of samples in interlaminar shear, with and without interlayer features. As a result, mechanical tests are useful combined with observations on the cross-sections of samples. In this section, raw data will first be described, followed by considerations on the mass of the specimens, and finally short-beam shear strengths will be reported for unidirectional and [0/90] samples.

5.4.1. Raw data

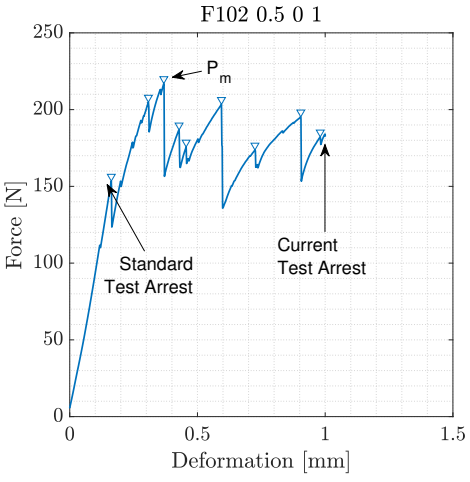

(a)

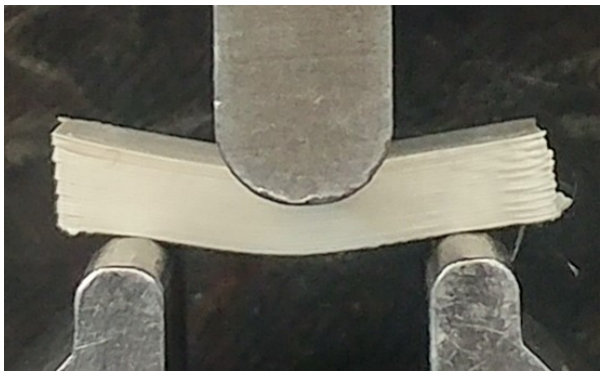

(b)

Figure 5.9 – *(a) Example of raw data: Sample F102 0.5 0 1 (b) Sample in the test fixture at maximum cross-head deformation. On the left-hand side, delaminated zones can be observed.*

Short-beam tests are conducted according to ASTM test D2344 [52], and the procedure is reported in details in the Methods Section 4.4. Short-beam strength is calculated from (4.3). As illustrated in Figure 5.9a, P_m is the maximum load experienced during the test, which, according to the standard, should be stopped when one of the following criteria is met: a load drop-off of 30%, two-piece specimen failure, or cross-head travel exceeding the specimen thickness (in this case, approximately 3 mm). Instead of these, the following criteria is

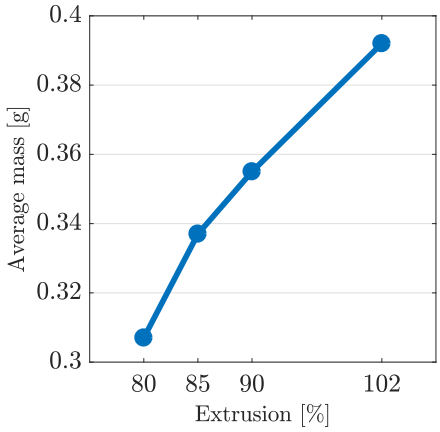

Figure 5.10 – *Average mass of one series (line-width and infill orientations combined) against extrusion rate*

Extrusion (%)	Mean Mass (g)	Var. Mass to Ref. (%)	Var. Extr. to Ref. (%)
80	0,307	-11,7	-10,4
85	0,337	-3,1	-4,8
90	0,355	2,1	0,8
102	0,392	12,7	14,3
89,3	*0,348*	*0,0*	*0,0*

Table 5.1 – *Average mass for each series (linewidths and infill orientations combined), compared to a reference point chosen as the average of this column and shown in the bottom row. The variation to a mean extrusion rate is also shown.*

applied for the purposes of this test, in order to secure the possibility to observe at least one delaminating zone in the cross-section for each sample: test stops when cross-head travel exceeds 1 mm, or 60% load drop-off. The impact of this choice is discussed in the Appendix, Section C.2.1. Cross-head speed was set according to the standard, at 1mm/min.

The load case in a short beam test is often considered complex because it can lead to mixed-mode failure instead of shear failure if the ratio of flexural strength over interlaminar shear is too low [54]. In the case of this experiment, all specimens delaminated in shear.

The raw data curves can be found in the Appendix in Figures C.9 to C.12. An example is provided in Figure 5.9a. In the majority of samples except the over-extruded ones, some cracks become visible from the sides after cross-head is released. On Figure 5.9b, one can notice the beam being split into several smaller beams on the left side of the specimen. A delamination effectively splits a beam into two, and reduces its stiffness by the amount prescribed by beam theory. This may also explain the saw-tooth shape noticeable in the raw data curves. Since the test is displacement-controlled, each drop in force corresponds to a delamination either opening further, or being created in another zone.

5.4.2. Mass of the specimens

In this test, the extrusion percentage is the parameter studied that is tied to the formation of swirls. However, as mentioned earlier, varying this percentage also changes the amount of material present in a sample. As a result, concern may arise on the validity of possible conclusions: if interlaminar shear strength increases with the extrusion percentage, this increase may either be imputed to the change in mesostructure with the growing presence of interlaminar features as expected, or to the increased material mass. In order to undermine this undesirable side-effect, the mass of each sample is measured, so that interlaminar shear strength can be normalized by the mass of each sample.

The mean mass, thickness and width of each sample are gathered in Table C.1 in the Appendix, along with standard deviations and coefficient of variations. While the thickness and width are taken into account in the short beam strength by Equation (4.3), the mass does not appear, even though it logically varies between samples, given the variation of the extrusion parameter. Table 5.1 gathers the average mass for each extrusion series - i.e, with linewidth and infill orientations combined. This mass is then compared to the mean mass of all samples, as a reference. A plot in Figure 5.10, shows a linear relationship between the average mass and extrusion rate. Therefore, an alternative plot to the SBS is shown in Figure 5.16 and 5.19, where all strength values are scaled by the mass of every sample.

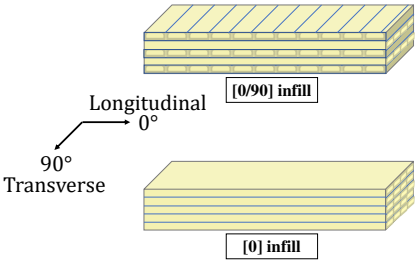

Figure 5.11 – *Two infill types are mechanically tested. Although they cause the samples to have different stiffnesses and thus their interlaminar shear strengths cannot be directly compared, they give indications whether the orientation of interlayer features plays a role in their ability to act as reinforcing features.*

5.4.3. Short-beam shear strengths

Two different infill types are tested, as illustrated in Figure 5.11: unidirectional, and [0/90]. This allows to test for two directions of the interlayers features with respect to the shear direction: parallel and perpendicular. In this section, results are reported and grouped according to extrusion rates. Interpretations of these results are available in Chapter 7.2. Short-beam strengths of samples are given first for unidirectional samples in Figure 5.14, and then for [0/90] samples in Figure 5.17. Along with the scatter plot representing the short beam strength of each sample, a general trend of microscopy observations is recalled, for two purposes: first, to compare the level of scatter within one configuration to potentially different mesostructures between these samples, thus bringing to light possible reasons for this scatter. Second, these microscopy observations mention the type of interlayer features displayed as a trend within one configuration and whether they are numerous or not, thus allowing to compare sample configurations together both by mechanical performance, and by presence or absence of interlayer features.
The short beam strengths, as well as the standard deviations, are represented in Table 5.12 and Figures 5.15 and 5.18. Taking into account the fact that over-extrusion may add more material to the samples, these results are also presented normalized by the mass of each sample in Table 5.13 and Figures 5.16 and 5.19.

Extrusion	F80		F85		F90		F102	
(MPa)	Mean	St. Dev.	Mean	St. Dev.	Mean	St. Dev.	Mean	St. Dev.
[0] 0.35	5,72	0,50	5,85	1,37	6,48	0,80	7,95	0,91
[0] 0.5	4,92	1,06	6,83	1,33	6,38	1,98	7,96	0,90
[0/90] 0.35	2,73	0,58	2,19	0,49	3,35	0,39	5,86	0,95
[0/90] 0.5	2,92	0,66	3,14	1,04	3,77	1,34	6,36	0,56

Figure 5.12 – *Mean short beam shear strength of the different sample configurations. This data is also illustrated in Figure 5.15 and 5.18*

Extrusion rate	F80		F85		F90		F102	
(MPa/g)	Mean	St. Dev.	Mean	St. Dev.	Mean	St. Dev.	Mean	St. Dev.
[0] 0.35	17,93	1,42	16,89	3,75	17,50	2,33	19,33	2,27
[0] 0.5	15,60	3,44	18,69	2,82	17,64	5,01	19,55	1,74
[0/90] 0.35	9,23	2,22	6,50	1,58	9,46	0,87	15,41	2,27
[0/90] 0.5	9,94	2,21	10,52	3,47	11,21	3,51	17,29	1,61

Figure 5.13 – *Mean short beam shear strength, normalized by mass, of the different sample configurations. This data is also illustrated in Figure 5.16 and 5.19*

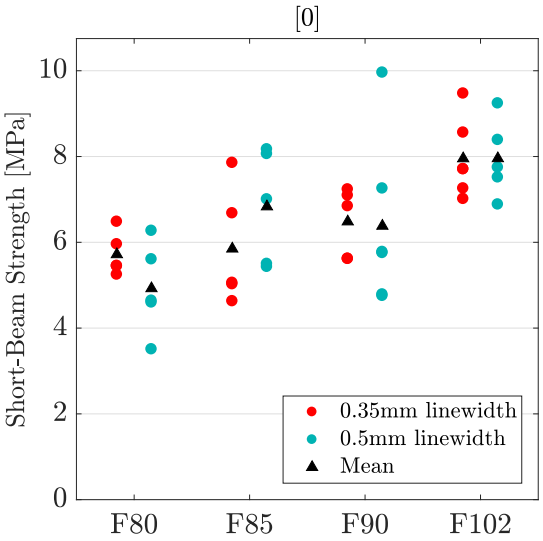

General trend of microscopy results:

F80-F85 – Small, barely noticeable notches present on all samples. In some cases, from a certain height, swirls may be visible as shown in Figure 5.1a

F90 – Fully formed swirls are present in varying amounts in most samples. An example can be found in 5.1c.

F102 – Fully formed swirls are present in all samples. See 5.1d.

Figure 5.14 – *Short beam strength of unidirectional samples.*

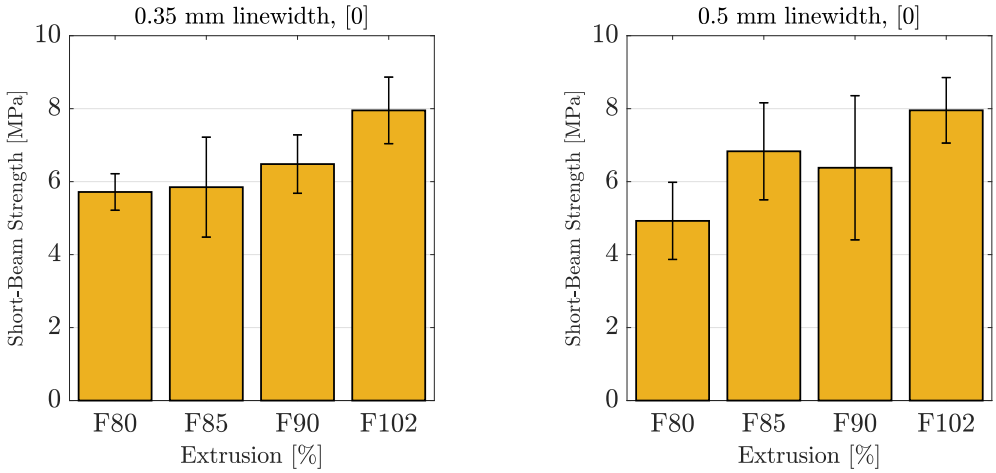

Figure 5.15 – *Short beam strength of unidirectional samples. The length of an error bar represents two standard deviations.*

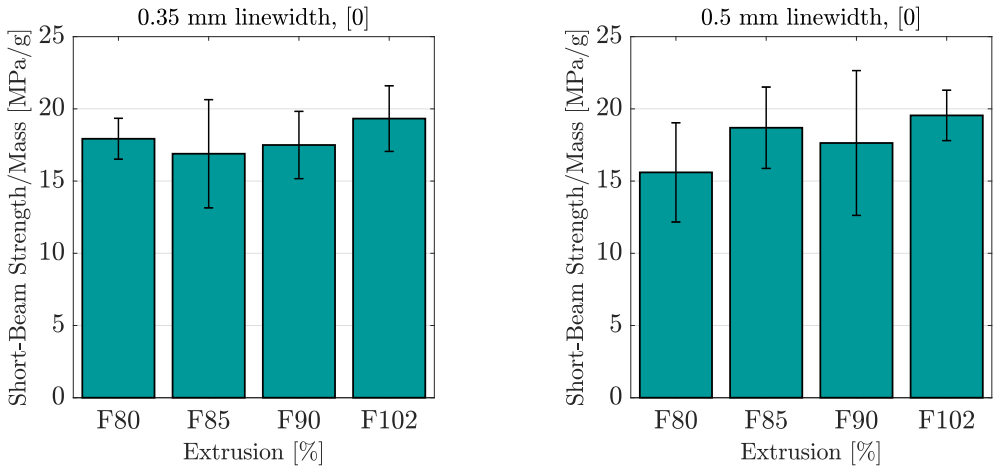

Figure 5.16 – *Short beam strength of unidirectional samples, scaled by mass of each specimen. The length of an error bar represents two standard deviations.*

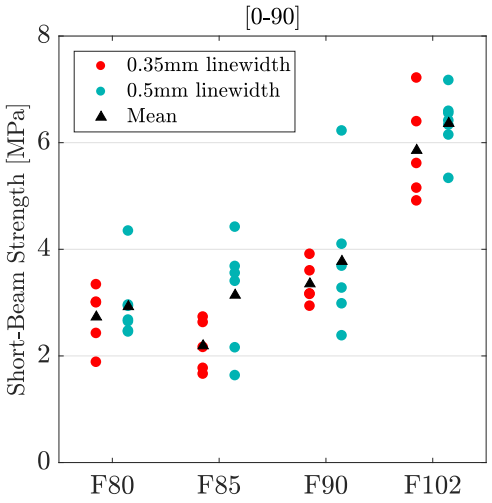

Figure 5.17 – *Short beam strength of [0/90] samples.*

General trend of microscopy results:

F80 – Small, barely noticeable notches are present in restricted areas.

F85 – Few notches can be found in the 0.35-mm linewidth series, but they are present in the 0.5mm linewidth series in restricted areas.

F90 – Two 0.35mm samples display very small notches in restricted area, two others do not display any interlayer feature. All 0.5mm samples display tall notches, except one which only shows an uneven layer profile.

F102 – Tall interlayer features can be seen, although their shape varies more in the 0.35mm linewidth series.

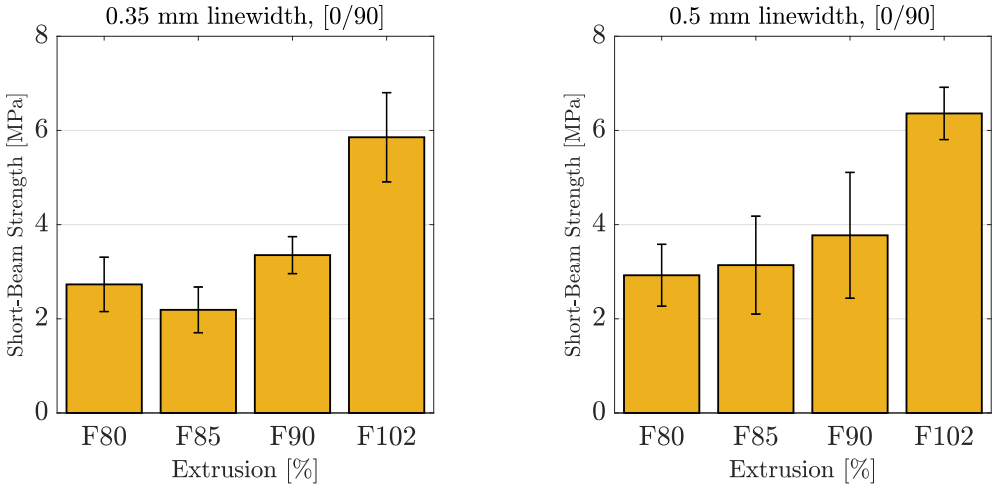

Figure 5.18 – *Short beam strength of [0/90] samples. The length of an error bar represents two standard deviations.*

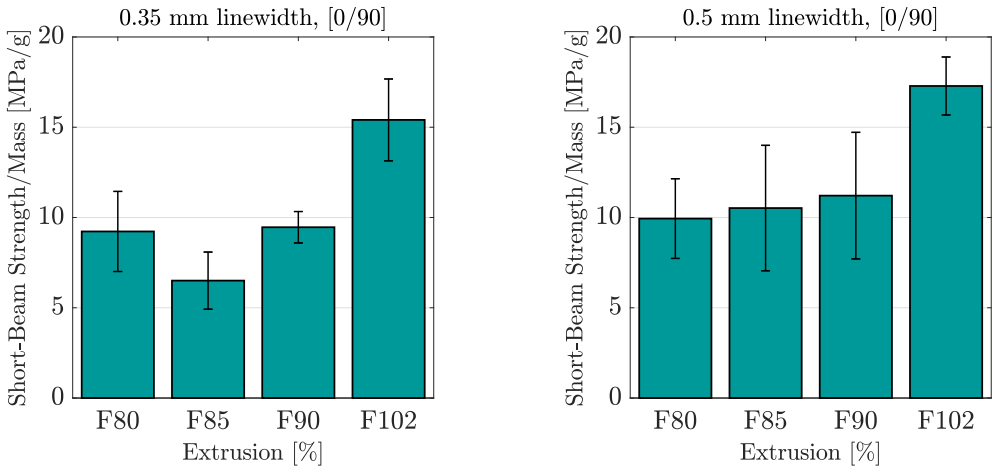

Figure 5.19 – *Short beam strength of [0/90] samples, scaled by mass of each specimen. The length of an error bar represents two standard deviations.*

5.5. SUMMARY

5.5.1. Formation of interlayer features: a summary of observations

Several elements put forwards in the macroscopic and microscopic observations in the previous section have to be taken into account in a formation mechanism:

a) Interlayer features are created during the printing process

b) Interlayer features form in contact with the nozzle tip

c) In some cases, two interlayer features form during one pass, one at each extremity of the nozzle

- Considering the fact that the nozzle tip is 1 mm wide, and that the linewidth is set from 0.35 to 0.5 mm, the fact that the interlayer features can form on two sides suggest an offset in the bead placement.
- If two interlayer features form during one nozzle pass, the outermost one has to be melted during the next nozzle pass, which is equivalent to the nozzle extruding additional material in this next pass.

d) Presence of interlayer feature is encouraged by over-extrusion, but no over-extrusion, and even under-extrusion, can still result in interlayer features.

e) Interlayer features are propagating within one material: once they have appeared, they tend to maintain themselves. However, they only tend to grow with over-extrusion in a 0° specimen.

Some of these observations, such as a) or b), directly answer hypotheses formulated in Chapter 3. But most importantly, from these observations arise questions, which are presented in Chapter 6.2. These observations have to be reproduced accurately by a formation mechanism for the interlayer features, but most importantly, this formation mechanism should also attempt to provide explanations for these observations, and for the resulting questions. This is the aim of Chapter 6.2.

5.5.2. Reinforcing potential of interlayer features: a summary of observations

The short beam shear of unidirectional samples does not seem to increase with extrusion rate, while it does increase significantly with [0/90] samples: from under-extruded to over-extruded samples, the percentage increase in short-beam strength normalized by mass is 64% for the 0.5mm-linewidth samples and 83% for the 0.35mm-linewidth samples. The scatter, in both infill configurations, is relatively high, and partially imputable to the presence or absence of interlayer features in the cross-section of samples. Since mechanical interlocking is hypothesized to be the main reason of this increase, one can also attempt to go beyond the mere observation of the presence or absence of interlayer features, and focus also on their geometry, to understand how the mechanical performance is affected by it. This will be discussed in details in Chapter 7.

6

Discussion: Mechanism of Formation of the Interlayer Features

INTRODUCTION

By observing the cross-section of 3D-printed Vectra samples, regular interlayer features, often displaying a distinctive spiraling pattern, can be noticed. The following question naturally arises: *Why, and how, are interlayer features formed during the print*?. Several hypotheses have been made to answer this question, and are recalled below.

Hypotheses on formation of interlayer features

H1.1 The interlayer features form because the material is over-extruded by the nozzle.

H1.2 Material belonging to a just-deposited line gets molten again as the nozzle passes over it to deposit the neighbouring line. As the new bead is being deposited, it expands against the molten material, pushing it outwards.

H1.3 The exit path for the molten material is situated at one of extremities of the nozzle, which creates a notch in the otherwise flat layer.

a) The distance between the interlayer features corresponds to the distance between two lines created by the nozzle (line width)

b) From the observed distribution of interlayer features on a printed specimen, the corresponding placement of the nozzle creating the neighbouring bead matches with the observed distribution of beads in the cross-section.

Hypothesis H1.1, focuses on the original reason why they may be created, while H1.2 and H1.3 focus on how they are created. However, while Hypotheses H1.1 and H1.3 refer to phenomena which can be observed after the print via observation of its cross-section, Hypothesis H1.2 refers to a process happening during the material deposition, which can not be verified experimentally with the present set-up directly. This hypothesis however, is in short a proposition of a formation mechanism. Thus, a way of verifying this hypothesis in spite of this difficulty is to develop further this mechanism and its implications, and to use microscopy observation of samples to correlate the implications whenever possible.

This chapter is divided into three main parts. In a first part, the observation campaign reported in Chapter 5 is interpreted, and summarized into a series of observations and questions feeding into the next part, in which a mechanism of formation of the interlayer features is established. Then, a complementary mechanism is proposed for the formation of a swirl in particular, with a spiraling pattern.

6.1. INTERPRETATION OF THE OBSERVATIONS

While the general trend of microscopy observations, available in the online appendix, shows that the number of interlayer features does seem to increase with increasing extrusion rates, Section 5.1.2 puts forward that over-extrusion is not a necessary condition for interlayer features, invalidating Hypothesis H1.1. Indeed, interlayer features can be observed in samples with a very low extrusion rate (80%). In these cases (Figures 5.1a and 5.1b), two zones exist: on lower layers, severe under-extrusion as expected; and on upper layers, presence of interlayer features, accompanied by an apparent offset of bead boundaries with respect to the first zone, whereas the g-code does not change between these layers. In contrast to the under-extruded cases, the interlayer features are present from the beginning of the print in the F102 samples. They also increase in size with taller layers, but only in the unidirectional infill. In the [0/90] infill, they do not seem to grow, suggesting that the deposition surface plays a role in their formation. This will be further discussed in Section 6.2.1.

Results both from microscopic and macroscopic observations, seem to provide evidence corroborating Hypothesis H1.3: the interlayer features are formed at the nozzle extremity as it passes to deposit a neighbouring bead. Macroscopic evidence, on its own, indicates that interlayer features are created during the printing process. It also suggests that the nozzle may leave an interlayer features on both of its extremities, but that one of them is ironed over at the next pass of the nozzle. This latter point is also in line with the fact that interlayer features are regularly located at a distance of a linewidth from each other, which also corresponds to the offset in the path followed by the nozzle depositing two lines, corroborating Hypothesis H1.3a. Furthermore, the fact that it is the tip of the nozzle that shapes the interlayer feature is further confirmed by the image analysis in Figure 5.7, in which the position of beads matches well with the expected one according to Hypothesis H1.3b.

In short, the following elements put forward in the macroscopic and microscopic observations, recalled from the summary of Chapter 5, have to be taken into account in this formation mechanism:

a) Interlayer features are created during the printing process

b) Interlayer features form in contact with the nozzle tip

c) In some cases, two interlayer features form during one pass, one at each extremity of the nozzle

   - Considering the fact that the nozzle tip is larger than the linewidth by 100% or more, the fact that the interlayer features can form on two sides suggest an offset in the bead placement.
   - If two interlayer features form during one nozzle pass, the outermost one should melt during the next nozzle pass, which is equivalent to the nozzle extruding additional material in this next pass.

d) Presence of interlayer feature is encouraged by over-extrusion, but no over-extrusion, and even under-extrusion, can still result in interlayer features.

e) Interlayer features are propagating within one material: once they have appeared, they tend to maintain themselves. However, they only tend to grow with over-extrusion in a 0° specimen.

Beyond these elements, contradictions and questions emerge. In order to be both convincing and useful, the proposed formation mechanism should not only be in accordance with these observations, but also explain apparent contradictions embodied in the following questions:

a-b) Where does the material forming swirls come from?

c) Why can swirls be formed both at the tip of the nozzle already in contact with material, and on its other free edge, if the bead width is smaller than the nozzle flat?

d) Why do unidirectional samples form swirls even when they are subjected to severe under-extrusion?

e) Why do swirls increase in size as the print builds up in unidirectional samples whereas they do not in their [0/90] equivalents?

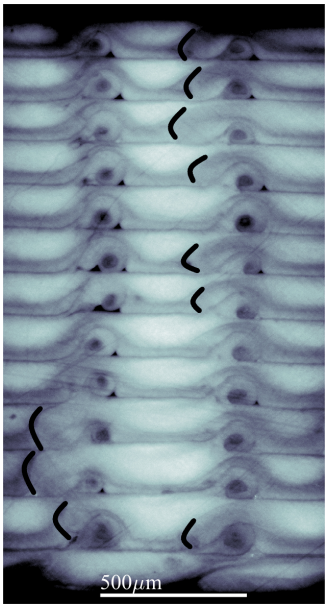

(a) Close-up of an early sample, print direction from right to left

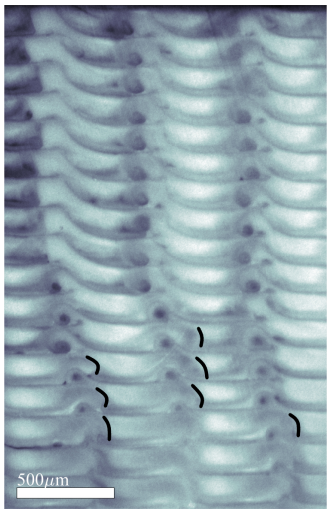

(b) close up of F102 0.5 0, print direction from left to right

Figure 6.1 – *Close-up on micrographs of samples displaying regular and tall swirl features. Boundaries are outlined in black. Contrast has been enhanced with false colors.*

6.2. Proposition of a mechanism of formation of an interlayer feature

This proposal will be divided into two parts, the first one in Section 6.2.1, presenting a mechanism in which an offset building up in the bead formation triggers the formation of interlayer features, and the second one, focused on the swirls themselves and the spiraling phenomenon.

6.2.1. Swirl formation triggered by the propagation of an offset in misplaced beads

The sharp transition between two zones for under-extruded samples recalled in the previous paragraph and reported in Section 5.1.2 indicates that the formation of swirls is closely associated with an offset in bead deposition localization. Figure 6.1 also indicates that bead boundaries are affected by the presence of swirls, as any deposited bead has to overlap the swirl created during deposition of the previous layer. The impact of the presence of swirls on bead boundaries is discussed in the upcoming paragraph. Insights on the formation of swirls are gathered by simply simulating the effect of the presence of swirls on a deposition surface. This will bring forward that interlayer features can be seen as a way to alleviate the pressure that builds up in the material as misplacement of the bead increases.

An investigation is carried on the disruptive effect of the presence of interlayer features on the propagation of beads. Indeed, the presence of interlayer features on one layer affects the next layer as the volume of material calculated and extruded, effectively does not correspond to the true volume available: interlayer features already make use of a non-negligible portion of this volume. Even without over-extrusion, the simple fact of having interlayer features may trigger a similar effect to over-extrusion, with gradual translation of each bead further outwards. This is a possible element of explanation for Question e) raised in the previous paragraph.

The impact of the presence of swirls in the deposition surface on the upcoming beads, is illustrated in Figure 6.2. The case represented is that of the nozzle printing lines with a 0.5mm linewidth. The swirls are considered, for the sake of the example, to represent roughly 16%, or 1:6 of the total cross-sectional area of

material extruded. The nozzle is located above the corner of a swirl. The boundaries of beads, should no disturbance exist, are depicted with colored lines of the corresponding color of each bead. They should of course be deposited underneath the center location of the nozzle. The colored areas depict the effective location of material destined for a specific bead. These colored zones are therefore of equal areas but different layouts, as the material can only take the space that is effectively available at this point in time. The logic behind Figure 6.2, which should be read as a printing sequence, is detailed here:

1. The first bead, B1, is already affected by the presence of a swirl. It is assumed to start in its theoretical location, but the presence of a swirl over 1:6 of the area shifts the rightmost extremity of this boundary by the same amount.
2. The next bead, B2, already finds its theoretical area occupied in 1:3. Indeed, 1:6 is taken by the shift of Bead B1, and 1:6 is also taken by the presence of another swirl on the bottom surface. Therefore, this second bead already shifts its rightmost extremity by half the expected linewidth. It finds itself in between two swirls.
3. The next bead deposited, B3, finds half of its intended volume already occupied: one third is occupied by bead B2 and one sixth by a swirl. As a result, its boundary oversteps onto the next swirl.
4. For the same reason, Bead B4 can only therefore have 1:3 of its theoretical volume available.
5. The situation worsens as for any subsequent bead, the offset is increased by 1:6.
6. As can be expected, the sixth bead deposited cannot flow out of the nozzle, as its opening is completely covered by the previous bead.

It could be expected that in the situation of bead B6, the nozzle would become clogged: pressure build-up tends to produce a back-flow in the extruder: typically, this causes the melting zone to extend farther than the hot-end, solidify, and block extrusion. However, no clogging is noticed during the prints with Vectra, suggesting that this printing sequence does not represent reality.

In fact, before such a blockage happens, it can be noticed that the available path for the material to flow out of the nozzle 6.2 becomes narrower and narrower as the offset increases. This may lead to a pressure build-up within the nozzle. One should then remember that Vectra has shear-thinning properties, meaning low viscosity when exposed to shear. Furthermore, its enthalpy of fusion is 1 to 2 orders of magnitude lower than conventional 3D printed polymers, which may allow it to change from liquid to solid state with a low energy input. These key characteristics can enable the pressure build-up to be alleviated by the formation of interlayer features, instead of resulting in a nozzle jam. This indicates that interlayer features result in fact from a pressure-alleviating mechanism.

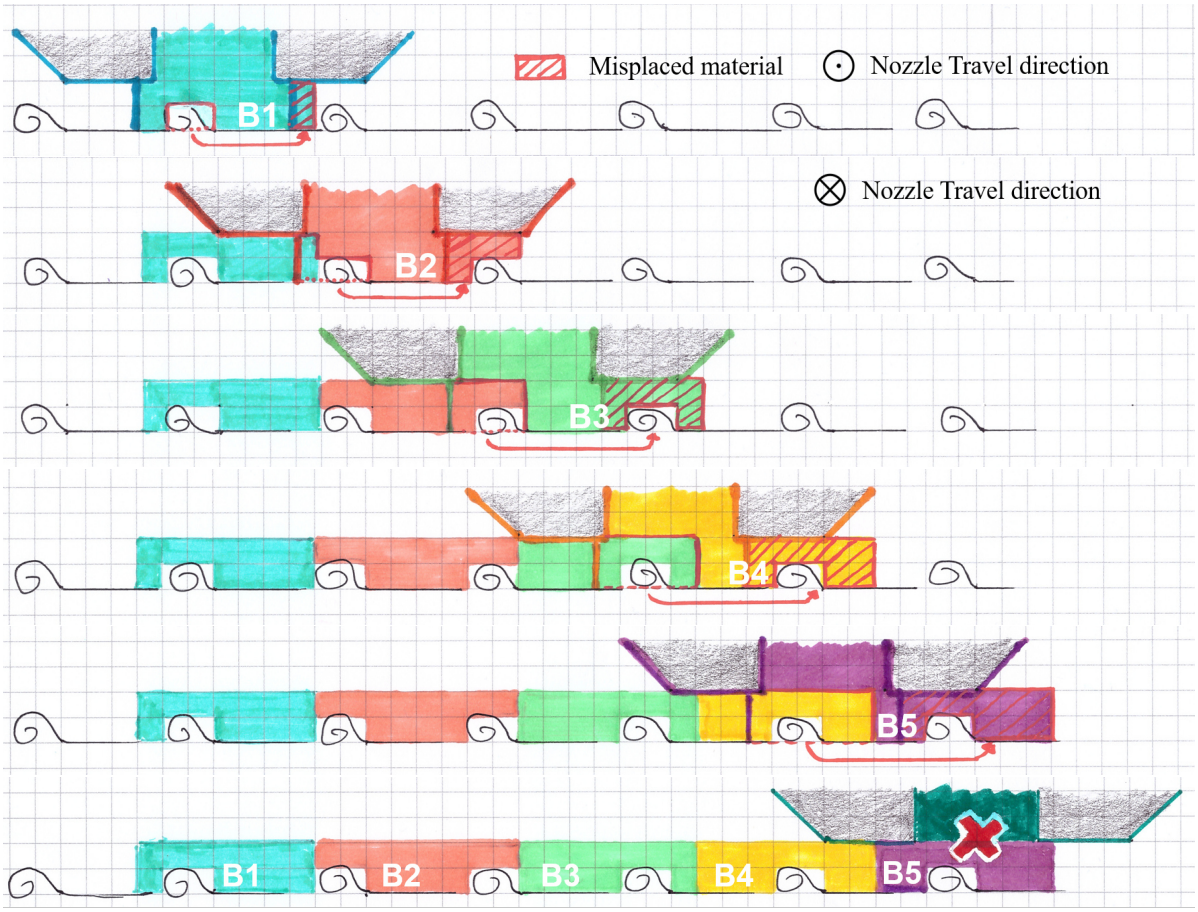

Figure 6.2 – *Transverse cross-section of the print, with the nozzle location and bead deposition history sequence. The distribution of beads takes into account the presence of interlayer features on the deposition surface. To be read from top to bottom. The names B1 to B6 identify bead shapes. Each square represents one twelfth of the cross-sectional area of a bead that should be deposited by the nozzle. The schematics is on scale, with 12 squares to 1 mm. The case represented here is of 0.5 mm linewidth.*

Swirls as alleviating mechanisms allowing the reproduction of one bead shape

One main argument in favour of considering swirls as alleviating mechanisms is that the bead patterns which can be seen for instance in Figure 5.1 do not change from the moment swirls have formed during the print, as if an equilibrium in extrusion had been attained. Furthermore, swirls have been observed to be self-replicating. As highlighted in Observation e), once they have appeared, they maintain themselves throughout a print. This leads one to wonder how material could be displaced in a way resulting both in the formation of a swirl, and in a bead shape arranged in a pattern maintaining itself from one pass to another – unlike the sequence of events leading to a blockage described in Figure 6.2. To answer Question a-b), three scenarios are proposed, each corresponding to the propagation of one bead shape: B1, B2 or B3, as shown in the same figure. The main difference between these three scenario is the formation of one or two swirls at each pass, which is the core of Question c).
The volume for upcoming molten material can be gained in three possible ways: either, on the right side of the nozzle, by overstepping the right swirl; on the left side by pushing the boundary, which may be molten to some extent or on the left side by creating a channel along the molten part of the previous bead. These two latter cases are illustrated in Figure 6.3b, top and Figure 6.3b, bottom, respectively. The former case would lead to a bead type B2 being created, which is covered in Figure 6.5.

Formation of one swirl: reproduction of the B1 bead pattern

Figure 6.3 represents the case of a B1 shape being reproduced by the formation of an interlayer feature. This scenario is envisioned in two steps. In the first step, the molten material takes the shape that is available. The

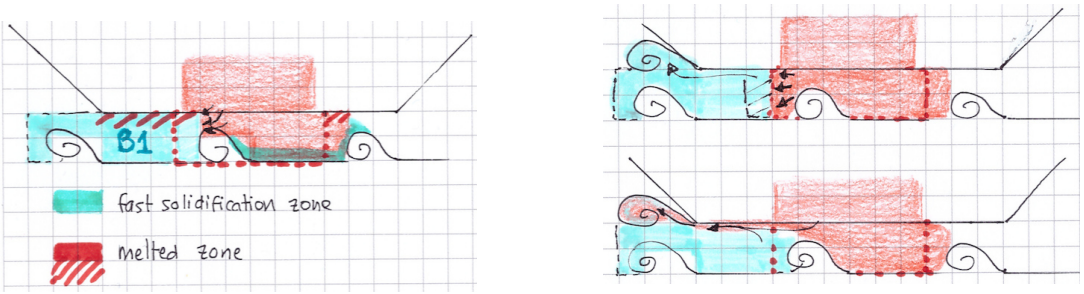

(a) First deposition stage, pressure build-up on initial boundaries

(b) Second deposition stage, pressure build-up and 2 possible pressure alleviating steps

Figure 6.3 – *Schematics of the pressure-alleviating mechanism in two steps, starting from a B1 bead shape. Colored zones represent material from different beads. Molten area of the neighbouring bead is represented with hatched red lines. Black arrow represent flow direction. Teal lines represent a zone which would solidify relatively faster than the others.*

part which is touching the bottom layer solidifies first, creating a skin zone, associated with dark colors in polarized light as seen on Figure 6.1b. This zone is depicted with an aqua-colored zone in the figure. Pressure builds up for more material to be extruded: 16% remaining on the figure, corresponding to the volume occupied by the swirl. Pressure-release happens in a second stage, shown in Figure 6.3b. The main difference between the top and bottom cases is the origin of the swirl material. It can be argued that the distance which should be travelled by material in the bottom case is far greater than that in the top case. However, this case still seems more likely as this path travelled is one of low resistance: the first bead is also molten in this area due to its proximity with the nozzle, in contrast to the top case. An evidence towards this possibility is also represented in Figure 6.4: on this close-up, boundaries can be distinguished with such a channel extending from a bead to the swirl.

These elements provide answers to Question a-b): *Where does the material forming swirls come from*?. It can also be envisioned that in reality a combination of the two possibilities shown in 6.3b may be at play: a channel of molten material is created underneath the nozzle irrespective whether this material had already solidified or not. This could mean that the swirl is in fact made of a blend of one bead and of its neighbour.

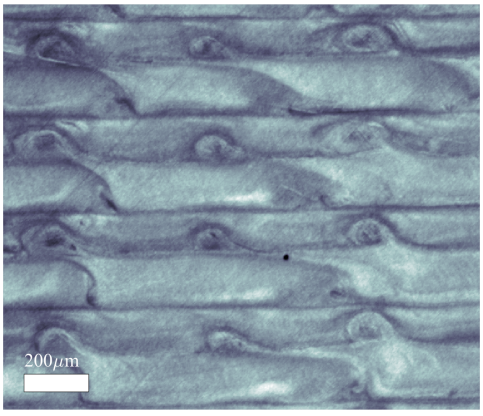

Figure 6.4 – *Close-up of Figure 5.4b, in which colors have been enhanced for visibility. A channel can be distinguished linking a bead to a swirl.*

Formation of one swirl: reproduction of the B2 bead pattern

Figure 6.5 represents the case of a B2 shape, with, once more, two steps depicted: before and after alleviation of the pressure by formation of a swirl. The resulting shape corresponds to that seen in the highlighted black regions in Figure 6.1b, as the bead seems to overlap the swirl.

Formation of two swirls: reproduction of the B3 bead pattern

Macroscopy observation via video recordings shown in Figure 5.8b has indicated that during print, the nozzle

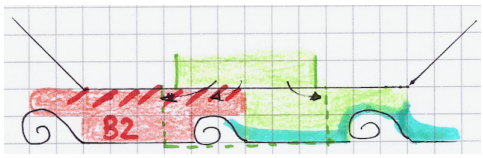

(a) First deposition stage, pressure build-up on initial boundaries

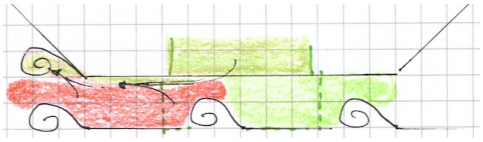

(b) Second deposition stage, pressure build-up and a possible pressure alleviating step

Figure 6.5 – *Schematics of the pressure-alleviating mechanism in two steps, starting from a B2 bead shape. Colored zones represent material from different beads. Molten area of the neighbouring bead is represented with hatched red lines. Black arrow represent flow direction. Aqua-colored line indicates a zone which would solidify relatively faster than the others as it is in contact with colder solidified material.*

may sometimes not form one but two interlayer features, on both sides parallel to its direction. This is the essence of Question c). A mechanism which allows two swirls to form at the same time is shown in Figure 6.6. For this to happen, material should be obstructing the nozzle in such a way that the next deposited bead exceeds the left-most nozzle tip. This is rather unusual: in normal printing conditions, this tip should never touch material.

In a similar manner as the two earlier scenarios, material leaving the nozzle has the possibility of expanding right or left. In Figures 6.6a and 6.6b, the material expands on the right side, as it is available. In 6.6b, it forms a notch with the right side of the hot nozzle. In the following pass of the nozzle, it irons over this notch, remelting it as a result with the extruded bead. This extra-material is left behind the nozzle as a swirl, in the way presented in the two scenario above. The right swirl continues being formed, ironed over and remelted for every new nozzle pass. In this manner, the B3 bead shape may be reproduced continuously.

Note on deposition surface

One observation which has only been partially addressed at this point is Question e), on the fact that swirls seem to grow in size in unidirectional samples while they do not in [0/90] samples. A difference between the two infills studied in this thesis, [0] and [0/90], is the profile of the deposition surface. Depositing material on a 0° or 90° layer should be equivalent without interlayer features. However, with interlayer features, this is not the case.

As highlighted earlier, swirls are in fact a self-replicating phenomenon even without over-extrusion: if the layer underneath the one printed displays interlayer features, it is likely that the next one will also do so, because the volume planned for the bead is partially occupied by the swirl from an underneath layer. This is the case in Figure 5.4a, where swirls may grow for this reason. In contrast, in the [0/90] case shown in Figure 5.4b, the presence of a 90° layer between each 0° layer allows the interlayer feature to be covered entirely, and the next layer to start on an even surface in which the theoretical volume corresponding to the extruded material is completely available. This further highlights the role of the depositing surface. In the [0/90] configuration, the scenario established in Section 6.2.1 can be adapted: indeed, since the self-propagating behaviour does not hold anymore, an external input of material is needed for the pressure build-up to occur: initial misplacement of beads because of an uneven surface, or local over-extrusion caused by the variations in filament diameter or other factors.

6.2.2. Summary

In this section, a discussion was carried on how the distribution of beads is affected by the presence of interlayer features on the deposition surface. Their presence alters the expected layout, and results in a gradual pressure increase as the available space is shifted from the bead deposition zone. Interlayer features are suggested to result from a pressure alleviating mechanism, enabled by the low enthalpy of fusion of Vectra: a fused bead can solidify with a low thermal energy input and inversely, a bead that has already solidified before can melt again in contact with the nozzle depositing its neighbour. The mechanisms presented above do not only reproduce, but also provide high-level explanations for all the observations gathered, such as the self-replicating ability of swirls.

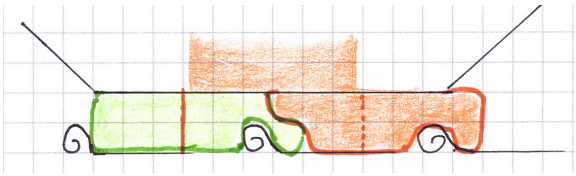

(a) Formation of bead type B3

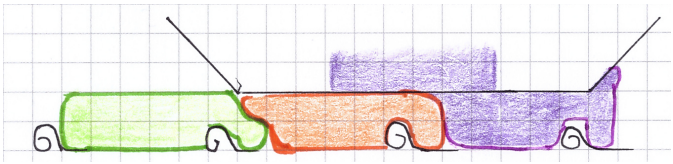

(b) The next B3 bead creates a front swirl

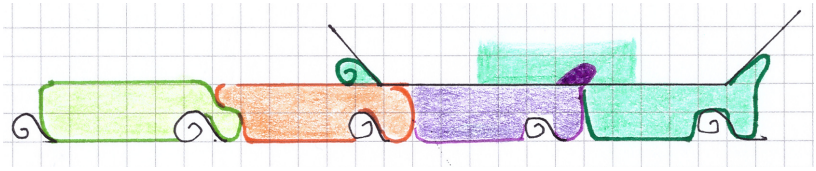

(c) This swirl is ironed over in the next pass, meaning extra material added to the molten bead: two swirls are created

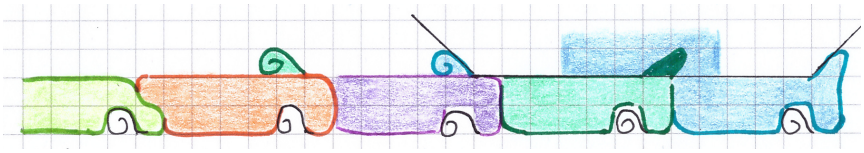

(d) One out of two swirls is left behind, the other one is ironed over.

Figure 6.6 – *Schematics of the pressure-alleviating mechanism in two steps, starting from a B3 bead shape, in which material fully exceeds the right-most nozzle tip, creating a path for swirls in the two sides of the nozzle. Colored zones represent material from different beads. A swirl now represents 1:12 of the volume of molten material deposited.*

6.3. PROPOSITION OF A MECHANISM FOR THE SPIRAL FORMATION

The formation of a spiral with several spires is a phenomenon often found in nature. However, to the author's knowledge, such a shape has never once been reported in the frame of additive manufacturing. In Section 6.3.1, two scenarios are proposed to explain this peculiar feature. These scenarios, established in two-dimensions, represent a phenomenon which is intrinsically three-dimensional. To take this into account, a discussion is carried in Section 6.3.2, extending these findings in three-dimensions via a possible helicoidal shape of the swirls.

(a) Close-up of F102 0.5 90 7

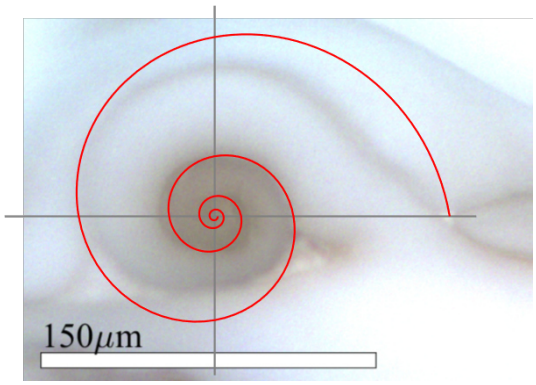

(b) A swirl overlapped with a logarithmic spiral

Figure 6.7 – *Cross-sections of samples seen under polarized light, zoomed on a fully-formed swirl with a distinctive spiralling pattern. Colors have been altered for better visibility.*

6.3.1. Description of two scenarios of formation

In this section, two possible scenarios for the formation of such a spiral shape will be discussed. These scenarios both rely on two important characteristics of Vectra highlighted in the literature study in Chapter 2: a shear-thinning behaviour with low viscosity, and a low enthalpy of fusion. The difference between them mainly lies in the onset of the coiling formation: either starting inside a solidified shell (scenario 1), or created by gravity as the material flows up the nozzle, followed by a collapse (scenario 2). Arguments in favour of each of them will finally be discussed.

Scenario 1: No Collapse

Scenario 1: Formation of swirl without collapse

In this configuration, swirls form starting from a notch, which solidifies, forming a shell. Spirals form within this solidified shell. The possible steps are illustrated in Figure 6.8.

(a) Pressure build-up results in material flowing out through a channel beneath the nozzle. Since it meets solid material, it tends to flow out of the nozzle, upwards around the nozzle tip.

(b) The proximity with the nozzle allows part of the molten bulge to remain in a liquid state, but it starts to solidify from the outside, forming a larger ellipsoid shape. Material continues to flow, and as a result, expansion also happens in parallel to the gradual solidification.

(c) The outer shell becomes thick enough to prevent further expansion of the shape, creating a backward flow movement of the molten material along the shell walls.

(d) This material in contact with the outer shell exchanges heat with it and solidifies in its turn as it flows, creating the start of the first spire in its backward flow movement.

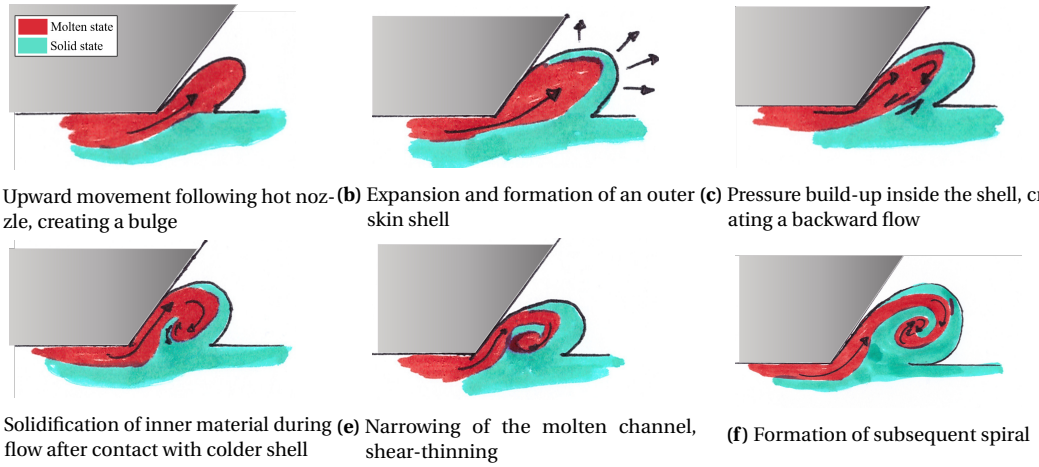

(a) Upward movement following hot nozzle, creating a bulge

(b) Expansion and formation of an outer skin shell

(c) Pressure build-up inside the shell, creating a backward flow

(d) Solidification of inner material during flow after contact with colder shell

(e) Narrowing of the molten channel, shear-thinning

(f) Formation of subsequent spiral

Figure 6.8 – *Suggested formation mechanism for swirls without collapse. In blue: solid state, in red: liquid state.*

(e) The channel continues solidifying and narrows down, causing the molten material to become less viscous due to its shear-thinning characteristics.

(f) The material continues flowing in this manner, forming thinner and thinner spires inwards, until pressure drops and solidification also happens in the core of the swirl.

As seen in Figure 6.7, a parallel can be drawn between the shape of a swirl, and a logarithmic spiral – a shape found for instance in nautilus shells [48]. A peculiarity of such a spiral is that its outermost shape is unaltered with each successive spire completed, which may be seen as an argument in favour of the initial formation of a shell according to the step seen in Figure 6.8b, within which material continues to flow. Moreover, in the step

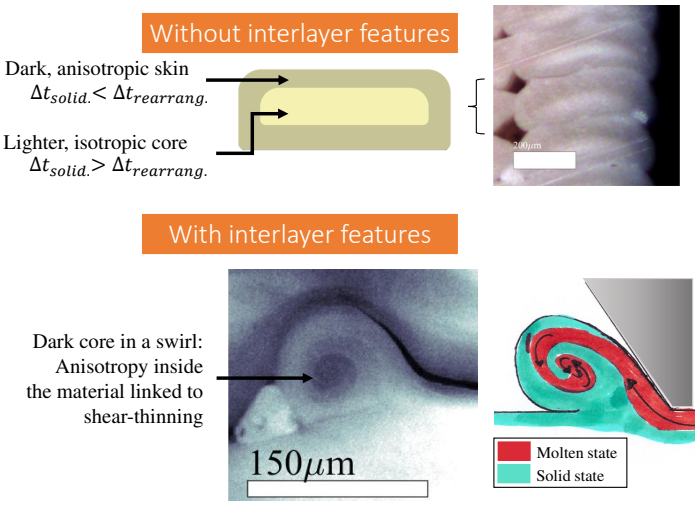

Figure 6.9 – *Schematics highlighting the anisotropy seen in the inside of a swirl, in contrast to the typical concentric skin/core pattern reported in [1] where anisotropy is located on the outer boundaries due to faster solidification.*

shown in Figure 6.8e, it is suggested that the spires can form thanks to the low viscosity of the material caused when it is sheared as the channel gets narrower and narrower, due to its shear-thinning characteristics. An observation correlating this is the fact that every swirl is darker in its center. In all features but this one, the darkest areas under polarized light are located in the outer boundaries. As highlighted by [1] or in Figure 6.9, darker zones are associated with higher anisotropy, and are thought to be caused by solidification occurring faster than the molecular reorientation of nematic domains. However, there is no reason for solidification to happen faster in the center of swirls than in their outer perimeter, therefore the apparent anisotropy linked to the darker zone must be caused by another factor. This shear-thinning step provides an explanation for the

formation of thinner and thinner spires inwards as shown in Figure 6.7, and for their color, linked to a higher anisotropy caused by shearing within the solidified walls as well.

Scenario 2: Collapse

A set of observation from the top layer of an early sample, found in Figure 6.10, brings further insight on how formation may occur. Indeed, this sample displays swirls on its uppermost layer which were not altered by another nozzle pass above them, in contrast to the specimens tested in this work. Their shape indicates that the initial upward movement may raise the onset of the spiral to a higher location than the one seen when the swirl is embedded inside a layer. These images suggest the occurrence of a collapse. Another formation mechanism taking this into account is therefore also proposed in Figure 6.11:

Scenario 2: Formation of swirl with collapse

(a) Pressure build-up results in material flowing out through a channel underneath the nozzle. Since it meets solid material, it tends to flow out of the nozzle, upwards around the nozzle tip, forming a stem.

(b) The proximity with the nozzle allows part of the molten material to remain in a liquid state, but it starts to solidify from the outside. The flow is directed towards the extremity of the stem, pressure builds up in this location as a stagnation point forms. In other words, all kinematic energy of the fluid is gradually transformed into pressure energy.

(c) The external solidified shell at the tip of the shell yields and allows material to flow out. The shape of the solidified stem, and the action of gravity causes the flow direction to rotate. As time goes by, the solidified walls thicken, shearing the flow and reducing its viscosity, thus allowing it to form thinner spires.

(d) After the spiral has reached a critical size, it collapses under its own weight. Further formation of spires may or may not continue depending on whether collapse happened early with respect to solidification time. Collapse may also happen in a later stage, upon deposition of another layer, as suggested by Figure 6.10.

The main discrepancy between the two scenarios presented in this section is the presence or absence of a collapse step, and the onset of the coiling pattern. In the first scenario presented, the spiraling pattern is due to the exchange of heat between the outer wall and the flow: solidification propagates inwards starting in the material that was directly in contact with the external wall, which effectively prolongs this wall in the flow direction. In the second scenario, the onset of the swirl formation is linked to the combined effects of gravity and of the shape of the solidified walls of the stem, creating a ramp from which material curls. The possibility of a collapse step is confirmed by Figure 6.11, especially as top free swirls are compared to the embedded swirls underneath them: a deformation at the root of the stem can be seen in Figures 6.10c and 6.10d. Since the height of these free swirls is larger than that of a layer, this collapse should happen before the nozzle reaches their location for the deposition of the upper layer: otherwise, the swirl would be deformed upon passing of the nozzle.

In spite of the presence of evidence for a scenario with collapse in Figure 6.11, it is considered that Scenario 1 may also be plausible in the case of the formation of swirls for lower extrusion rates, as no evidence of a collapse has been found in the short beam test samples presented. Moreover, in these samples, the presence of notches with the same semi-circular outline as a swirl but without a spiral pattern shown. Figure 6.12 indicates that the difference between a notch and a swirl may lies in the level of pressure induced by molten material after Step 2: formation of a bulge and expansion, Figure 6.8b. In order to differentiate between these two scenarios, a closer monitoring of the extrusion rate should be carried, as well as a careful observation of the print with for instance a high-speed and high-resolution camera.

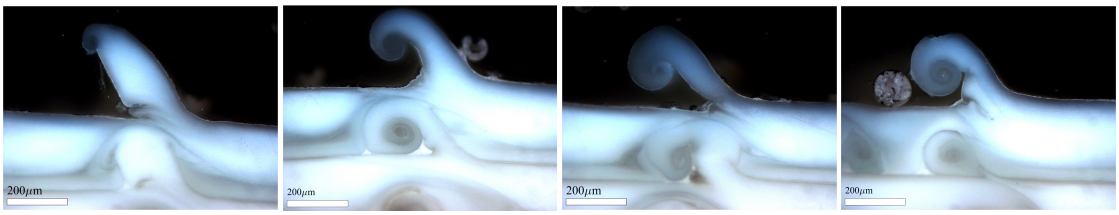

(a) **(b)** **(c)** **(d)**

Figure 6.10 – *Micrographs of an early sample subjected to overextrusion, seen with ×20 objective*

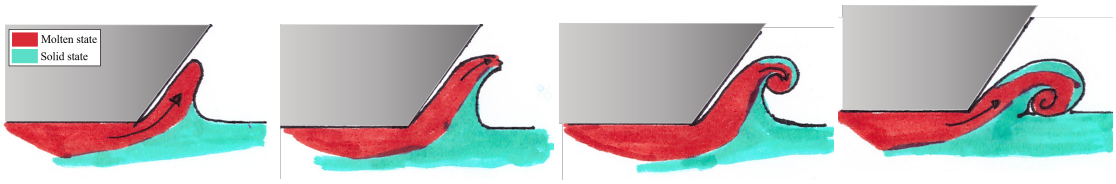

(a) Upward movement along hot nozzle, forming a stem

(b) Pressure build-up at the tip, forming a curl

(c) Shear-thinning, onset of spiral formation

(d) Collapse of the spiral, inner spiral formation continuation

Figure 6.11 – *Suggested formation mechanism for swirl with collapse. In blue: solid state, in red: liquid state.*

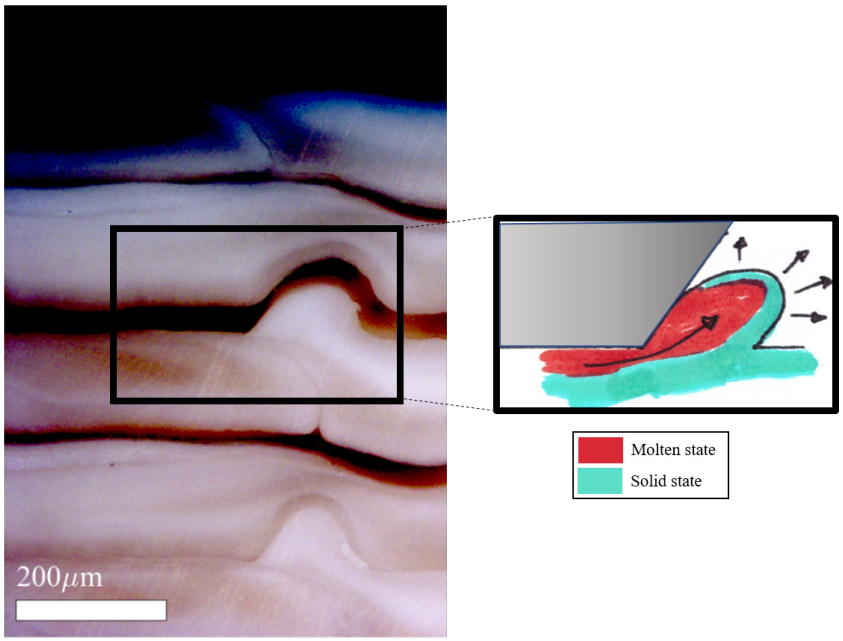

Figure 6.12 – *Micrograph of Sample F85 0.5 090 1 in longitudinal cross-section, seen under polarized light with a ×10 objective. This sample displays notches instead of swirls, also in a semi-circular shape*

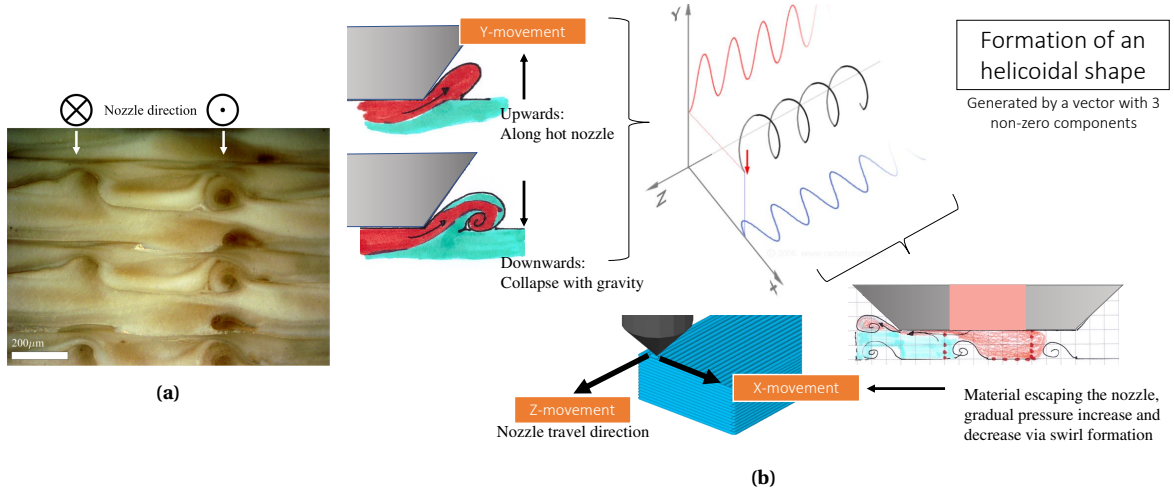

Figure 6.13 – *(a) Micrograph of the longitudinal cross-section of Sample F102 0.5 90 2, with ×10 objective. Printing sequence goes from left to right, printing direction is indicated by the ⊙ and ⊗ symbols. (b) Representation of an helix as a sum of two components (a sine and a cosine) and a propagating direction (Creative Commons 2.0 license)*

6.3.2. Swirls as helicoidal shapes

The scenarios illustrated in Figure 6.8 and 6.11 have been presented as if the formation of swirls were happening in two-dimensions only. However, due to the travel movement of the nozzle, a third dimension is likely to play an important role. This raises a point which has not been studied with data, as the methods employed are only two-dimensional, based on cross-sections of the swirls. However, in light of this remark, one should consider that the swirls may be helicoids, as shown in Figure 6.13b.

Indeed, an helix can be drawn by a vector of three non-zero components, where the x and y components may vary as sine or cosine. In the case of swirls seen in LCPs, a non-zero z-component is linked to the direction of nozzle movement: material is dragged in this direction. The non-zero x-component may be that linked to the fact that the deposited material cannot take the space allocated as has been discussed in Section 6.2.1. The non-zero y-component may be linked to the upward movement described in Step 1 (Fig. 6.8a), as molten material meets solidified material. In order to form an helix, the x- and y-components must vary as trigonometric functions. The variation along the x-axis could be provided by the gradual pressure increase and decrease with the formation of swirls. As seen in Figure 5.8a, their transverse spread is not constant along the z-direction. The variation along the y-axis may be a combination of upward flow guided along the wall of the hot nozzle, and downward flow due to gravity.

An experimental element supporting this remark is that in some cases, only one interlayer out of two is visible as a spiral pattern, as shown in Figure 6.13a: this may also be an indication that the z-component, the direction of nozzle travel, plays an important role.

However, one thing indicating that this explanation is not sufficient is that in most swirls, for instance in Figure 6.7, several spires can be seen, whereas a simple helix produces only one point in the (x,y) plane shown in Figure 6.13b. Therefore, a complete explanation should combine the scenarios established previously with a third component of the swirl formation along the z-direction.

6.4. SUMMARY

In this chapter, the question of the formation of interlayer features is addressed. In a preliminary part, three hypotheses are formulated, and tested. The first hypothesis states that interlayer features form because the material is over-extruded in the nozzle. While it can be noticed as a general trend that interlayer features are more numerous and taller with increasing extrusion percentages, this hypothesis suggests that only samples for which the extrusion percentage is superior to 100% may display interlayer features. However, interlayer features can be noticed on severely under-extruded samples (e.g. 80% extrusion rate): after a number of layers printed with elements symptomatic of under-extrusion such as large gaps between beads, a sharp transition occurs towards a zone displaying no voids and interlayer features. This suggests that over-extrusion is not a necessary condition for interlayer features to develop.

This highlights the need for a conceptual mechanism of formation, in which other parameters may play a role in the formation of swirls. A formation mechanism is thus proposed, and presented in two scales: on the bigger scale, a triggering sequence of events based on an offset between beads shows the interlayer features as a pressure-alleviating mechanism. On a smaller case, the formation mechanism focuses on the formation of one swirl with its spiraling pattern. A body of evidences supports the formation mechanism in both scales. They are also recalled here:

- Interlayer features are located every line width in the transverse cross-section of 3D printed parts. The position of the interlayer feature located on bead N coincides with that of the nozzle tip location as it deposits bead N+1, suggesting that swirls are created by the interaction of the nozzle with previously deposited material.

- Color patterns and boundary lines indicating bead boundaries, shift in the presence of swirls: in the manner presented in Figure 6.2, this offset may be caused by the volume allotted to a bead being already occupied by interlayer features. This phenomenon may lead interlayer features to be self-replicating even in the absence of over-extrusion. The fact that beads are shifting is both supported by microscopic evidence and by the observation on a video of two swirls being created by the same nozzle pass. This latter observation can only be explained by material exceeding the limit of the nozzle tip, thus by the bead being shifted.

- At a big scale, a mechanism is proposed for three different types of bead patterns to self-replicate by forming an interlayer feature, as a pressure-alleviating mechanism. Material previously deposited by the nozzle can melt once more in its contact, creating a zone of molten material in which extruded material can also flow until it reaches the nozzle tip. This is supported by microscopy observation of bead boundary shapes.

- At a smaller scale, two scenarios are proposed for the formation mechanism of one swirl. Narrowing of the flow channel is the reason put forward for two main observations: the presence of a darker, anisotropic center within one swirl can be explained by the higher molecular orientation of the LCP when exposed to shear in the narrower channel, and the presence of several spires within one cross-section can be explained by the shear-thinning properties of the LCP, reducing its viscosity as the channel becomes narrower.

- The formation mechanism may only be complete if these scenarios are transposed in three-dimensions, as evidence suggests that a non-zero component in the direction parallel to nozzle movement may transform the spiral into a helicoidal shape.

- A closer monitoring of the extrusion rate in real-time is essential to further study the impact of over-extrusion on the swirl geometry and to understand what triggers their formation in the first place, in a quantitative manner.

7

Discussion: Reinforcing Potential of Interlayer Features

INTRODUCTION

The preceding chapter has focused on the reasons why interlayer features may occur, and has proposed an explanation mechanism for them. But another question can be asked: *are these interlayer features desirable in a print?* This question necessitates an assessment of their potential at enhancing the performance of a printed part. Indeed, a weakness of Vectra, inherent to the 3D-printing approach but also accentuated by the anisotropy of this material, is the poor mechanical strength at the interface between two layers. It is believed that interlayer features cannot represent an improvement for Mode I-related values, because of their shape and because they do not influence the way two layers could bond together at molecular scale. However, for Mode-II related values (in-plane shear), their shape may provide interlocking between two layers, ideally blocking a delamination until they are plastically deformed. A study of literature gathered in Section 2.2.2 has provided reasons to expect that these interlayer features may improve the interlaminar shear of the specimen, as they provide mechanical interlocking from one layer to the other.

7.1. TEST PHILOSOPHY

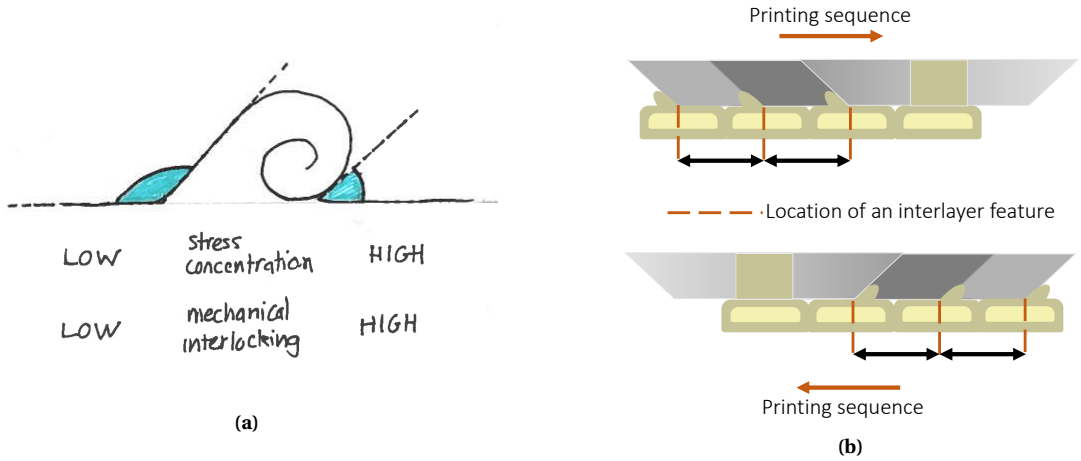

Figure 7.1 – *(a) Schematics of the two different types of angles that can be seen in interlayer features such as swirls. (b) Representation of the consequence of the printing sequences and nozzle geometry on the formation and shape of interlayer features*

The research question asked is: *Does the presence of interlayer features in a 3D-printed part act as rein-*

forcement and enhance interlaminar shear strength? To answer this question, hypotheses that have been formulated in Chapter 3 are recalled here:

Hypotheses on interlayer features as reinforcement material

H2.1 The direction of interlayer features with respect to the delamination propagation front determines whether or not the interlaminar shear strength is enhanced.

- H2.1a) Interlayer features in the direction parallel to the delamination propagation does not enhance the interlaminar shear strength of printed specimens.
- H2.1b) interlayer features in the direction perpendicular to the delamination propagation does enhance the interlaminar shear strength of printed specimens.

H2.2 When the two directions are perpendicular, the geometrical characteristics of the interlayer features at the location where delaminations occur may influence the level of increase in interlaminar shear strength.

- H2.2a Interlaminar shear strength is highest in samples in which delaminations happen on a 90° layer presenting tall interlayer features with a steep outward slope.
- H2.2b In contrast, the influence of interlayer features on interlaminar shear strength does not scale up with their number.

The philosophy behind these hypothesis is as follow: it can be expected that the mechanical interlocking ability of an interlayer features depends on its direction with respect to the shear direction. Two infills are tested in this work: [0] and [0/90]. If the shear load direction is parallel to the longitudinal direction (0°), then interlayer features on a 90° layer are perpendicular to it, while the ones generated by a 0° layer are parallel. In the latter case, an increase in performance linked to the presence of interlayer features is not expected, because the level of mechanical interlocking is negligible: the layers may simply shear along the interlayer feature. This expected discrepancy is described in Hypothesis H2.1.

Hypothesis H2.2 focuses on the link between the geometric parameters describing interlayer features seen on a sample, the delamination path that can be seen on this sample, and its interlaminar shear strength. Indeed, interlayer features are asymmetric, as schematized in Figure 7.1a. Since it is foreseen that the reinforcing ability of these layers is imputed to mechanical interlocking, one has to take into account that swirls tend to have a shallower slope on the side which has been in contact with the nozzle extremity. While for the reasons above, this may not be of importance in 0° layers, in a 90° layer, a sliding movement going along the shallow slope of the swirl will not be restricted as much as if it were happening from its other, steeper side. In a worst-case scenario, one could even imagine how this feature could be counter-productive, with the small and smooth angle acting as a ramp from which layers can be torn apart, adding a mode I-component. A mode-I component should be avoided at all costs given the weak interlayer bonding of Vectra. Therefore, the geometry of the interlayer features may be important to understand in what conditions they can act as reinforcing mechanism.

Two points can thus be investigated in the frame of verification of Hypothesis H2.2. First, the boundary on which delamination propagates in [0/90] specimens, and second, the influence of the number of swirls. This first point is related to the following remark: if the delamination occurs on top of a 90° layer, it has to propagate around an interlayer feature, while if it occurs on top of a 0° layer, its path is straightforward. According to Hypothesis H2.2a, this may play a role in the interlaminar shear. Trends are drawn from microscopy observations of each specimen after test. The second point on the influence of the number of swirls on the interlaminar shear strength is directly linked to Hypothesis H2.2b. It can be verified by varying the number of swirls and comparing the interlaminar shear strength of the two resulting samples. Varying the number of swirls can simply be done by changing the line width of the samples. Indeed, smaller linewidths should create more interlayer features because of the more numerous nozzle passes needed to fill one layer. Changing this parameter is therefore a way to assess qualitatively whether the number of interlayer features has an influence on the interlaminar shear strength.

Table 7.1 summarizes the parameters which have been chosen to test the hypotheses above, as well as

Type of parameter	Values	Comment
Printed line width (mm)	0.5 0.35	If interlayer features have an influence, it can be expected that the more there are, the strongest the interlaminar shear
Stacking sequence (°)	[0] [0/90]	Shear force direction will be aligned with the swirls Half of the interlayer features will be in the direction transverse to shear, which is expected to be more efficient.
Flow multiplier (%)	F102 F90 F85 F80	Overextrusion, producing interlayer features reliably No overextrusion, producing interlayer features unreliably Limited underextrusion, few to no interlayer features, low void content Limited underextrusion, no interlayer features at all, larger void content

Table 7.1 – *Description of the parameters and values chosen in the test*

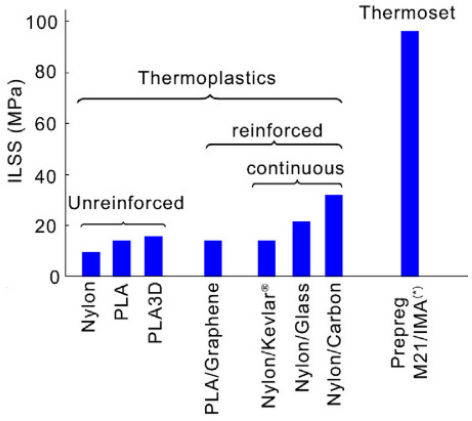

Figure 7.2 – *Comparison of interlaminar shear strength tested via short-beam tests for a range of materials. Extracted from (Caminero et al. [46]).*

their values and the philosophy behind these. Four extrusion percentages have been selected. For simplicity, it would have been desirable to keep the extrusion rate values tested to two: one generating tall and regular interlayer features, the other not - all other things being equal. Since interlayer features have been shown to be more numerous with higher extrusion percentages, one could therefore wish to maximize this parameter. However, this would also affect the part quality with over-extrusion, i.e. unevenness of the surface and other visible defects. Therefore, the choice of these four extrusion parameters is linked to the necessity to find a balance between over-extrusion and the presence of interlayer features.

7.2. Interpretation of the Results

In this section, the results gathered in Section 5.4 will be compared with literature, discussed, and the hypotheses recalled in the previous section will be assessed based on this experimental evidence.

7.2.1. Overall Performance: comparison with literature

A study conducted by Islam et al. [51] discussed in Section 2.2.2 compares the interlaminar shear strength of pristine CFRP laminates to those on which PLA 3D-printed structural reinforcements are added when in the pre-preg state. Layups are $[+45_5/-45_5/90_5/0_5]_s$ and $[+45_3/-45_3/90_3/0_3/+45_2/-45_2/90_2/0_2]_s$. The values obtained in this paper are 5.68 ± 1.2MPa in the former case, and 8.26 ± 0.12 MPa in the latter. In this thesis, the average values found in Figure 5.15 range from 2 MPa in the lowest performing configuration – F85 samples with 0.35mm linewidth and [0/90] layup – to 8.13 MPa in the higher performing samples – F102 samples in [0] layup and 0.5 mm linewidth. Thus the highest performing samples are comparable to the type of CFRP laminate used in [51] in term of interlaminar shear strength.

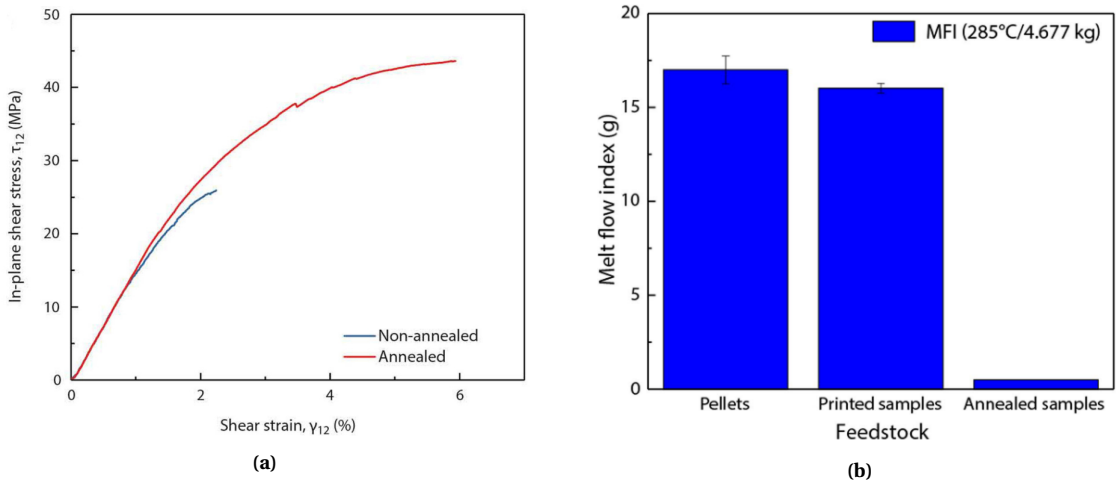

Figure 7.3 – *(a) Shear stress-strain curve of LCP with and without annealing for 96h of ± 45° tensile samples. A 75% increase in in-plane shear strength is reported with annealing. (b) Melt flow index of pristine pellets of Vectra, printed samples without annealing and printed samples after annealing. The much lower value for the latter indicates a very high viscosity, owing to their higher molecular weight due to the cross-links established during annealing. This indicates that annealed materials are not readily recyclable. Both graphs extracted from Gantenbein et al. [1].*

However, another study by Caminero et al. [46] shows different 3D-printed materials: nylon and PLA. At a comparable layer thickness (0.2 mm) to the one used throughout this work (0.15mm) and with a [0] layup, unreinforced nylon samples display an interlaminar shear strength of 9.33 MPa. This can be compared to the 6.36 MPa found for F102 samples in [0/90] layup and 0.5 mm linewidth, and the 8.13 MPa found for F102 samples in [0] layup and 0.5 mm linewidth. In spite of being in the same range as Nylon, Figure 7.2 highlights that the ILSS of unreinforced thermoplastics is up to 2 orders of magnitude lower than some thermosets.

In Gantenbein et al. [1], in-plane shear strength has been measured with ± 45° tensile samples. A representative curve can be found in Figure 7.3a. The authors report an increase of 75% for the in-plane shear strength by annealing the samples. Indeed, as mentioned in Chapter 2, annealing allows solid-state cross-linking via a transesterification reaction. Covalent bonds can be created between printed layers, resulting in higher layer adhesion and higher in-plane shear strength as shown in Figure 7.3a. As a result it may also be expected that annealed samples may outperform non-annealed samples in interlaminar shear strength. However, annealing comes at the cost of greatly undermining the potential of recyclability of the printed parts, as shown in Figure 7.3b, while the improvements in interlaminar shear proposed in this work do not impact the recyclability of this material as they rely on mechanical interlocking of layers.

7.2.2. Interlayer features parallel to shear direction

Hypothesis H2.1a states that *"Interlayer features in the direction parallel to the delamination propagation does not enhance the interlaminar shear strength of printed specimens."*. In this section, its validity will be discussed. Then, possible explanations will be established for the observation made.

Lack of improvement in unidirectional specimens

According to Figures 5.15 and 5.16, no statistically significant increase in interlaminar shear can be found between unidirectional samples displaying interlayer features, and others which do not. However, a comparison of mean short beam strength may be criticized due to the relatively large scatter between samples, as shown in Figure 5.14. One can thus also make use of the microscopy observations to compare samples individually when they display interesting features. For instance, some samples appear free of voids and do not display notch or swirl features at all, as shown in Figure 7.4. Even though small notches are still present, these samples appear to be a good trade-off between absence of large inter-layer features and absence of undesirable side-effects such as voids. As a result one can use them as a baseline for assessment of the effect of swirls. Their performance lies

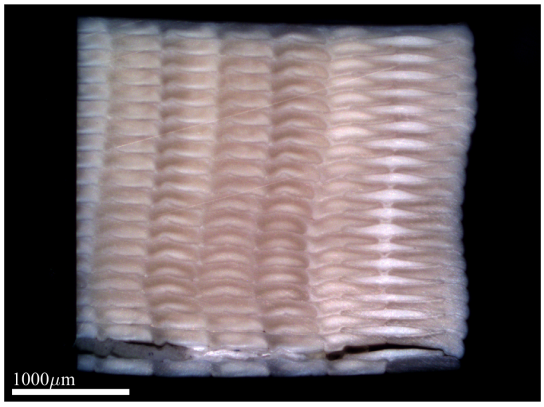

(a) F85 0.5 0 4 could be a baseline sample for the comparison as it does not display any void or interlayer feature. Its SBS is 8.06 MPa.

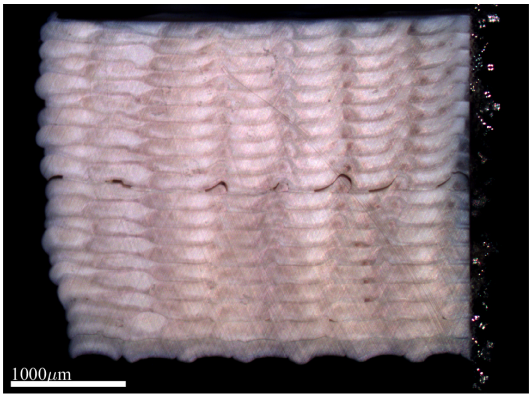

(b) F102 0.5 0 4 does not display any void but does have regular interlayer features. Its SBS is 7.51 MPa.

Figure 7.4 – *Comparison of two samples for which only the extrusion rate varies. Left sample may be a baseline for comparison to the F102 samples as it does not show voids or interlayer features. The SBS of this sample is in the same range as that of the mean F102 samples: 8.06 MPa vs. 7.95 MPa. The fact that they perform similarly shows that in the unidirectional configuration, interlayer features do not enhance the interlaminar shear strength of a sample.*

in the average of the F102 samples, which themselves display swirls. This indicates that for the unidirectional samples, swirls do not seem to lead to a strong increase in performance in interlaminar shear strength, in line with Hypothesis H2.1a. More precisely, one can conclude that the difference in layer profile between very small notches and tall swirls is not significant enough to produce differences in interlaminar shear strength noticeable with the current level of scatter in the samples.

Elements of explanation: no variation in crack-front shape

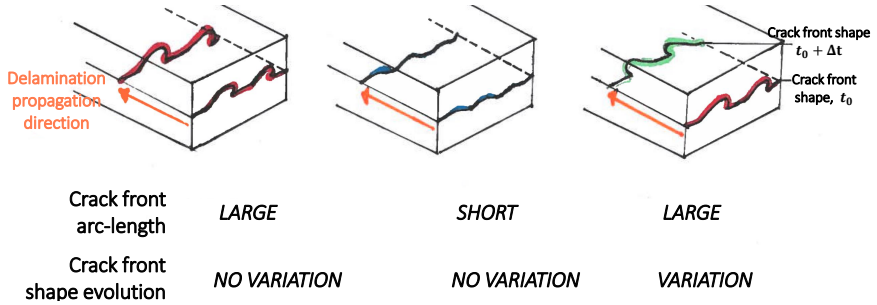

Figure 7.5 – *Schematics of the crack front evolution depending on the interface type: (left) presence of unidirectional interlayer features, (middle) absence of interlayer features, (right) hypothetical interface type in which the crack-front arc length is large, and the shape of the crack front does change along the delamination propagation direction. This latter case provides high mechanical interlocking but has not been produced experimentally.*

When cracks propagate in laminated structures, two elements in the geometry of the crack-front matter: its length, and the variations of its geometry along the propagating direction. This concept is illustrated in Figure 7.5. Since the mechanical test results of unidirectional samples indicate that no increase in short beam shear strength can be seen between samples with tall interlayer features and those without, it can be put forward that for this material, the larger arc-length of the crack front shape does not enhance interlaminar strength. While it is observed that the arc-length of the crack front varies between the two broad sample configurations (absence or presence of tall interlayer features, respectively middle and left cases shown in Figure 7.5), one should also bear in mind that theoretically, due to the 0° infill, the shape of the crack-front does not evolve along the delamination direction in both cases. If such assumption is verified experimentally, it could be concluded that for Vectra, it is the evolution of the crack-front shape along the propagation direction which matters the most, rather than the crack-front arc-length, at any given point of the delamination path.

This fact can also be argued from a mechanical interlocking point of view. In a specimen printed at an infill

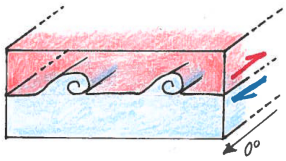

Figure 7.6 – *Schematics of shear direction encountered by the 0°layers*

orientation of 0°, a shear deformation in a direction parallel to the bead, will not encounter a large resistance due to mechanical interlocking if both types of features (small notches and swirls) are 'cylindrical' features along which layers can slide easily, as is shown in Figure 7.6. Unfortunately the level of regularity of inter-layer features along the delamination propagation direction could not be measured with the present setup.

7.2.3. Influence of the number of interlayer features

Hypothesis H2.2b states that "*the influence of interlayer features on interlaminar shear strength does not scale up with their number.*". Indeed, no significant difference can be noticed in short beam strength between the two linewidths, 0.35mm and 0.5mm, although the number of interlayer features is higher for smaller linewidth, due to the more numerous passes of the nozzle. This higher number increases the arc-length of the crack-front in the 0.35mm configuration. This is in keeping with the supposition established in the previous paragraph, that crack-front length does not influence the interlaminar shear strength. It can thus be concluded that in the configurations tested here, increasing the number of interlayer features does not enhance interlaminar shear strength.

7.2.4. Interlayer features in the direction perpendicular to shear

According to hypothesis H2.1b, "*interlayer features in the direction perpendicular to the delamination propagation enhance the interlaminar shear strength of printed specimens.*". In this section, its validity will be discussed. Then, possible explanations will be established.

Linewidth (mm)	Under-extruded Average SBS (MPa)	Over-extruded Average SBS (MPa)	Percent increase (%)	Under-extruded, Average Normalized SBS (MPa/g)	Over-extruded, Average Normalized SBS (MPa/g)	Percent increase (%)
0.35	2,76	5,86	112%	8,40	15,41	83%
0.5	3,28	6,36	94%	10,56	17,29	64%

Table 7.2 – *Comparison of average values of [0/90] samples, under-extruded (i.e. F80, F85, F90) to over-extruded (F102)*

Elements of explanation

According to Figures 5.18 and especially 5.19 which takes into account the mass gain of samples, a general increase in interlaminar shear can be found between [0/90] samples displaying interlayer features, and others which do not. An increase of close to 80% can be found by comparing the underextruded samples (F80 to F90) to the over-extruded case (F102), even after having taken into account the mass increase in F102 specimens, as highlighted by Table 7.2. Mechanical interlocking is the primary reason why interlayer features may enhance the interlaminar shear strength of a sample. However, this hypothesis represents a trend, and so does the mean of all specimens within one configuration, which is why the two agree well.

Contradictions

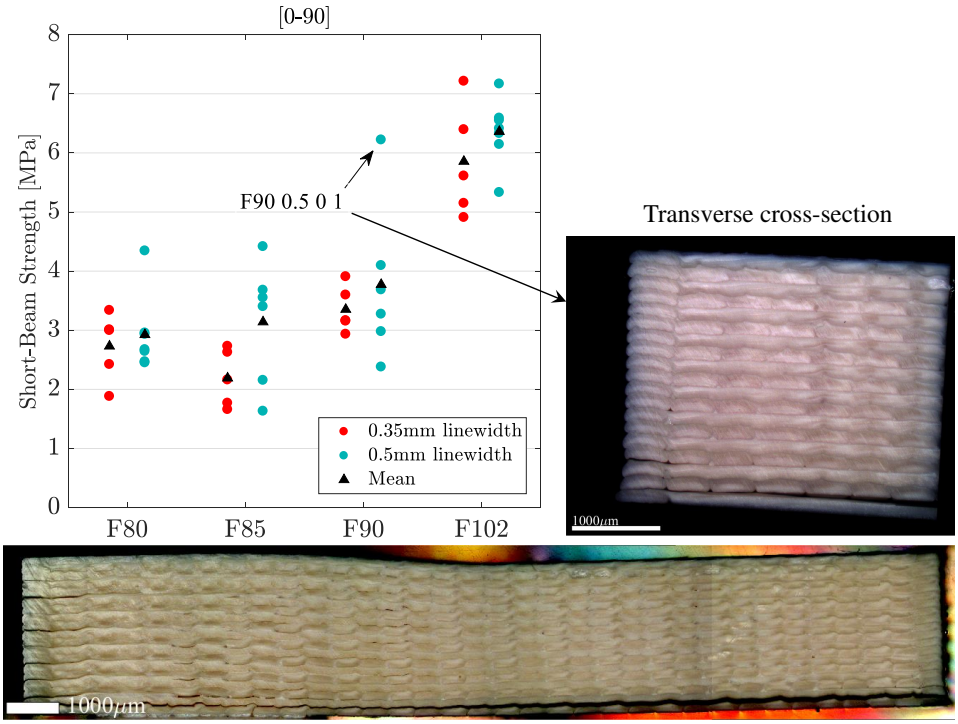

Figure 7.7 – *Sample F90 0.5 0 1 performs as well as the average F102 sample, while both its transverse and longitudinal cross-sections do not show the presence of tall interlayer features.*

In reality, this hypothesis does not fully capture the behaviour of samples individually. The limitations of this hypothesis can be highlighted by looking at the microscopy observations and at the scatter which can be found for instance in the F90 series, displaying tall interlayer features. Indeed, several samples seem to contradict the fact that interlaminar shear is enhanced by presence of interlayer features: one may notice from Figure 5.19 that F90 samples perform less well in average than F102 samples by almost a factor two, while at the same time displaying tall notches. Another prime example is Sample F90 0.5 090 1, which performs as well as the average F102 sample in spite of not displaying any visible swirl, as summarized in Figure 7.7.

These elements indicate that the relationship between the presence of swirls and higher performance is not straight-forward. The general trend shown in Figure 5.18 does seem to indicate that the presence of swirls or tall and sharp interlayer features may enhance the interlaminar shear strength of the specimens. However, the presence of swirls is not a sufficient condition for increased mechanical performance, and in fact, it is not even a necessary condition either: the example of Sample F90 0.5 090 1, as mentioned previously, suggests that other factors than the presence of swirls may also increase greatly the interlaminar shear strength. Moreover, the presence of tall notches in some F90 samples does not prevent them from under-performing the F102 samples, suggesting that another parameter than their mere presence might be at play.

7.3. Reinforcing potential of interlayer features: classification according to delamination type

7.3.1. Presentation of the classification

Delamination surrounding zone	Notch front encountered by delamination	Layer supporting the delamination [°]	Nomenclature
Absence of marked interlayer feature		0	**A-0**
		90	**A-90**
Presence of marked interlayer feature	Shallow slope	0	**B1-0**
		90	**B1-90**
	Steep slope	0	**B2-0**
		90	**B2-90**

Table 7.3 – *Nomenclature differenciating delamination types based on the raster angle of the layer on top of which it can be found, and the presence of interlayer feature.*

As one may recall from Figures 7.1a and 7.8, it has been hypothesized that a delamination meeting a steep angle may more likely be arrested, than if it had met a shallower angle. In the latter case, the swirl might act as a 'ramp' from which the layers might separate further away from each other, instead of a crack-arrest feature. A classification is established in order to understand what may cause scatter within one series and to see whether this hypothesis is represented by data. This classification, presented in Table 7.3, indicates that a distinction should be made among samples displaying marked interlayer features: not only the presence, but also the geometry of the interlayer feature should influence the specimen interlaminar shear strength. The features that matter in this classification are the the delamination surface, the height of a feature, and the angle of the notch front encountered by the delamination, assuming that the latter progresses from the outer sides of the specimen inwards. In order to verify Hypothesis H2.2, this classification is submitted to the [0/90] specimens. Examples are provided in Figure 7.10 to further show what is meant by each delamination type. The results of this classification are then discussed in this following section.

As shown both in Figure 7.10 on real samples, and on the bottom schematics in Figure 7.8, the difference made in the classification between B1 and B2 is linked to the geometry of the interlayer features, which often are not symmetric, and may display a smooth angle on one side, and a sharper one on its opposite side. The classification takes into account the angle of the interlayer feature which is first encountered assuming the delamination travels inwards, i.e. the outermost angle, and classifies it between 'steep' and 'shallow', with the distinction being relative to the opposite angle, as shown in Figure 7.1a. If both slopes appear symmetric, an angle larger than 60° may be considered steep and the sample put in category B2. Else it falls into Category B1. In a nutshell, samples that are gathered by the B1-delamination types are specimens on which a marked notch pattern can be seen, but on which the slope of the notch first encountered by the delamination is shallow.

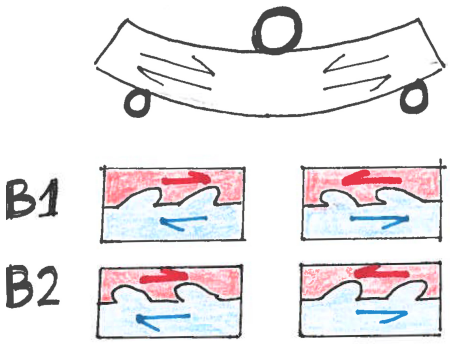

Figure 7.8 – *Top: deformed shape with expected shear resultants. Bottom: B1 and B2 configurations, depending on the slope of the specimen.*

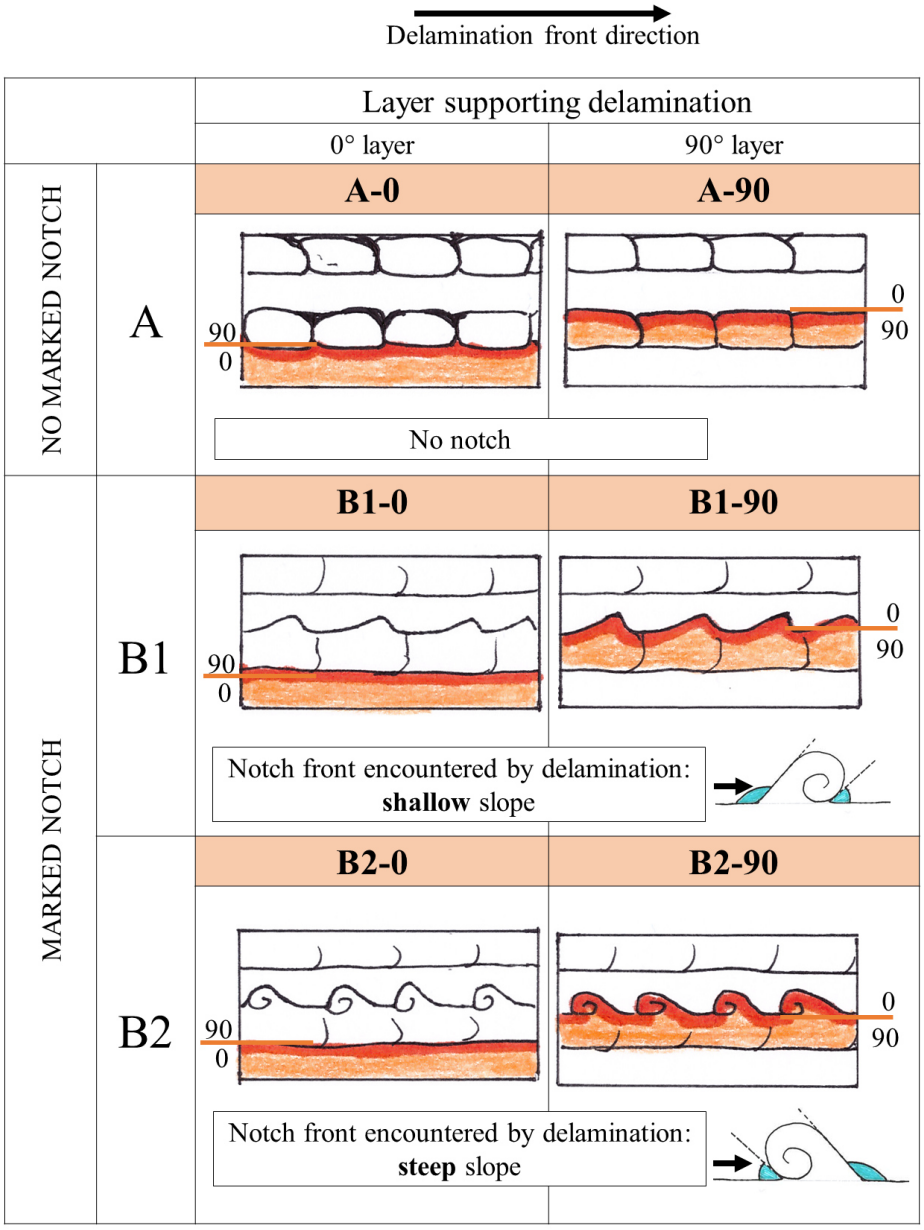

Figure 7.9 – *Schematics of the classification used to distinguish between samples*

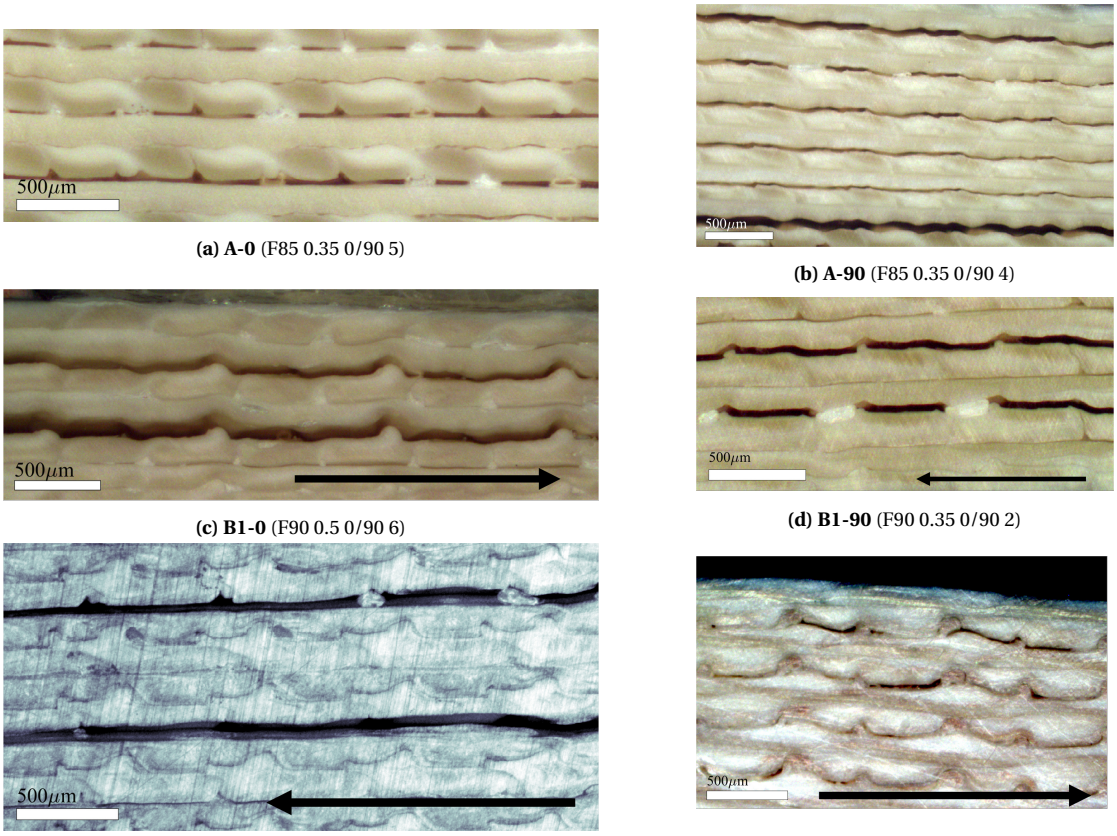

(a) A-0 (F85 0.35 0/90 5)

(b) A-90 (F85 0.35 0/90 4)

(c) B1-0 (F90 0.5 0/90 6)

(d) B1-90 (F90 0.35 0/90 2)

(e) B2-0 (F102 0.35 0/90 4)

(f) B2-90 (F102 0.5 0/90 4)

Figure 7.10 – *Close-ups of micrographs of samples which are representative for one delamination type described in Table C.2. The letter (A, B) denotes whether tall interlayer features can be seen, (0, 90) indicates the bottom layer type on which delamination propagates, and (B1-B2) indicates whether the delamination front encounters the interlayer feature at a shallow slope, or at a steep one. The propagation of the delamination front is shown with a black arrow.*

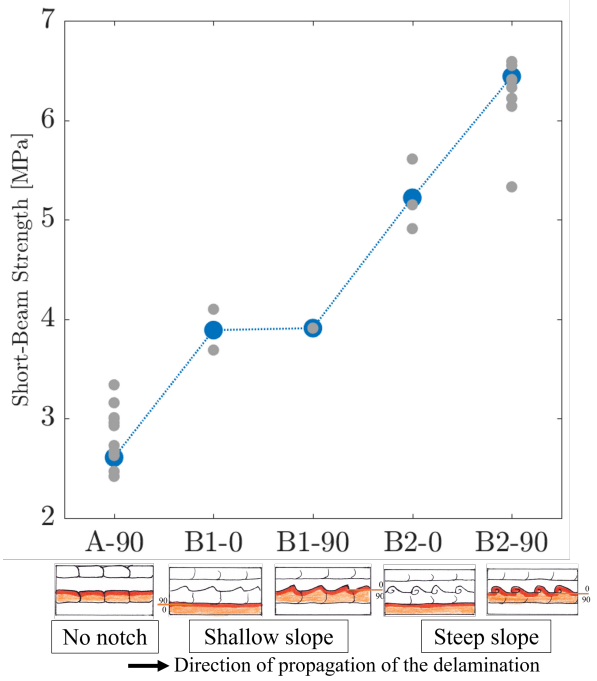

Figure 7.11 – *Mean short-beam strength of samples according to their delamination type (blue), and short-beam strength of samples for which the mean is calculated (grey). Only samples displaying one delamination type are taken into account.*

	F80		F85		F90		F102	
	0,35	0,5	0,35	0,5	0,35	0,5	0,35	0,5
A-0			1	3	1	2		
A-90	5	7	5	5	3	1		
B1-0					2	4		
B1-90				2	2	2		
B2-0		1					3	
B2-90		2		1		1	2	7

Table 7.4 – *Distribution of delaminations according to extrusion multiplier and linewidth. Numbers indicate the amount of specimens on which the corresponding type of delamination was observed. Some specimens appear several times as they delaminate in multiple manners.*

Each [0/90] sample is classified according to this nomenclature in Figure 7.11 and Table C.2. Samples may display more than one delamination types, and may therefore appear several times in Table C.2. In contrast, only samples displaying a single delamination type are shown in Figure 7.11. One can see that the number of specimens accounted for in the graph vary greatly, with only one specimen in the B1-90 case and 15 in the A-90 case: this highlights the fact that a large amount of samples delaminate in multiple manners, belonging to up to three classifications. The exact break-down of what delaminations types are displayed for each sample is shown in the Appendix, Table C.3.

7.3.2. Discussion on the classification established

It has been hypothesized that "*Interlaminar shear strength is highest in samples in which delaminations occurs on a 90° layer presenting tall interlayer features with a steep outward slope*" (Hypothesis H2.2a). Using the classification established in Table 7.3, this is equivalent to the following: "B2-90 specimens perform better than their peers". This hypothesis focuses on the [0/90] samples and tries to find possible explanations for the contradictions to Hypothesis H2.1b raised by individual samples in the previous section. In this section, the validity of this statement will be discussed, in two separate parts: the influence of the geometry of the interlayer features on the interlaminar shear strength, and the possible reasons why delaminations appear on 0° layers or on 90° ones. Trends brought to light by the classification of Table 7.9 will also be presented as they are closely related to this hypothesis. Then, possible explanations will be established.

Influence of the geometry of the interlayer feature on the performance of the samples

B2-90: top-performing samples

All the top-performing samples, those reaching 6 MPa, have delaminated in the B2-90 manner, i.e. with the delamination following the tortuous 90°layer profile, effectively being stopped as it encountered the steepest slope of the interlaminar feature – except the F90 0.5 090 1 sample mentioned earlier. In this manner, these samples can reach the interlaminar shear of the average unidirectional sample. This trend is captured in Figure

7.11, where samples displaying only one type of delamination have been taken into account. This is a strong argument in favour of hypothesis H2.2a described above. Another point that these top-performing specimens share in common is the large number of delamination sites: i.e., delaminations have not propagated and remained within the boundaries of two interlayer features, as shown in Figure 7.10f or Figure 7.12, indicating they may indeed act as crack-arrest.

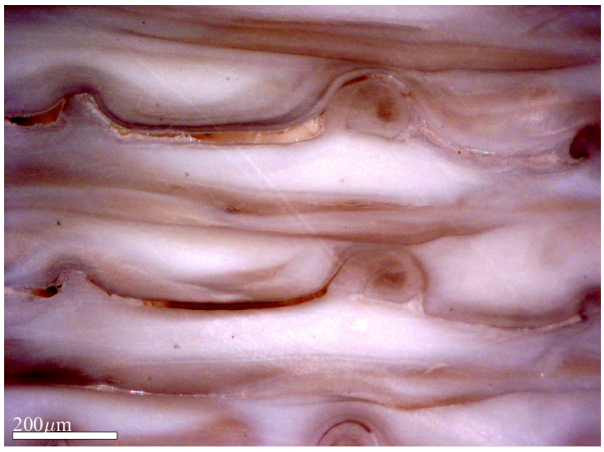

Figure 7.12 – *Close-up with a ×10 zoom of sample F102 05 090 4, on which the delamination is contained on a small zone and stopped at the corner of a swirl.*

B1 vs B2: increase in interlaminar shear strength when delaminations meet steep slopes
As mentioned earlier, a component of the difference between samples in Category B1 and B2 is the side (left or right) where delamination started. Samples in Category B1 delaminated from the side where the smoothest angle is outwards. Samples in Category B2 delaminated from the side where the sharpest angle is outwards. In both cases, the delamination could also have started from the opposite side, which would have resulted in the sample being placed in the other category, unless the angles were considered symmetric, as shown in Figure 7.8. Regardless of why delaminations happened in one side or the other of the sample, the fact is that short beam shear strength is higher when delaminations started in zones where steep slopes can be found directed outwards of the specimen. As shown in Figure 7.11, an increase of 45% in average short beam strength can be found between the two delamination types. This may indicate a difference in propagation of the delamination between both cases, with the propagation being facilitated in the B1 category and hindered in the B2 category.

These elements indicate that interlayer features may in fact only be useful if they are used against the delamination propagation, with a steep angle, and a certain height (from approximately 50% of the layer height), else their effect is negligible. Even though it can be argued what the direction of propagation of delaminations can be, one can still conclude that a symmetric profile would be a desirable feature for higher robustness, as a delamination propagating from either side, or an opposite shear deformation, would be handled in the same manner by the specimen. Sample F102 0.5 090 3 displays this symmetry, illustrated in Figure 7.13, and performed the best in its category.

Delamination surface along the 0° or 90° layer: role of interlayer features in attracting a delamination

If interlaminar shear increases as samples display steeper and taller interlayer features, the fact is that some samples displaying tall and sharp interlayer features still delaminate along the 0° direction (B2-0): among the F102 samples, 25% do not delaminate in a B2-90 but rather a B2-0 manner. These samples are the lowest performing of their series, with a loss in performance up to 2 MPa, and a crack length longer by 3 to 4 times. One can understand why delaminating above the 0° layer could cause a drop in performance, as it follows a straight path with no crack-arrest feature delaying its propagation. However, the mechanism which triggers one or the other type of delamination is not well understood. It would be extremely useful to understand why a delamination surface may form on a 0° layer or on a 90° one, in order to make sure that it can be directed in a zone with interlayer features to minimize its propagation.

In fact, one can argue the following to explain why some samples may delaminate upon their 0° interface while some other would delaminate on the 90° one: two competing mechanisms are always at play, as delaminations can either appear in the path with the most stress concentration, or in the least tortuous path. One may easily imagine how the uneven 90° layer interface would act as the former, and the 0° layer interface as the latter. In this sense, sharp interlayer features can be seen as stress-raisers, attracting delaminations on the 90° layers. The sharpest the angle of the notch, the higher the stress concentration in this small zone (see Figure 7.13a), and the likeliest the delamination will appear in this layer. Once this has happened, the crack can be arrested due to mechanical interlocking, and interlaminar shear of the specimen enhanced.

In other words, in order to act as crack-arrest features, the interlayer features should attract the crack in the first place. In order to do so, they should ideally present a tall and sharp front to generate as much stress concentration as possible when layers are shearing. A key challenging aspect if one were to optimize the mesostructure of the 3D-print for increased interlaminar shear, would be to ensure that delaminations only appear in the 90° layer interface, and to avoid at all costs the 0° layer interface as no crack-arrest feature would stop it from progressing.

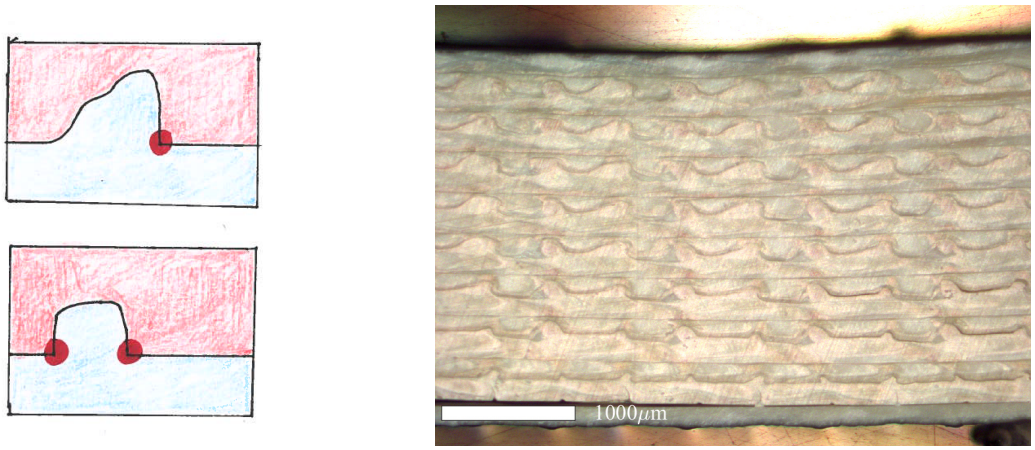

(a) **(b)**

Figure 7.13 – *A symmetric profile of the notch may enhance the interlaminar shear of the specimen. (a) Schematics of two configurations. Top: stress concentration may be highest when shear is negative (zone concerned by the delamination is sharp, highlighted in red.) than when shear is positive. Bottom: the stress concentrations in the notch are affected regardless of the shear type due to its symmetry. (b) F102 0.5 090 3 sample has tall symmetric notches and has the highest interlaminar shear of all the [0/90] samples.*

7.4. SUMMARY

Short beam tests have been carried on samples with varying extrusion percentages and varying infill stacking sequences. In this chapter, these mechanical tests have been discussed based on several hypotheses. In an attempt to get rid of an undesirable side-effect the variation in extrusion percentage, the results are normalized to the mass of each specimen. The results show a trend towards an increase in interlaminar shear with higher extrusion percentages. Since samples of the same configuration may sometimes have different mesostructures and/or very different interlaminar shear strength, they are classified according to the delamination type they display and the presence of small or tall notches. This procedure allows to draw a number of conclusions, presented here:

7.4.1. Unidirectional configuration

- Increasing the extrusion parameter does not lead to a statistically significant increase in short beam strength. The difference in layer profile between very small notches and tall swirls does not produce differences in interlaminar shear strength in unidirectional samples.
- Reducing the linewidth parameter does not lead to a statistically significant increase in short beam strength. Therefore, increasing the number of interlayer features does not enhance interlaminar shear strength in the unidirectional samples.

7.4.2. [0/90] configuration

- A statistically-significant higher short beam strength can be seen in the over-extruded samples displaying tall interlayer features in the 90° direction. This indicates that these can indeed act as reinforcing features, provided they are laid out perpendicular to the shear force direction.
- Similarly to the unidirectional samples, no difference in short-beam strength can be seen between samples with 0.35mm- and 0.5mm-linewidth, suggesting that the influence of interlayer features does not scale up with their number.
- Among samples displaying marked interlayer features, those performing the best tend to be taller, present their steepest profile outwards, and delaminate along their 90° layer interface.

These experiments shows in a qualitative manner that swirls and other interlayer features can act as crack-arrest mechanisms. These interlayer features open possibilities of tailoring the interlaminar shear of samples so that, for instance, a zone of the 3D-printed part may be sacrificed as a 'structural fuse'. However, achieving such results will be contingent on reducing the scatter between printed specimens, which requires a tighter control over the parameters influencing the geometry of the interlayer features.

III

Conclusion

8

Outlook

Continuous fiber printing and additive manufacturing of liquid crystal polymers face one same challenge: attempting to reinforce the in-plane properties with increased anisotropy often comes at the expense of interlayer properties. Anisotropy is, of course, inherent to the 3D-printing approach, as bonds are created between layers and within one layer, between printed lines. But this anisotropy is intensified in both cases by the molecular orientation. Even though "fibers" can only be deposited in-plane, through-the-thickness reinforcements would be desirable. As shown in more details in Chapter 2.2.2, several studies have tried to address this issue with varying success. In this context, this thesis focuses on the study of a feature noticed in printed liquid crystal polymer parts, and attempts to verify whether this feature improves the interlayer properties of a part by producing mechanical interlocking between its layers.

8.1. SIGNIFICANCE OF THE CURRENT WORK

As mentioned earlier, an obstacle preventing the application of Vectra in a large number of use cases is the poor adhesion between layers. Gantenbein et al.[1], authors of the work reporting this material as feedstock for 3D-printing for the first time, have circumvented this problem by annealing the samples. Indeed, Vectra is a material which can establish cross-links between polymeric chains via trans-esterification. In this manner, better adhesion between layers can be found: in-plane shear is enhanced by 75%. However, annealing is a post-processing step that greatly undermines the recyclability of the printed parts. In this context, cross-sections of printed LCP parts are reported in this work for the first time. They reveal the presence of interlayer features, made of material from one layer overstepping onto the space allotted to the upper layer in a crenelated manner, as shown in Figure 8.1.

These observations naturally lead to two questions: *how are these interlayer features formed during a print?*, and *can they be useful to enhance the mechanical performance of a print?* Indeed, their crenelated shape strongly suggest they may provide mechanical interlocking between layers, and enhance the interlaminar shear strength of a sample. As will be detailed in the upcoming section, the reinforcing capability of

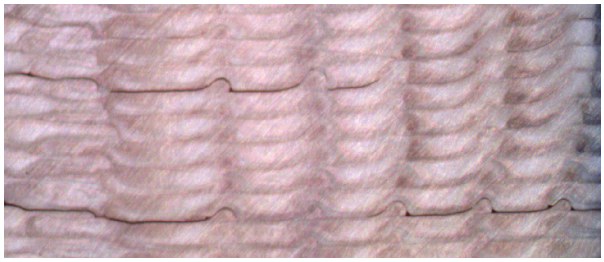

Figure 8.1 – *A test-sample (F102 0.5 0 1) printed with a [0] stacking sequence, where the 0° direction is normal to the plane of this page. This micrograph therefore shows printed lines in their cross-section. Two delaminations outline the shape of layers: instead of being straight, they are crenelated by the regular interlayer features*

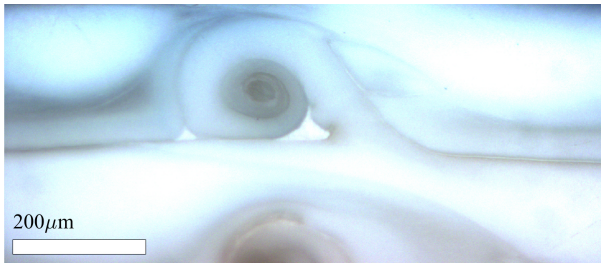

Figure 8.2 – *An early sample, zoomed-in on a spiraling pattern, also called swirl.*

these interlayer features has been established in the case where they are oriented transverse to the shear load direction. A large number of benefits emerge: beyond the much called-for improvement in interlaminar shear, interlayer features are reinforcements which have the advantage of being intrinsic to the part printed. As such, these interlayer features make the LCP belong to the category of self-reinforcing structures. Furthermore, no additional step or post-processing step is needed, maintaining a manufacturing simplicity, which is at the core of the philosophy of additive manufacturing. Last but not least, the recyclability potential of the part is not undermined with this reinforcing method.

A closer look at these interlayer features allows one to see the distinctive shape of a spiraling pattern, called *swirl*, as illustrated in Figure 8.2. Such a spiraling pattern, although often found in nature, has, to the author's knowledge, never been reported, either in the context of liquid crystal polymers, or in additive manufacturing. Therefore, this pattern is a feature worth-investigating in itself, even if no application as structural reinforcement were found. This pattern develops during print. Although the current set-up does not allow for in-situ observation, a mechanism of formation of these interlayer features is still proposed in this work. This mechanism is deemed to be coherent with the body of evidence formed by indirect observations, such as optical microscopy of printed samples cross-sections.

8.2. MAIN CONCLUSIONS

Two main kinds of experiments have been carried in this thesis: short-beam strength tests for apparent interlaminar shear strength, and microscopy observation under polarized light of the cross-sections of the mechanically tested samples. For these tested samples, three parameters have been varied: width of the printed lines, infill angle direction, and extrusion rate, with respectively 2, 2 and 4 values tested. This work has been divided into two core parts: in Chapter 7, the ability of the interlayer features to increase the interlaminar shear strength of a 3D-printed part is discussed. In Chapter 6, the question of the formation of interlayer features is addressed. The conclusion of these two parts are gathered in the upcoming paragraphs.

8.2.1. Interlayer features as reinforcements in interlaminar shear

Short-beam shear test is a 3-point bending test providing an apparent interlaminar shear strength for comparative purposes, which fits well with the aim of this work: a proof of concept showing interlayer features are effective as interlaminar shear reinforcements. Conclusions of these tests are as follow:

For the two infill types shown in Figure 8.3, it is found that the number of interlayer features, varied by changing the width of the printed lines, does not have a statistically significant impact on the mechanical performance of the samples. In other words, in the current state of the experiment, scatter indicated by the standard deviation does not allow to conclude on the question of the influence of the number of interlayer features. At this point of the research, two answers are still plausible: either the influence of interlayer features does not scale up with their number, or small variations may still exist but are too small to be observed considering the scatter in the data.

In contrast, a strong difference between unidirecional and [0/90] samples can be noted with respect to the extrusion rate: unidirectional samples do not display any increase in interlaminar shear strength with increasing extrusion rates. However, [0/90] samples do, which indicates that the direction of the interlayer feature

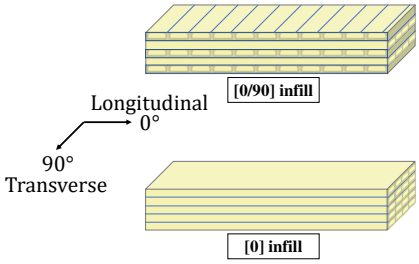

Figure 8.3 – *Short beam test samples illustrated with the two infill types used in this work, with angle convention*

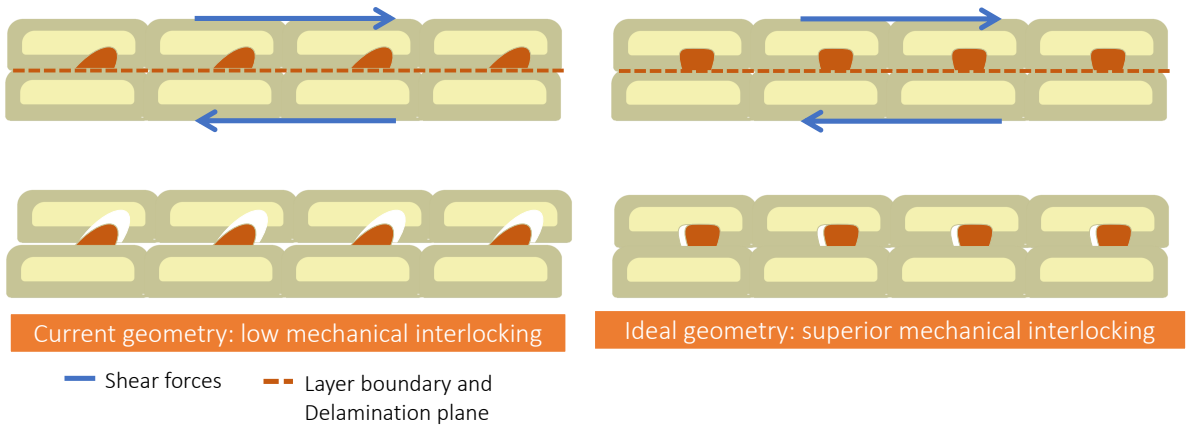

Figure 8.4 – *Comparison of two geometries of interlayer features, subjected to the same shear load: due to the current asymetry of the interlayer features, the level of mechanical interlocking provided changes depending on the shear direction. In the top image, the interlayer feature with a smooth slope may effectively act as a 'ramp' adding a mode-I component to the fracture. In contrast, a symmetric interlayer feature does not cause such a side-effect.*

influence its reinforcing capabilities. It is shown that an average improvement of up to 112% can be found in short-beam shear strength, between over-extruded samples displaying tall swirls and under-extruded samples, when interlayer features find themselves in a direction perpendicular to the delamination propagation.

Microscopy observations show that interlayer features may also appear in samples which are under-extruded. Thus, the cross-sections of individual samples are observed and classified according to the delamination type they display and the presence or absence of marked interlayer features. The limitations of this configuration are highlighted: the number of samples available for comparison varies greatly, as only samples displaying one type of delamination can be compared. However, this classification still indicates a large increase between presence and absence of interlayer features for the samples available for comparison. For instance, an increase of 174% in short-beam strength is observed between samples displaying no marked interlayer feature, and those for which a specific combination of characteristics are found: tall interlayer features meeting the delamination front with a steep angle; and delaminations starting on the interface where they can effectively act as crack-arrest – in contrast to a delamination starting on a smooth 0° layer.

These experiments indicate in a qualitative manner how interlayer features can be used as crack-arrest features. However, a good control of the geometry of the interlayer feature appears important: to be most effective, it appears the interlayer features may have to be tall and symmetric with steep slopes on both sides, as shown in Figure 8.4. This geometry seeks to optimize several aspects: enhancing mechanical interlocking, increasing the tortuosity of the crack path, but also increasing the sharpness of angles to act as stress-concentrators. This apparent paradox is a 'divide-and-conquer' philosophy: raising the stress in the 90° layers helps triggering the onset of delaminations close to the interlayer features, where the crack will need the largest energy levels to propagate. In this manner, multiple delamination sites occur, but are restricted to areas

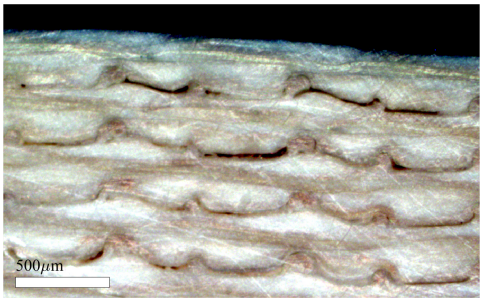

Figure 8.5 – *Micrograph of an overextruded sample in which multiple delamination sites are restricted between interlayer features. (close-up onto the longitudinal cross-section of sample F102 0.5 090 4, optical microscope with polarized light)*

within two interlayer features, as shown in Figure 8.5.

8.2.2. Formation of interlayer features

In Chapter 6.2, the question of the formation of interlayer features is asked. Two facets of this question are addressed: *why*, – i.e. what are the parameters that cause its formation; and *how* – what sequence of events leads to the observations gathered.

It has been hypothesized that the extrusion percentage is the key parameter which influences the presence of interlayer features. However, while tall and regular features are seen to be more numerous when increasing this parameter, in the current test set-up, their presence is more determined by a probability increasing with extrusion percentage than a systematic causal relationship. Such a relationship is explained by the combination of experimental factors and the self-replicating ability of swirls: when a local disturbance in the extrusion rate linked to the unevenness of the filament occurs, it causes one line to be wider than expected. As a result, the distribution of material is affected throughout the rest of the layer. Similarly if an interlayer feature is created on one layer, it occupies volume that should have been allocated to the upper layer. Consequently, during printing of this upper layer, too much material is extruded compared to the available space, resulting in apparent over-extrusion.

Following this line of thought, one can see how the presence of regular interlayer features on the deposition surface affects the distribution of beads: the expected layout is altered in such a way that the available space for the material deposited by the nozzle is gradually shifted farther away from the bead deposition zone. Swirls are considered in this work to be the result of a pressure alleviating mechanism: as the nozzle opening is partially blocked by the previously deposited bead, pressure is higher than expected inside the nozzle. Two escape routes are used by the extruded material. It can of course leave through the small opening left in the nozzle hole, but one has to also bear in mind that Vectra has a low enthalpy of fusion: a fused bead can solidify with a low thermal energy input and inversely, a bead that has already solidified before can melt again in contact with the nozzle depositing its neighbour. As a result, material previously deposited by the nozzle can melt once more in its contact, creating a zone of molten material in which extruded material can also flow until it reaches the nozzle tip, forming a notch with the imprint of the nozzle tip shape: the interlayer feature.

The question of the formation of interlayer features is then further centered around the formation of a spiraling pattern in particular, as shown for instance in Figure 8.2: in this thesis, two scenarios are proposed for the formation of such a spiral, available in Figures 6.8 and 6.11. These scenarios rely on two important characteristics of Vectra: its shear-thinning behaviour and again, its low enthalpy of fusion. The onset of the coiling is either the formation of a solidified shell inside which material continues to flow, or gravity as the material flows up the nozzle. Microscopic evidence can be found for either of these scenarios. It is finally highlighted that these scenarios are established in two dimensions, but represent in fact a process which is inherently three-dimensional as the nozzle travels along the print direction.

The main conclusions of this thesis have been gathered in this chapter. In the next chapter, perspective for further research and improvements of the current methods will be presented.

9

Perspective for future research

The field of additive manufacturing of anisotropic materials is relatively new, and that of additively manufactured Liquid Crystal Polymers all the more so, with only one publication to this date. These materials open an exciting route in which process, material and structure influence each other more than ever. Furthermore, as illustrated in Figure 9.1, each of these aspects is reinforced with an added value: with additive manufacturing and anisotropy come supplementary design freedom, with additive manufacturing comes ease of manufacturing, and sustainabilty is not ignored as this material has a potential for recyclability. All these points create synergies with existing fields, which need to be further developed. In this chapter, limitations of the current research will be recalled, and solutions will be proposed. Then, perspectives of future research will be presented.

9.1. Limitations of the current research and possible improvements

9.1.1. Towards a quantitative study of the phenomena

The work presented in this thesis has been limited to qualitative comparisons and observations, due to limitations of the current set-up and time constraints. Even though a quantitative triggering mechanism for the swirl formation has not been addressed, evidence seems to show it may exist: Figures 5.1a to 5.1c, in which a sharp transition can be seen between absence and presence of interlayer features, suggest there may be a quantitative threshold between these two states of extrusion. A closer monitoring of the print would be necessary to study this phenomenon. Understanding more about this threshold would be useful to gain a better control of the print mesostructure, for instance if the designer wants to avoid the formation of interlayer features at any point in the print. Stopping the propagation of swirls appears only possible if two conditions

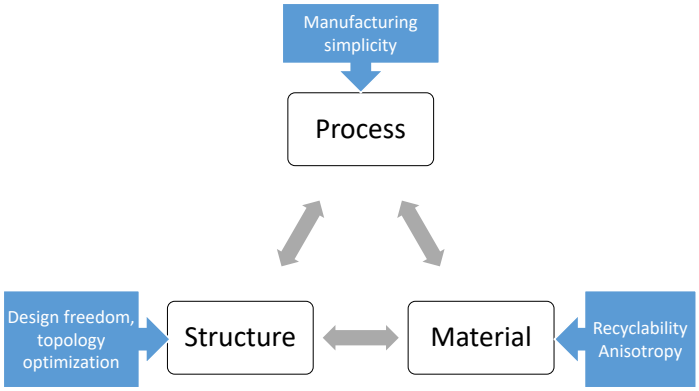

Figure 9.1 – *Additive Manufacturing of liquid crystal polymers strengthens the level of interaction between structure, process and material. While this may add complexity in modelling, for every of these aspects, liquid crystal polymers brings also an added value compared to more conventional materials like composites.*

are met: first, addition of another layer taking into account the extra-volume occupied by the interlayer feature, thus stopping their self-propagating behaviour; and second, remediation of the factor triggering them. This highlights the need for further study on this triggering mechanism.

9.1.2. Improvement of the methods employed

A study such as the one mentioned above should also aim to understand better the relationship between extrusion rate and formation of interlayer features: indeed, at this moment, extrusion rate is varied in order to increase the probability of interlayer features forming. However, unwanted side-effects may also influence the mesostructure and the mechanical properties of the part, such as the presence of voids or unevenness in the layer interfaces. It would be beneficial to adjust precisely the volume of extruded material during print depending on the filament size, in order to keep the extrusion rate truly constant in spite of variations in filament size. In the current set-up, the variation in filament cross-sectional area is up to 10%. In order to study with precision the triggering mechanism for swirl formation, this uncertainty in the true extruded volume has to be reduced. Two methods can be employed to achieve this: one method consists in improving the filament making process with a tighter control of its diameter and cylindricity. Another method consists in designing a device mounted on the printer, and able to measure the filament dimensions from two sides (as it is ellipsoidal) before it enters the extruder. The corresponding cross-sectional area should be computed, and the amount of material grinded by the roller should be updated according to this area measured, in real time.

Furthermore, this thesis has been focusing on measuring the interlaminar shear strength of samples with a short-beam shear test, which should be considered a comparative method, even though all specimens delaminated in shear. Further investigations may be undertaken with other methods of assessment of interlayer properties more suited to the rigorous field of fracture mechanics.

9.1.3. Gathering additional data

Several methods and ideas, which have not been used in this work, are believed to be interesting in the direct continuation of this study. They are presented in this section.

Parameters studied

In this work, the layer height has been kept constant at 0.15mm, a value for which a skin-core pattern is visible under optical microscopy. This allows to distinguish, most of the time, the mesostructure of the print under polarized light. However, in (Gantenbein et al. [1]), best mechanical performances were obtained with samples printed at 0.05mm layer height, as the complete thickness of the deposited bead is made of highly anisotropic skin material. It remains to be tested whether interlayer features seen in this work can also be observed and possess the same efficiency with such a small layer height.

Furthermore, the thermal environment has been assumed to be constant for all samples, as they were printed in the same enclosure in similar conditions, as reported in the Methods section, Chapter 4. However, small temperature variations may show to have an influence on the interlayer adhesion of the part or its viscosity. The question of the influence of the thermal environment on a print needs to be addressed. The influence of print speed and of the printing sequence should also be studied, as they directly influence the thermal conditions in which layers adhere together.

Imaging techniques

The use of other imaging techniques than optical microscopy has not been investigated in this work but may also provide complementary information. Confocal microscopy can for instance be useful to map the geometry of interlayer features in three-dimensions, whereas they have only be observed in their cross-section in optical microscopy. However, like optical microscopy, it is a destructive technique: layers need to be peeled off to be observed. Micro-CT scanning may show to be an interesting alternative to gain access to the entire mesostructure of the print. However, only optical microscopy under polarized light has the ability to show spiraling patterns, thanks to the birefringent properties of Vectra.

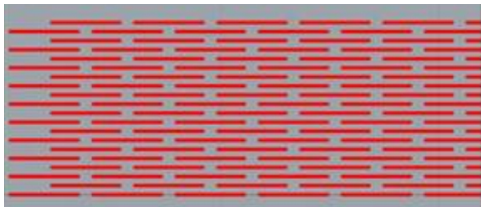

Figure 9.2 – *Infill created as a parametric file with Grasshopper in Rhino (MacNeel)*

Spiralling patterns also need to be studied further with different techniques. For instance, in the scenarios of formation established in this thesis, the spiral is created at the nozzle tip by a flow channel directed transverse to the print direction. As a result it may be expected that the direction of anisotropy may not be parallel to that of the nozzle movement in the inner side of the interlayer feature, but rather perpendicular to it. This may be verified with tests using X-ray diffraction, provided the beam could be restricted to the scale of a zone within one spire of the swirl, about $10\mu m^2$.

In-situ observations can also be improved to complement the evidence of the formation mechanism established in this work. Observations during print have been carried only with a USB microscope. Using a camera with a higher resolution at high magnifications may provide more insight. In-situ observation with thermal cameras can also be envisioned to gain insights on the influence of the thermal environment.

Strategies for improvement of interlayer properties

Several strategies have yet to be tested to change the geometry of the interlayer features, such as: partial ironing of the nozzle to flatten the top of the interlayer feature before another layer is printed; a change of the nozzle geometry; a change in the order of printing sequence to change the tip of the nozzle imprinting the interlayer feature, as shown in Figure 4.17; or rapid variations in the extrusion rate to alter the height of the interlayer feature along the printing axis. All these strategies have a common goal: to increase the level of mechanical interlocking in all directions. Indeed, this thesis has shown that interlayer features were only acting as reinforcement when they were transverse to the shear direction. It would be desirable to make them effective when exposed to all shear directions. Producing shape variations along the interlayer feature axis appears to be a straightforward way to enhance mechanical interlocking in the printing direction as well.

Samples displaying interlayer features should also be compared to annealed samples. Since annealing creates covalent bonds between layers, it is still expected to perform better than interlayer features to enhance interlayer properties. The combination of annealing and interlayer features can be tested as well. As recyclability should become an important focus in the manufacturing industry of tomorrow, other strategies to enhance interlayer properties can be tested in comparison or in combination with the interlayer features reported in this thesis.

For instance, a brick-and-mortar approach, as described in [55], may also be envisioned to enhance intralayer adhesion. In the same manner as nacre platelets acting as toughening features [56], the tortuous interface created by the brick pattern may increase the delamination surface and increase the toughness of Vectra, for which high values are already reported by [1]. This brick-and-mortar layout, complex to manufacture with composites, could be more readily implemented with 3D-printing using a custom parametric slicer such as Grasshopper to generate the infill and print sequence, as shown in Figure 9.2. Moreover, this infill type may also be investigated as a means to study the adhesion strength between beads in tensile tests by pull-out of the "fibers". Furthermore, the time elapsed between deposition of neighbouring beads is shorter when lines are short and deposited in a brick-and-mortar pattern, than if they are deposited as long lines spanning the full length of the specimen. This may enhance the adhesion strength between beads.

9.2. Other perspectives and applications

Additive manufacturing of anisotropic materials such as liquid crystal polymers enables a large design freedom: since these materials are monolithic, the freedom of movement in the layer plane is unlimited. Even overlap-

ping one curve with another is possible, as it just results in no material being extruded for the brief moment of the overlap. If the designer wishes both lines to be uninterrupted, the layer thickness may simply be dropped by half at the overlap location. This concept can for instance be directly applied to the manufacturing of planar lattice structures. Similarly, findings from the field of variable stiffness laminates and topology optimization in general, are often hindered by manufacturing constraints inherent to traditional manufacturing techniques of composites. 3D-printing of liquid crystal polymers like Vectra may thus prove useful as an enabling technology to test further levels of topology optimizations.

In this context, this thesis has shown that yet another dimension in the tailoring of structures becomes attainable: if the parameters describing the interlayer features (absence and presence but also height and shape) can be controlled, tailoring the reinforcements of a part becomes a possibility. For instance, in the field of aerospace where inspectability is an important dimension in the design of a part, specific zones can be purposedly left void of reinforcements: as a *structural fuse*, inspection may in this manner only be needed on this restricted area to know whether the part has been subjected to damage.

Finally, another research field in active development, in which Vectra could be readily applied, is 5-axis printing. Indeed, 3D-printing as currently envisioned, is in fact called by some authors a *2.5-printing* method, as the approach is always to deposit material horizontal layer after horizontal layer. This creates restrictions on the applications of additive manufacturing due to the inherently poorer interlayer bonding. 5-axis printing may unleash further the potential of anisotropic materials like liquid crystal polymers, as it may enable printing curvilinear shapes such as shells, cylinders and other components just as crucial as planar parts in the aerospace field.

IV

Appendix

A

Preliminary trials and observations

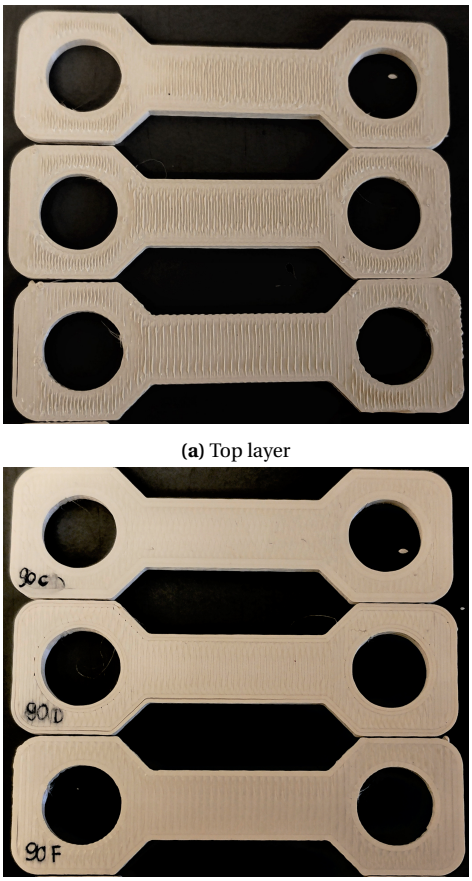

(a) Top layer

(b) Bottom layer

Figure A.1 – *Example of specimens printed. These specimens display a small apparent amount of over-extrusion in the bottom layers, worsening as layer height increases*

Initial trials with various printing parameters have been carried to establish the presence of interlayer features. Initially, the diameter of this experimental filament (1.81mm), larger than the factory-set one (1.75mm), was not taken into account and resulted in over-extrusion in printed parts. This problematic aspect was solved by adjusting the flow rate, also called extrusion rate. This setting controls the volume of material extruded and is a multiplying factor or a percentage of the theoretical volume needed. Typically, modifying this factor above or below 1 leads to over-extrusion or under-extrusion respectively. Increasing the percentage of extruded material resulted in parts which did not delaminate, and were stiff in bending. However, these parts appear rough in surface, and clearly over-extruded, as shown in Figure A.1. By lowering the extrusion rate, parts appeared significantly smoother aesthetically, but tended to show delaminations and were easier to break.

In general, several observations were made regarding the interlayer adhesion of samples:

- Even in an enclosure, samples may delaminate during print. Moreover, with an adhesive spray, the first layer adheres well to the print surface, but the second layer tends to delaminate when the material is peeled off the bed after print.
- Sawing samples, even with a diamond blade and another backing material, tends to cause delaminations, suggesting adhesion between layers should be increased.

Cross-sections of these early samples were observed under the microscope. These cross-sections showed various features, such as bead patterns, which were not regularly spaced out in some samples. The question of bead patterns will be discussed in Chapter B. But most interestingly, a sample with mild levels of over-extrusion such as 102% of the expected flow rate, also revealed regular interlayer features. This sample is shown in Figure A.2. This geometry has shown to be reproducible with other trials. The printing parameters used are available in Figure A.3. Looking closer onto the interlayer feature, one can also notice a distinguishable spiral shape, such as those described in the introduction of this work.

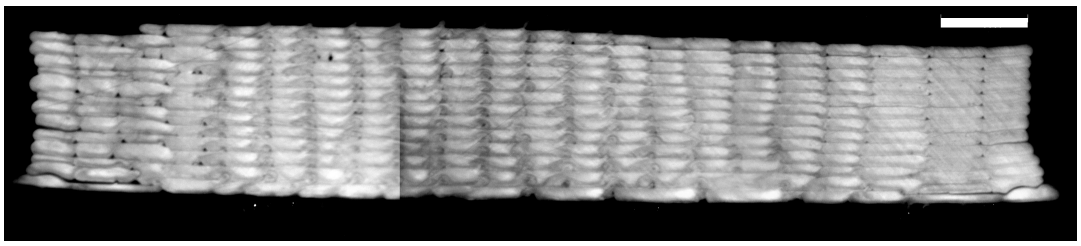

Figure A.2 – *Cross-section of an unidirectional sample under polarized light, in which the interlayer features can be observed. Scale bar indicates 1mm.*

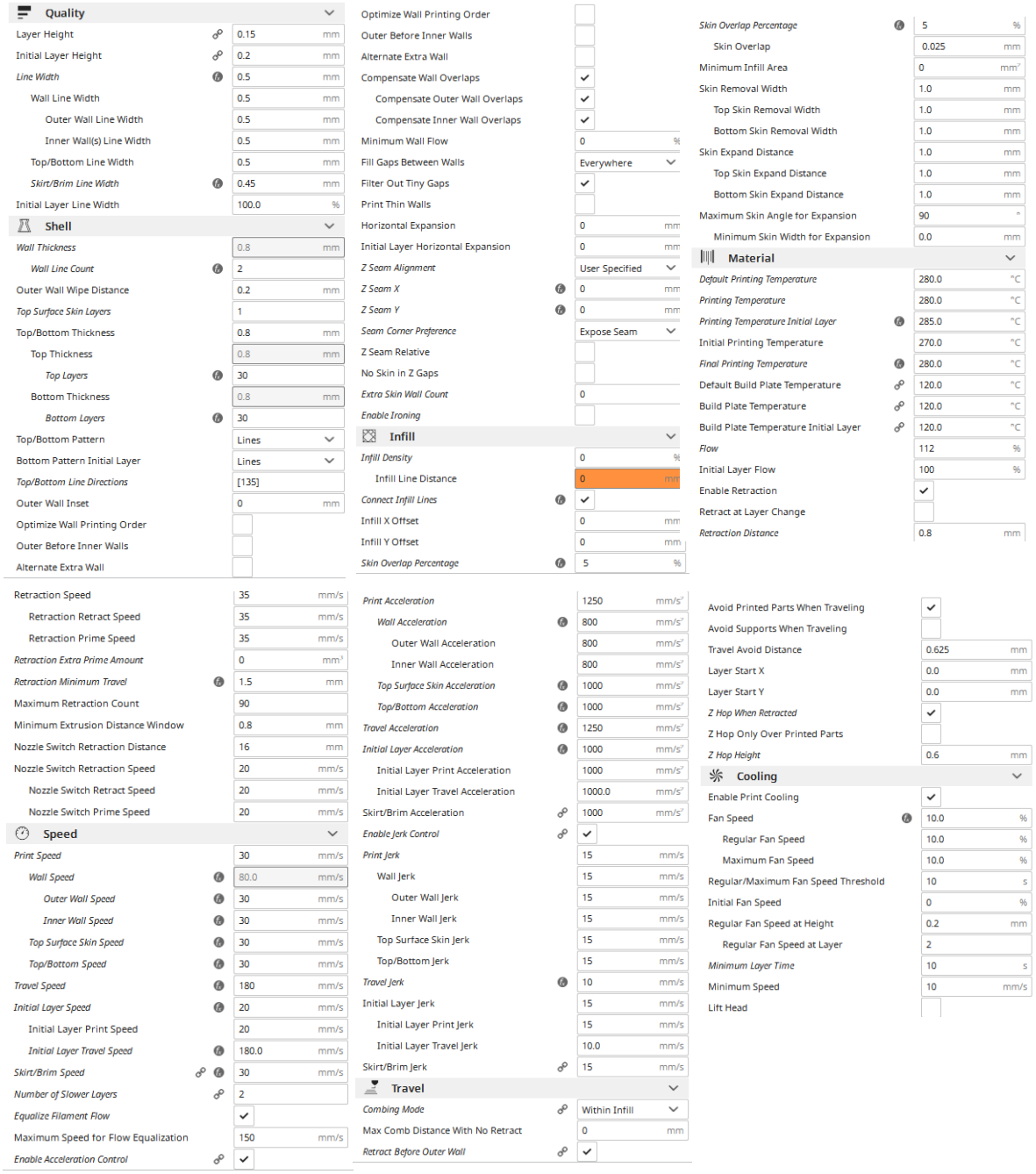

Figure A.3 – *Printing parameters set with the slicer Cura (Ultimaker) to print a specimen displaying interlayer features. The parameters used in this thesis are similar unless specified in the methodology, Chapter 4.*

B

Mesostructural characteristics

B.1. INTRODUCTION

Vectra is a birefringent material, and this characteristic is of great usefulness to characterize its mesostructural properties. It has been shown in [1] that the level of anisotropy in a filament can be correlated to two distinct areas seen with an optical microscope under polarized light: a skin and a core. In the skin, the microstructure is highly oriented in the direction of the print path, less so in the core. According to the authors of [1], their formation is linked to the solidification rate of the bead. The difference in color seen under polarized light is attributed to these different molecular orientations, with the lighter areas attributed to isotropic material, and the darker areas to anisotropic material.

It is also known from other works such as [33] that the molecular orientation of Vectra is influenced by its flowing behaviour. As a result, the observation of colors under optical microscopy with polarized light, indicating molecular orientation, may also hint on the flow history of the material before solidification. In this manner, the flow behaviour during the print may indirectly be obtained through this kind of observation. This knowledge is an useful tool to complement the understanding of the formation of interlayer features established in Chapter 6.

For these reasons, some key characteristics of the mesostructure of the 3D-printed LCP are presented and discussed in this chapter:

- Differences in colors that can be seen under polarized light, and referred to as the 'skin-core' pattern, described in [1]. These will be presented in Section B.2.
- Boundaries between beads, or in other words, the frontiers between material from one bead and material from another bead, first with respect to color patterns in Section B.3, and second, with respect to void patterns in Section B.4.

For the sake of clarity, for each of these points, a separate result section will directly be followed by a discussion and a conclusion. The methodology is the same as that of Chapter 4.

B.2. SKIN-CORE PATTERN

It has been suggested in [1] that a pattern as seen in Figure B.1a results from even solidification starting from the free surface of the bead: fast solidification occurs on the top and on the sides because of exposure to the colder environment. In the core, more time is elapsed till the temperature can drop under the solidification threshold, which leaves more time for molecular orientation. Therefore, the skin is solidified into an anisotropic state while the core is solidified into a more isotropic state, and the difference in color on the micrograph is due to the different optical properties that these two molecular states confer to the same material. Observations linked to this skin-core pattern will be gathered in this section.

Skin-core pattern within one bead

In some samples, the presence of a clear delimitation between skin and core in a concentric manner within one beads renders the identification of bead boundaries straightforward, even without the presence of voids. This concentric pattern, highlighted by [1], can indeed be seen on some specimens, as shown in Figure B.1. This pattern however, is not constant throughout the specimen and appears to fade away when beads are located far away from the extremities (Figure B.1c).

Two-beads pattern

On Figure B.1c, one can see that the two colors which were so far observed within one bead, can in fact be seen more consistently in a pattern of two beads, illustrated in Figure B.2. In this figure, the printing directions are different, but the pattern remains the same: one bead displays a light color in its center, its

(a) F80 0.5 090 4

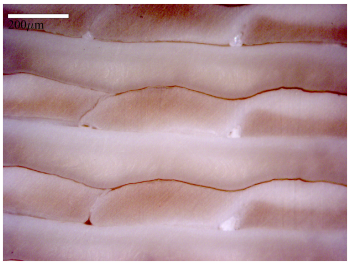

(b) F85 0.5 090 2

Figure B.2 – *Micrographs of samples, longitudinal cross-sections*

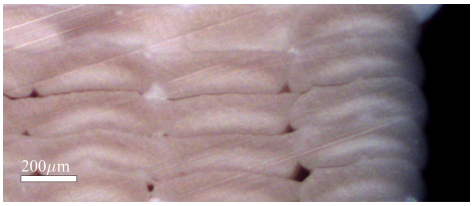

(a)

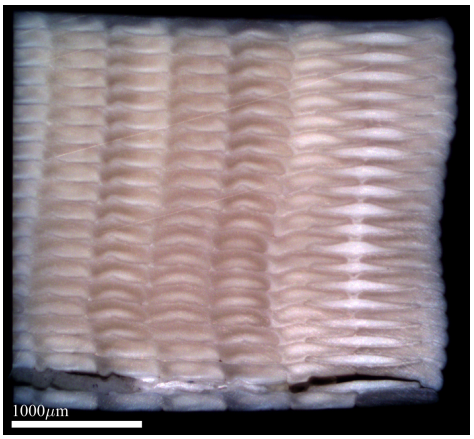

(b)

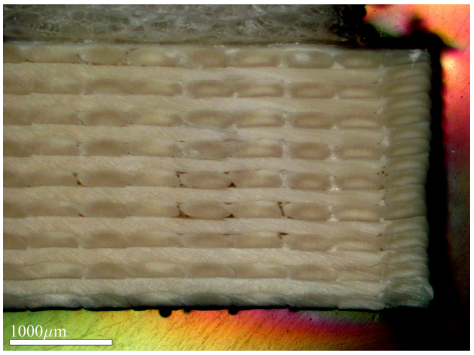

(c)

Figure B.1 – *Micrographs of cross-sections of samples under polarized light. Top: Detail of Sample F85 0.5 0 1 (Transverse). Middle: Sample F85 0.5 0 4 (Transverse). Bottom: Sample F85 0.5 090 6 (Longitudinal).*

neighbour displays a dark color in its center. Other examples can also be found at bigger scales in Figures 5.7c and 5.7d or Figure B.6b. The reader is also invited to consult the online appendix [14] for direct observation of other samples.

The thermal history and solidification rate experienced by two neighbouring beads should not differ largely, especially since the images are taken in the middle of a cross-section, where any border effects should not play an influence. This may lead one to think that another parameter plays an influence in the color pattern of a bead under polarized light. Since it seems to the author that the only thing that varies consistently between two neighbouring beads is the direction with which they are printed, an hypothesis can be formulated: *The color pattern of a bead is influenced partly by the solidification rate, and partly by the direction of observation with respect to that of the printing deposition.*

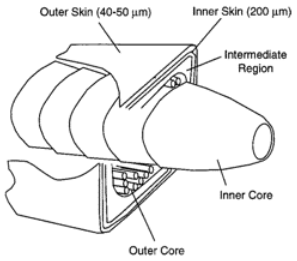

Figure B.3 – *Schematics of the mesostructure of injection-moulded Vectra A950. Extracted from [26].*

In other words, the color of the print under polarized light, which, as was pointed out by [1], depends on the level of molecular orientation within a bead, may also depend on the printing direction, out-of-plane with respect to the micrograph cross-section plane (⊗ or ⊙). This is not a new idea. Indeed, Plummer et al. [26] have developed a structural model for injection-moulded Vectra A950, summarized in Figure B.3, in which directionality of the flow is established. In [24], this directionality is also noticed with scanning electron microscope. One may envision that the flow front within the material, and thus the molecular orientation, could be arranged in such a conical shape also as it is deposited by the nozzle in the print direction, leading to the two different colors seen under microscopy. Further investigation is needed, using methods similar to those used in [26] and [24], to test this hypothesis.

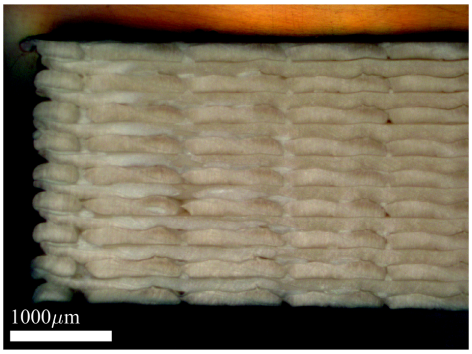

Figure B.4 – *F85 0.5 090 6, left extremity, longitudinal cross-section*

Conclusion on color patterns

A first conclusion of importance is that the color pattern which had been identified by previous literature is in fact one of many. While it has been suggested in previous literature that solidification rate was influencing the color distribution, the fact that color changes can be seen between two neighbouring beads of the same print, for which the solidification rate is similar, indicates that another factor also plays a role in the color of one bead. A possible explanation may be the print direction, which may orient the flow front in a conical manner.

B.3. Relationship between color pattern and bead boundary

It has been seen in the previous section how a color pattern may be observed within one bead, but also in a repeating unit of two beads. This shows that the link between color pattern under polarized light and printing parameters is not merely tied to solidification rates. In this section will be addressed in more details the relationship between color patterns and bead boundaries.

A close look into the boundaries between beads is needed for the understanding of interlayer feature formation, as it is closely tied to the material distribution based on the location of preceding beads. However, the distinction between boundaries is only straightforward in two cases: if the beads display a concentric skin-core pattern, or if the beads are clearly delimited by voids. In other cases, especially when interlayer features can be seen, the distinction from one bead to another is more difficult to the observer, partly because of the lack of voids, and partly also because of the lack of color contrast between them.

Variability of the color pattern

While the two-bead pattern is largely present among samples, as can be seen in the Supplementary Data [14], it is not systematic. Within one sample type, discrepancies can be seen. Figure B.6 shows for instance two samples extracted from the same configuration - and thus having the exact same g-code, for which the color pattern differ. One sample in Figure B.6b has a distinctive difference between colors, while it can hardly be noticed in Figure B.6a.

In fact, even within one sample, the color pattern of beads may change. An example is the observation of Sample F85 0.5 090 6, whose complete longitudinal cross-section is in Figure B.6b. In a close-up, in Figure B.4, the two bead pattern can still be noticed thanks to the presence of voids every two beads, but the color itself hardly changes, and no distinct boundary can be observed within one pattern, as if the two beads had completely fused. On its right-hand side (zoomed in Figure B.1c), this pattern is fully distinguishable. In the same configuration, but another sample (F85 0.5 090 6 in Figure B.6a), the color pattern can hardly be seen at all throughout the longitudinal cross-section, in spite of having been printed with the same g-code file.

The disrepancy in bead patterns within one sample can also be noticed in Figure B.5b, in which a sharp transition exists: a concentric bead pattern can be seen on the bottom half, with large voids separating neighbouring beads; and on the top half, the presence of interlayer features is noticed, combined with a less distinctive color pattern.

In the latter case, the bead pattern transition seems linked to the presence of interlayer features. As can be seen in Figure B.5, samples in which interlayer features are displayed find the color pattern of their beads disturbed. This can result in either the kind of bead pattern illustrated in Figure B.5b, which appears regular although the boundary cannot be clearly identified; or another type of pattern, far more random, illustrated in Figure B.5a, in which bead boundaries also can hardly be identified.

In Figure B.5b, one could be tempted to associate the regular striped pattern on the top half with bead boundaries. However, the bottom half beads whose boundaries are easily distinguishable indisputably indicate where the nozzle has passed to deposit material. Boundaries between the top half and the bottom half should be aligned since the nozzle path only repeats itself from one layer to the other

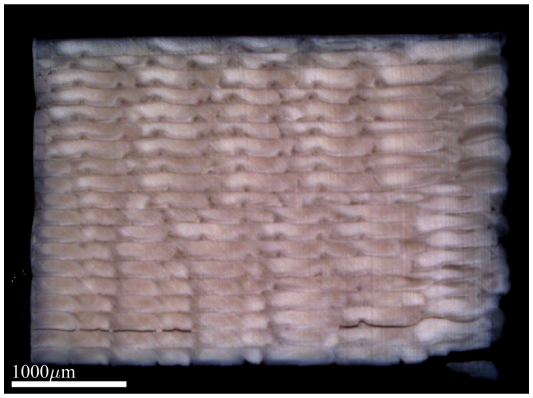

(a) F102 0.35 0 3, transverse cross-section

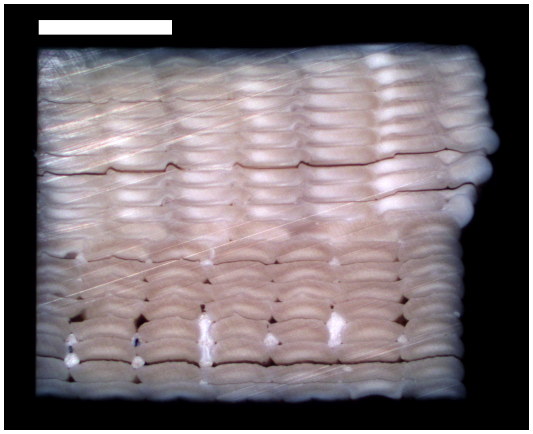

(b) F85 0.5 0 1, transverse cross-section

Figure B.5 – *Micrograph of samples with irregular bead pattern*

according to the g-code file. This indicates that in the presence of interlayer features, color patterns cannot be used to establish the localization of theoretical bead boundaries.

These three facts suggest the following elements:

- The hypothesis established in the previous section, stating that the print direction may influence the color pattern of a bead in polarized light, does not hold true for every sample, as this two-bead pattern can sometimes disappear or simply be absent. It appears that other factors, most likely environmental since they can appear within one sample or within two samples printed with the same parameters, may reduce the visibility of this pattern.
- A consequence of these observations is that in this stage of the research, the color pattern cannot be used reliably to distinguish between beads. It may be only be used as a supporting hint when the two patterns mentioned previously can be clearly identified: a concentric skin-core pattern, or a two-bead pattern.

This conclusion highlights a lack of knowledge and some contradictions. The second point above does provide a constraint, which has been applied in this thesis, in order to prevent this knowledge gap from interfering with further conclusions. Nevertheless, it appears essential to the author that more research be carried on the relationship between the colors of thermotropic liquid crystal polymers observed under polarized light, the flow behaviour related to their formation, and the corresponding level of anisotropy. Such knowledge may provide very useful insight on the 3D printing process without having to refer to numerical approach. It may even be useful to calibrate or validate numerical models of the 3D printing process, for which a major challenge is that both thermal and rheological characteristics of the materials play a simultaneous and crucial role, and evolve with time.

B.4. Relationship between void pattern and bead boundary

In light of the above conclusions, it could appear that the only reliable manner with which boundaries can be distinguished is the presence of voids. However, this should also be done with care. Indeed, for a certain type of bead pattern as illustrated in Figure B.7, one out of two void does not indicate a bead boundary but is instead thought to be a resulting effect of the flow behaviour of the bead. On this figure, two consecutive voids can be seen in what appears to be the same bead judging from the short distance separating them. The color distribution seems to indicate that the left bead may have partially collapsed when the next bead was deposited.

This feature, as mentioned above, can also be seen in samples with a larger extrusion rate, in which supposedly no voids should be seen, such as in Figure B.8. Moreover, they appear in Sample F102 0.35 90 5 6 on top of a 0° layer, which is a flat and level surface, so the void cannot be linked to an uneven surface beneath it.

Another micrograph is shown in Figure B.9, in which the polarized light did not allow to see contrasted colors between two beads. Instead, it appears to show boundaries between beads, as these dimensions correspond with the line width set in the g-code. A clear line can be distinguished between the two beads, again in a pattern of two. The two consecutive voids can also be distinguished. In this figure, it appears more clearly how the first bead may have collapsed when the second one was deposited on top, almost covering half of it.

A possible explanation for such a pattern may be a solidification of the bead in two steps: the first

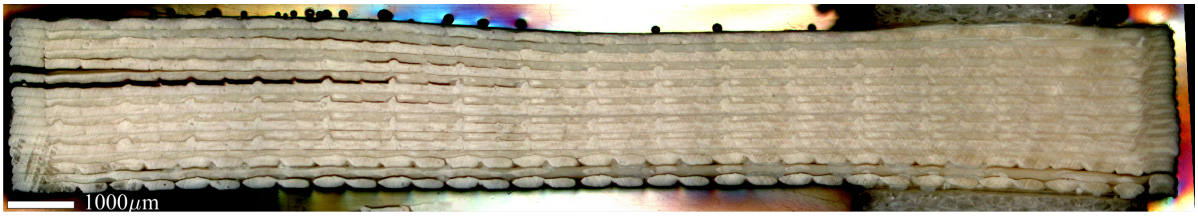

(a) F85 0.5 090 4

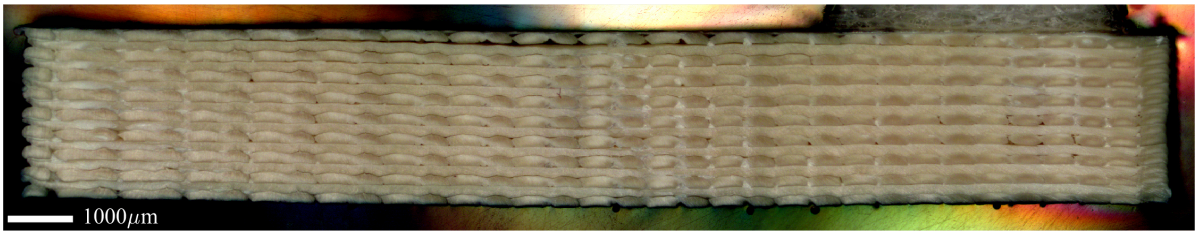

(b) F85 0.5 090 6

Figure B.6 – *Micrographs of samples (Longitudinal cross-section)*

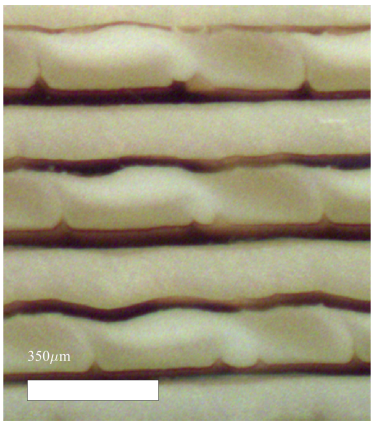

(a) F85 0.35 90 5, longitudinal cross-section

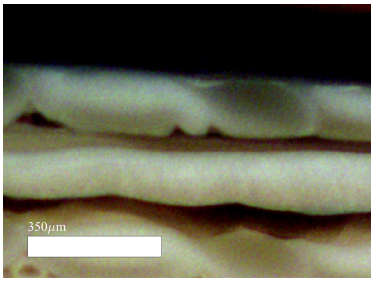

(b) F80 0.35 90 5, longitudinal cross-section

Figure B.7 – *Micrograph of Samples displaying a collapsed-bead pattern. Print sequence from left to right.*

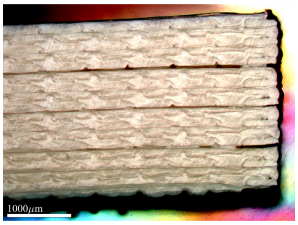

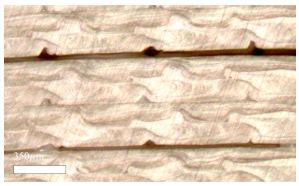

Figure B.8 – *Micrograph of Sample F102 0.35 90 5 6 with voids every 0.7mm, i.e. twice the line width*

layer deposited solidified directly upon contact with the surface underneath, starting from its bottom, creating a bathtub shape corresponding to the shape of the bead when it first touched the surface, with little pressure. This is coherent with the fact that the bottom of this first bead is darker than its top. In a second stage, as was indicated by the location of the collapsed bead, more material may have been deposited than what the first bathtub-shaped solidified material could hold, and therefore it may have overflowed slightly, creating this collapsed shape. Since the temperature of the direct environment may have already been raised by the presence of molten material, the solidification rate may be slower in this second stage, explaining why the collapsed region is lighter in color on the micrograph. The next bead would then take the shape that is offered and overlap the first bead. What this explanation does not cover, is the difference between the two consecutive beads, which *de facto* exists, since it can be consistently observed that when one bead collapses, the other

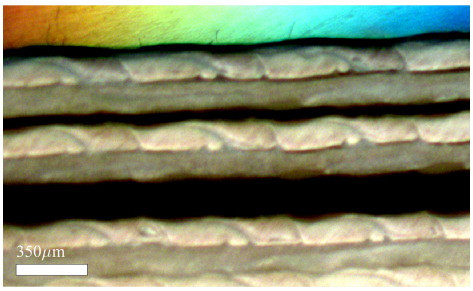

Figure B.9 – *F80 0.35 90 1, detail on the longitudinal cross-section seen under polarized light with a ×2.5 objective.*

stays in an oval shape.

Conclusion

Regardless of the formation mechanism of this pattern which is at this stage an hypothesis for future work, in light of these results, several points can be made:

- This pattern is also generated by a repeating unit of two beads instead of one, and furthermore, the same two-color pattern can also be observed in it.
- Once more, even though the true flow behaviour cannot be traced back for validation, the distribution of colors may provide hints on the thermal and flow history which resulted in beads with such a pattern.
- Most importantly, in a similar manner as in the previous section, the present observations highlight a lack of knowledge on the formation mechanism of a bead. In order to prevent this lack of knowledge from interfering with further conclusions, it has been considered throughout this work that the only way to determine where bead boundaries are located is when a clear delimitation can be seen between them, such as voids in both sides, at least over one portion of the specimen, such as the bottom. Figure B.6a shows an example of an indisputable way of locating beads: on the two bottom 90°layers, the perimeter of each bead can be clearly distinguished. Even though the upper layers do not display these voids, this allows a good localization of the places where the nozzle has deposited the beads, and consequently, a localization of its movements throughout the print.

C

Appendix: Supplementary Data

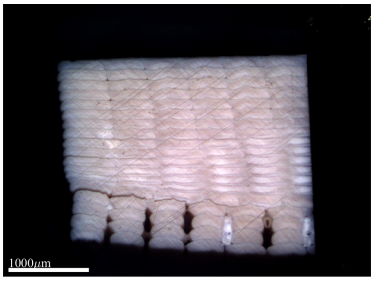

(a) F80 0 0.5 7: τ_{SBS} = 6.48 MPa

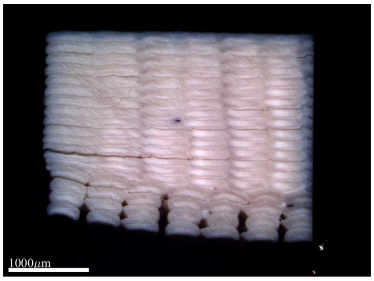

(b) F85 0 0.5 6 : τ_{SBS} = 5.06 MPa

Figure C.2 – *Comparison of the mesostruscture of two samples with 5% extrusion rate flow difference: mesostructure and performances.*

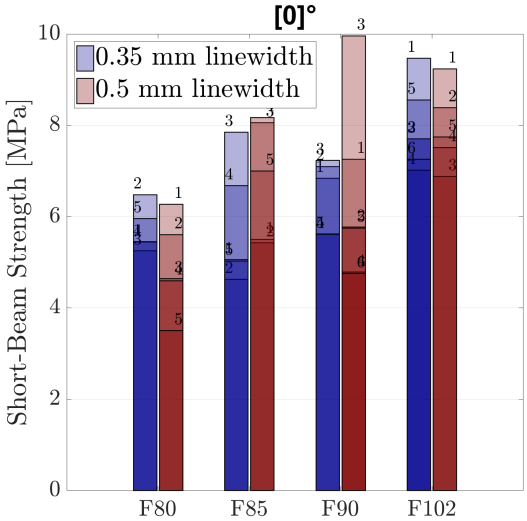

Figure C.1 – *Short beam strength of unidirectional samples, with identification number of sample indicated.*

C.1. Microscopy observation of samples

In this section, a detailed description of each sample configuration is gathered. All the mentioned sample cross-sections are available for download in the Supplementary Data [14]. This description of samples is aimed at comparing the cross-section of samples individually based on their performance in short beam shear strength. As a result, this description is thought to be read while comparing these micrographs with Figures C.1 and C.4.

C.1.1. Unidirectional Configuration

F80

Small, barely noticeable notches are present on all samples.

Samples display voids on their bottom layers. The core in all cases has a lighter color and is more compacted, as shown in Figure While it has been said that over extrusion is a propagating phenomenon, one can notice that voids appear on the top layer after some sort of higher compaction has been reached in the mid-section. A majority of samples might have moved during the print as shown in Figure C.2. On the transverse cross-section, one can see the boundary between the lighter and darker areas is tilted, with seemingly one layer difference between one side and the other.

F85

Small, barely noticeable notches are present on all samples.

Samples F85 0.35 0 [1, 2, 5] display no difference both in SBS and in cross-sections with the F80 0.35 specimens.

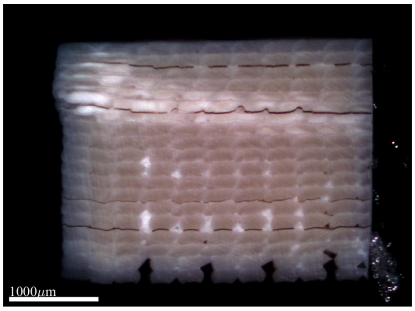

(a) F85 0 0.35 3

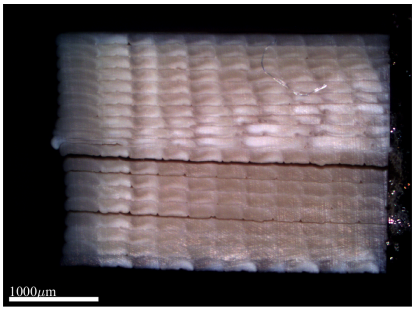

(b) F85 0 0.35 4

Figure C.3 – *Transverse microscospy of two unidirectional samples with a 85% extrusion rate.*

Other samples from this series, F85 0.35 0 [3, 4], have a less contrasted transverse cross-section, which, on the micrograph under polarized light, appears darker. They are shown in Figure C.3. These samples are the strongest among their peers. In particular, F85 0.35 0 3 reaches values which set it in the average short beam strength of the F102 samples.

Standard deviation are similar between the 0.5mm and 0.35mm linewidth series. While Samples F85 0.5 0 [3, 4, 5] display a regular, traditional skin/core pattern with short notches, Samples F85 0.5 0 [1, 2] only display this pattern on their lower half, with the top half being more densely packed. Figure C.1 shows that short-beam strength results are lowest for Samples F85 0.5 0 [1, 2], and highest for F85 0.5 0 [3, 4, 5]. Thus, in this case, it appears that the samples with a regular pattern and a clear distinction between beads perform better than those having a denser mid-section and voids on the top and bottom layers.

F90
Fully formed swirls are present in varying amounts in most samples.

All specimens in the 0.35 series but Sample 1 display fully-formed swirls. These features can be seen in both a regular pattern (Samples F90 0.35 [2,4]) and irregular (Samples F90 0.35 [3,5]), but this observation cannot be tied to a trend in their short-beam strength.

Scatter is much higher in the 0.5mm-linewidth series than in the 0.35mm-linewidth series due to Sample F90 0.5 [3] outperforming its peers by 75% percent. In the 0.5mm-series, Sample F90 0.5 [1] differs in cross-section to its peers and is instead very similar to Samples F85 0.5 [3, 4, 5]. It also finds itself in the same performance range in the mechanical testing. No void can be reported, and small notches can be seen.

Sample F90 0.5 [3] outperforms not only its peers but also all F102 samples. However, no specific difference in cross-section can be noticed with its peers. All samples of this series but Sample 1, display both a traditional skin core pattern on the bottom, and fully-formed swirls on their upper part, including Sample 3. No delamination can be seen on both its transverse and longitudinal cross-sections, which can still mean that the sample delaminated from a side that has not been observed.

All the other samples display interlayer features in varying amounts. Out of the 5 delaminations that can be observed in total, 3 have occurred in the upper zone with swirls and 2 in the lower zone with clear bead separation. Their performance is close to those of the lowest performing F85 samples, in spite of displaying taller inter-layer features such as fully-formed swirls instead of notches.

F102
Fully formed swirls are present in all samples.

The F102 specimens all display a very marked swirl pattern. Standard deviations and average results are almost equal for the two linewidth type. The lack of regularity in swirls of some samples does not correlate with a decrease in performance. The longitudinal cross-sections indicate that in all cases, the delaminations have not opened the specimens.

C.1.2. [0/90] Configuration

F80
Small, barely noticeable notches are present in restricted areas.

The scatter in both series is rather low. All the 0.35mm-linewidth samples delaminate on top of their 90° layers, although very few delaminations can also be seen on the 0° layers. In most cases no notch can be seen, but the distinction can still be made in terms of layer profile between the two types of layers because the 90° layers still present a rougher, more uneven profile than the 0° layers. This distinction can be seen in Sample F80 0.35 090 2 for instance, illustrated with a close-up in Figure C.5. This zone of the sample highlights the type of features that can be seen for this type of samples.

Sample F80 0.5 090 7 is outperforming its peers, with close to a 1.5 MPa short beam strengh difference

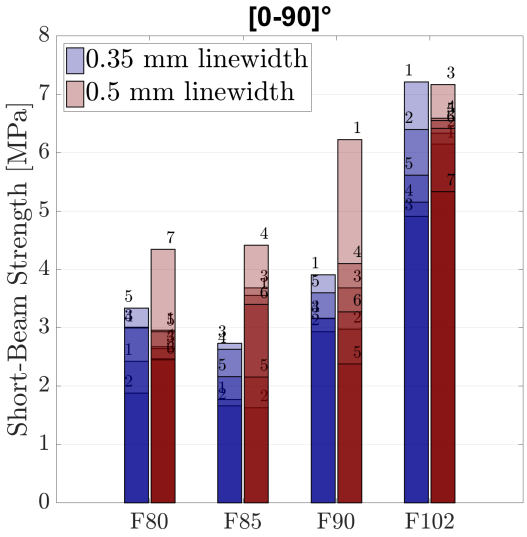

Figure C.4 – *Short beam strength of [0/90] samples, with identification number of each sample indicated.*

Figure C.5 – *Close-up of Sample F80 0.35 090 2 showing an uneven layer profile but no interlayer feature.*

with the next best-performing material. Figure C.6 shows its longitudinal cross-section. Interestingly, this sample displays three types of delaminations: they have occurred on top of the 90° layer on the left-hand side, while they have occurred on top of the 0° layer on the right-hand side. In the left side, where each layer is started by the print head, the interlayer features are short to non-existent: the classification type is A-90. However, since notches are a propagating phenomenon, the become gradually taller in the direction of the printing sequence. On the left side towards the middle, they can be seen tall, and most notably, plastically deformed, in a B2-90 manner.

F85

Only a handful of interlayer features can be found in the 0.35-mm linewidth series, but they are present in the 0.5-mm linewidth series in restricted to large areas.

In the 0.35mm-linewidth series, the performance of samples was lower in average than that of the F80 series. However, no specific distinction can be made between the two configurations by looking at their cross-section. Therefore, this larger average SBS may also be attributed to F80 0.5 090 7 whose mesostructure was discussed in the previous paragraph. In a similar manner as the F80 samples, these samples delaminate mostly on top of their 90° layer. Unevenness of this layer profile is high but regular, as shown in a close-up of Sample 4 found in Fig. All samples but Sample F85 0.35 090 5 delaminate on top of their 90° layer. In the latter, delaminations are on top of the 0° layer interface, which in this case, can be considered are rougher than the 90° one due to the numerous voids, apparently caused by under-extrusion.

The scatter is larger in the 0.5mm-linewidth series, with the highest-performing sample, F85 0.5 090 4, having a short beam strength more than twice as high as that of the lowest performing sample, F85 0.5 090 2. However, this difference may be explained by the mesostructured of each sample: Sample F85 0.5 090 2 is very porous through the whole thickness, and as a result no notch has been built up, which can explain the low performance. Samples F85 0.5 090 [1,3] are similar in cross-section, with notches reaching about 60% of the layer height at their tallest, and in a similar fashion as F80 0.5 090 7, display different kinds of delaminations which are reported in Table C.2. However, unlike the latter, they display delaminations both on their 0 and 90° layers in the same areas.

F90

Presence of interlayer features is variable in this series: While Samples F90 0.35 090 [1,2] display very small notches in restricted area, Samples F90 0.35 090 [3,4] do not display any interlayer feature, apart from a higher roughness. Samples F90 0.5 090 all display tall notches, except F90 0.5 090 5 which only shows an uneven layer profile.

The F90 0.35 090 series shows well the variability of delamination behaviours that can be seen within one configuration. All samples delaminate on top of the 90° layer, while Sample F90 0.35 090 5 is the only one which delaminates on top of the smoother profile of the 0° layer. Looking at performance, however, this sample did not gain or lose from this difference as it lies in the same performance range as its peers. In fact, one can notice that in spite of these different behaviours, the scatter in this series is the smallest of all experiments. One common point for all samples in this series is that all samples in this configuration delaminated in the right-hand side of the micrograph while the printing direction goes from left to right. This means that in cases where interlayer features can be seen, assuming the delamination propagated inwards, it first met its smoothest angle.

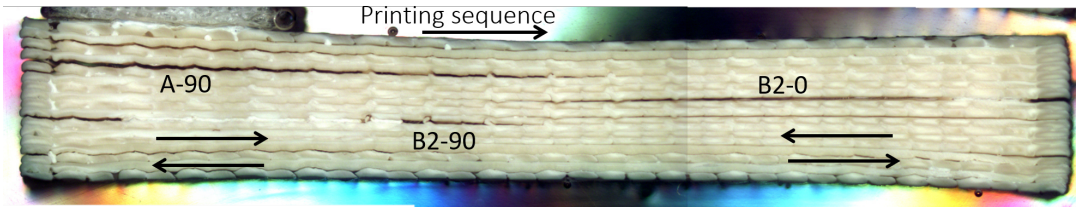

Figure C.6 – *F80 0.5 090 7*

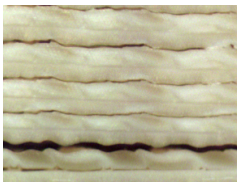

Figure C.7 – *F85 0.35 090 4*

In contrast to the 0.35-mm series, the F90 0.5 090 series shows the largest scatter of all sample configurations tested. The highest performing sample, Sample F90 0.5 090 1, has a Short-beam strength which is again double that of the lowest-performing sample, Sample F90 0.5 090 5. This case was addressed in Figure 7.7. Such scatter is expected with the F90 series, as it has been noticed in previous trials that this was a series where interlayer features could develop without too much over-extrusion – or not develop at all.

On these samples, except for Sample 5, all specimens were printed from right to left, and delaminated on the left hand side, which is the location were swirls typically have their smoothest angle outwards due to the shape that the nozzle imprints. In Sample 2 however, the sharpest angle appears to be the outermost on the left-side, which is why it was placed in the B2-90 category. However, the sharp angle seem to be linked to plasticity as it does not match perfectly with its imprint on the upper layer in the delamination. This sample did not gain from this supposed deformation as it performs on par with its peers.

The chosen path of delamination, although being consistently restricted on the left-hand side, does not consistently start on the 0° or 90° layer. On the samples which have been categorized in B1, no damage to the notches can be seen, suggesting that they did not act as crack-arrest features.

The high performance of Sample F90 0.5 090 1 remains unexplained. The main noticeable difference between Sample 1 and its peers, is the crack-length. In Sample 1, one can notice two types of cracks: those starting from the side, on 0° layers, did not propagate. Multiple delamination sites can also be seen on top of 90° layers in the center, but again they did not propagate. The reason for this discrepancy is not understood, as this sample was printed in the same manner as its peers. Since this sample does not specifically display any taller notch than its peers, the mechanical interlocking is not greater, therefore the answer may lie in chemical adhesion, for instance caused by an unidentified change in environmental conditions.

F102

Tall interlayer features can be seen in both series, although their shape varies significantly more in the 0.35mm-series, which has a larger scatter in performance than the 0.5-mm series. For instance, the weakest sample is Sample 3, which in comparison with its peers, does not display any swirl but two types of stepped notches reaching less than a third of the layer height. Swirls can be seen on samples F102 0.35 090 [1,2], and all samples from F102 0.5 090.

Another aspect differentiating them is the fact that Samples F102 0.35 090 [1,2] which possess the strongest short beam shear strength, both delaminated on top of their 90° layers, while Samples F102 0.35 090 [3,4] delaminated on top of their 0° layers. While for the former, the crack lengths are merely 1mm, for the latter, they extend from 25% to 50% of the total length of the specimen. This suggests that a delamination in a 0° layer propagates more easily – as all tests were carried at the same speed and stopped at 1mm-cross head movement. Samples from the 0.5mm-linewidth series can all be compared, in performance and mesostructure, to Samples 1 and 2 of the 0.35-mm configuration.

C.2. SHORT BEAM STRENGTH TESTS

In this section, additional information on the mechanical tests will be presented.

C.2.1. Comparison of loads

As stated in Section 5.4, the load selected to derive the short beam strength corresponds to the maximum of all peaks. The relevance of this choice can be discussed, as three possibilities may be elected.

The most straightforward choice, and most compliant with the ASTM D2344 standard is the

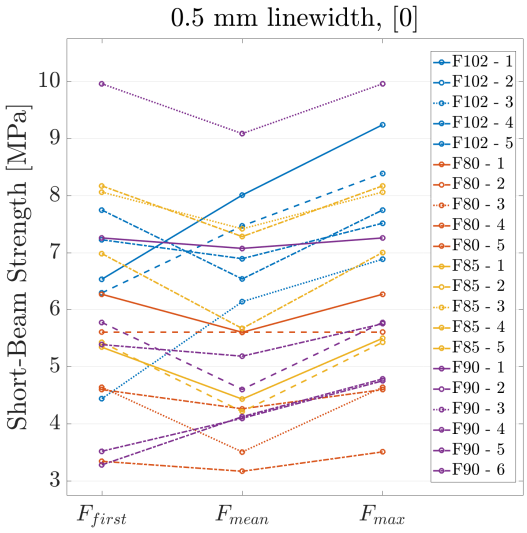

(a)

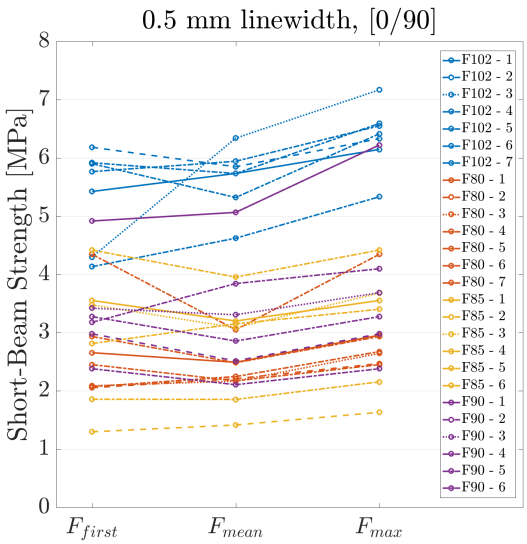

(b)

Figure C.8 – *Comparison of short beam shear strength values calculated in three different cases: by taking the first peak in the curve, the mean of all peaks, or the maximum peak.*

first peak. However, the first peak load might not be the one in which interlayer features have an effect, as the specimen would first fail in its weaker areas. The difference between the maximum peak and the first peak can be 3 MPa. These peaks are most-likely associated to two distinct delaminations, however it is the configuration producing the highest short beam strength which is of interest in this work. Using the first peak would leave the possibility that some samples are assessed not by the presence of interlayer feature but by that of a small defect.

Another possibility would be to use the mean of all peaks. While this may reduce scatter and tone down the effect of initial defects, it does not represent a physical measure of the specimen and is more sensitive to the peak finding algorithm, with a sensitivity to 'noise' defined arbitrarily.

In order to measure the impact of this choice on the results, a comparison is carried between the short-beam strengths derived from the load at the first peak, at the maximum peak, or at the mean of all peaks. As shown in Figure C.8 on the 0.5 0 samples, it can be seen that the classification varies from sample to sample within one series: if one were to compare all F102 0.5 0 samples, one would see for instance that the best-performing sample would be Sample 5 if the first peak were selected. If the maximum peak were selected, the best performing sample would be in fact Sample 1, while Sample 5 is relegated to the third row. This inconsistency is linked to the different behaviours of the samples, with two distinct cases: either the first peak is the maximum peak, or the first peak is lower than the maximum peak, often by more than 1 MPa. This changes the relative performance within one series. However, in light of the previous element, the author still believes that a performance classification using the maximum peak load is the best one to get the fullest understanding of the characteristics of each specimen.

Furthermore, the relative classifications within one sample type (i.e. F102 0.5 090) appear much less affected in the [0/90] configuration (right) than in the [0] configuration (left). This may be seen as another element in keeping with the conclusions reached in the previous paragraph: no effect of strengthening can be seen in the [0] configuration, regardless of whether the first peak, the mean peak or the maximum peak is used to derive the short-beam strength. However, a strengthening effect can be noticed in all cases in the [0/90] configuration: the F102 specimens, in blue, perform above the other specimens whether one takes the first peak, the mean of all peaks or the maximum peak.

			Thickness			Width			Mass		
			Mean (mm)	SD (mm)	CV (%)	Mean (mm)	SD (mm)	CV (%)	Mean (g)	SD (g)	CV (%)
F80	0.35	0	2,5	0,101	4,1	5,7	0,112	2,0	0,319	0,007	2,1
F85	0.35	0	2,7	0,086	3,2	5,7	0,094	1,6	0,346	0,014	4,1
F90	0.35	0	2,8	0,035	1,3	5,8	0,182	3,2	0,371	0,012	3,2
F102	0.35	0	2,9	0,083	2,8	5,9	0,060	1,0	0,412	0,014	3,5
F80	0.5	0	2,6	0,072	2,8	5,6	0,049	0,9	0,316	0,009	2,8
F85	0.5	0	2,8	0,104	3,7	5,6	0,038	0,7	0,364	0,017	4,6
F90	0.5	0	2,8	0,062	2,2	5,6	0,081	1,4	0,360	0,012	3,4
F102	0.5	0	3,0	0,033	1,1	5,8	0,058	1,0	0,406	0,011	2,8
F80	0.35	0/90	2,4	0,087	3,7	5,7	0,038	0,7	0,298	0,015	5,1
F85	0.35	0/90	2,6	0,086	3,3	5,7	0,049	0,9	0,338	0,009	2,7
F90	0.35	0/90	2,7	0,050	1,9	5,7	0,038	0,7	0,354	0,008	2,4
F102	0.35	0/90	2,7	0,053	2,0	5,9	0,018	0,3	0,380	0,008	2,2
F80	0.5	0/90	2,4	0,096	3,9	5,5	0,035	0,6	0,295	0,009	2,9
F85	0.5	0/90	2,4	0,065	2,7	5,5	0,052	0,9	0,299	0,004	1,4
F90	0.5	0/90	2,5	0,082	3,2	5,5	0,049	0,9	0,335	0,018	5,3
F102	0.5	0/90	2,7	0,078	2,9	5,8	0,048	0,8	0,368	0,011	2,9

Table C.1 – *Mean thickness, width and mass of the short beam test samples gathered by series. SD: Standard Deviation, CV: Coefficient of Variation (SD:Mean ratio in percentage)*

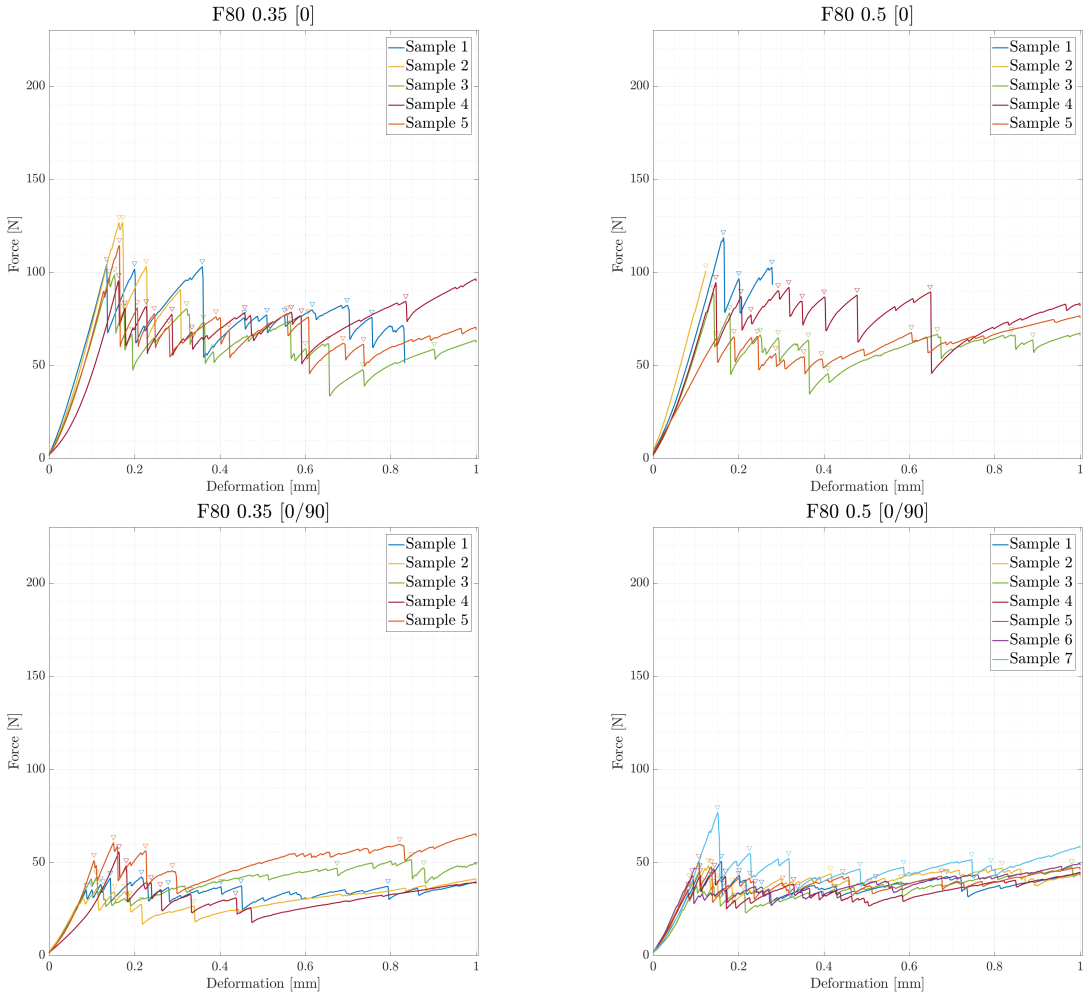

Figure C.9 – *Raw load-crosshead displacement curve for the F80 samples*

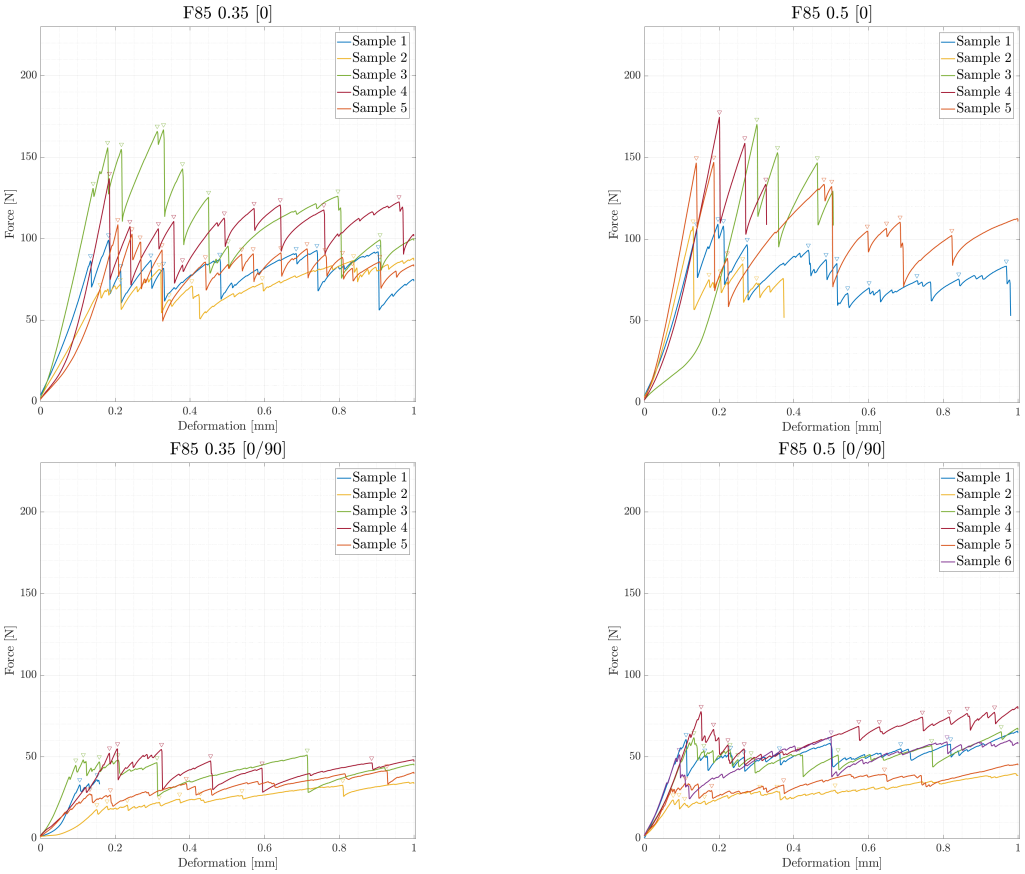

Figure C.10 – *Raw load-crosshead displacement curve for the F85 samples*

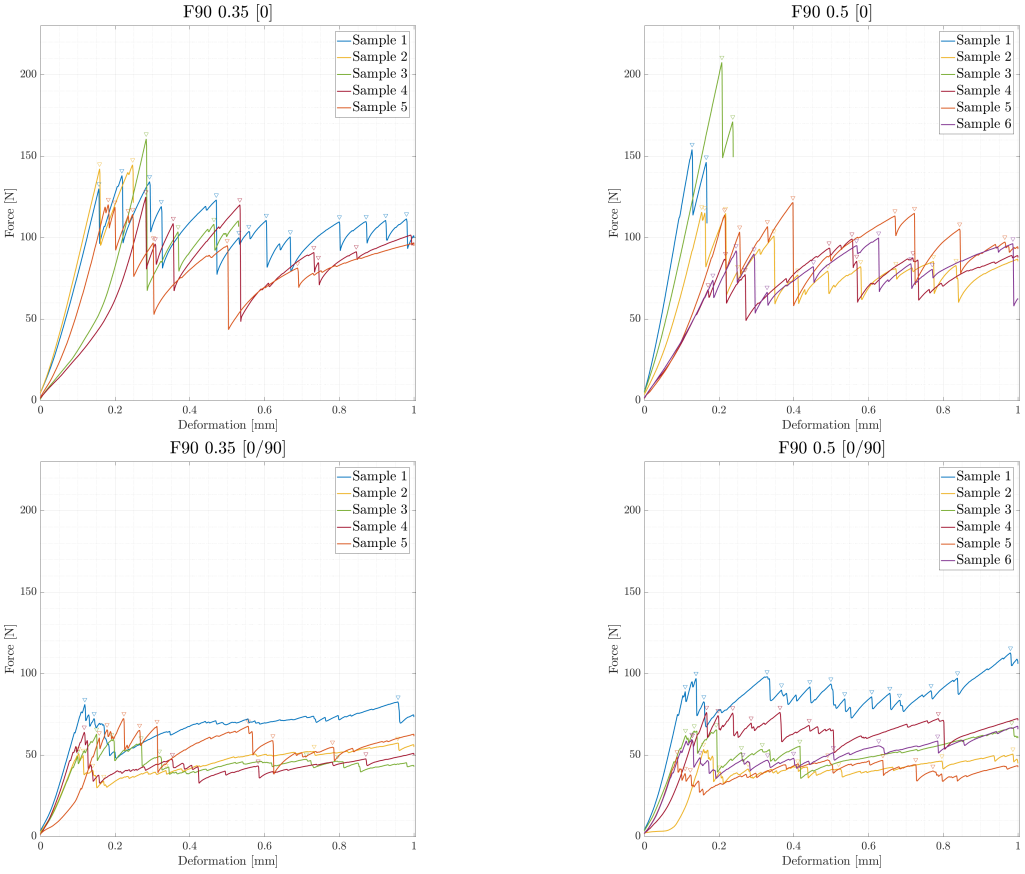

Figure C.11 – *Raw load-crosshead displacement curve for the F90 samples*

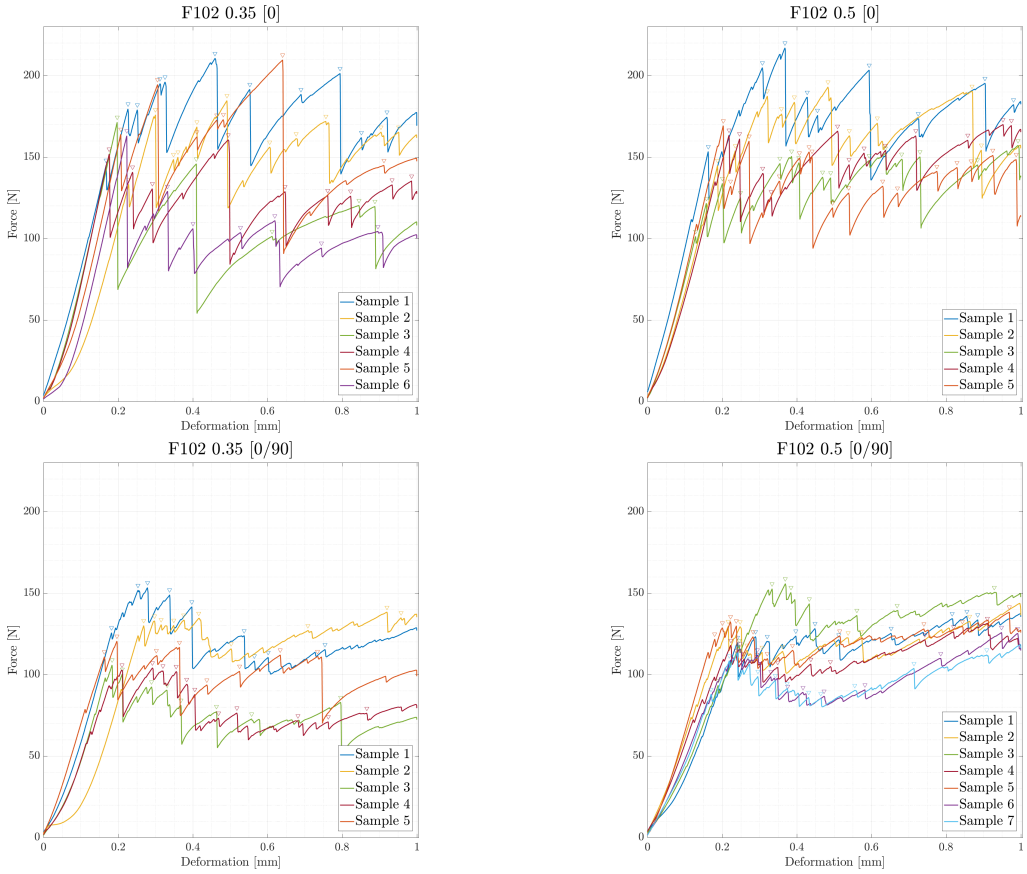

Figure C.12 – *Raw load-crosshead displacement curve for the F102 samples*

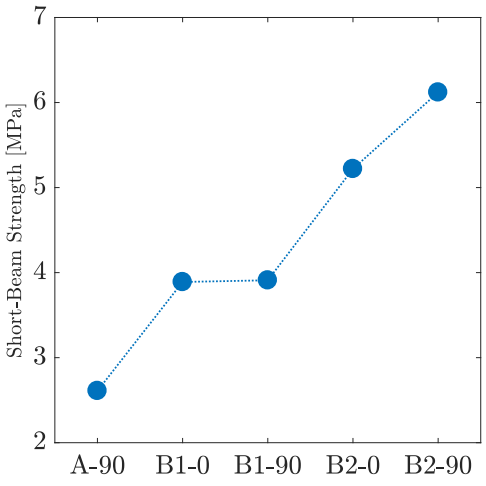

Figure C.13 – *Mean short-beam strength of samples according to their delamination type. Only samples displaying one delamination type are taken into account.*

	F80		F85		F90		F102	
	0,35	0,5	0,35	0,5	0,35	0,5	0,35	0,5
A-0			5	1 3 5	4	1 5		
A-90	1 2 3 4 5	1 2 3 4 5 6 7	1 2 3 4 5	1 2 3 4 5	3 4 5	5		
B1-0					2 5	1 3 4 6		
B1-90				1 5	1 2	1 6		
B2-0		7					3 4 5	
B2-90		6 7		4		2	1 2	1 2 3 4 5 6 7

Table C.2 – *Distribution of delaminations according to extrusion multiplier and linewidth. Numbers represent the identification number of the corresponding sample in the column. Numbers appearing several times in the same column indicate that the corresponding sample delaminated in several manners.*

Specimen Identifier				SBS (MPa)	Normalized SBS (MPa/kg)	Delamination Type		
F80	0,35	90	1	2,42	8,30	A-90		
F80	0,35	90	2	1,88	5,92	A-90		
F80	0,35	90	3	3,01	11,27	A-90		
F80	0,35	90	4	3,00	9,52	A-90		
F80	0,35	90	5	3,34	11,13	A-90		
F85	0,35	90	1	1,77	5,01	N/A		
F85	0,35	90	2	1,66	4,79	A-90		
F85	0,35	90	3	2,73	8,27	A-90		
F85	0,35	90	4	2,63	7,80	A-90		
F85	0,35	90	5	2,16	6,65	A-90	A-0	
F90	0,35	90	1	3,91	10,42	B1-90		
F90	0,35	90	2	2,93	8,38	B1-90	B1-0	
F90	0,35	90	3	3,16	9,23	A-90		
F90	0,35	90	4	3,17	8,99	A-90	A-0	
F90	0,35	90	5	3,60	10,28	A-90	B1-0	
F102	0,35	90	1	7,21	18,74	B2-90		
F102	0,35	90	2	6,40	16,36	B2-90		
F102	0,35	90	3	4,91	12,79	B2-0		
F102	0,35	90	4	5,15	14,18	B2-0		
F102	0,35	90	5	5,61	14,96	B2-0		
F80	0,5	90	1	2,96	10,41	A-90		
F80	0,5	90	2	2,47	7,74	A-90		
F80	0,5	90	3	2,64	9,31	A-90		
F80	0,5	90	4	2,67	9,25	A-90		
F80	0,5	90	5	2,93	10,08	A-90		
F80	0,5	90	6	2,45	8,31	A-90	B2-90	
F80	0,5	90	7	4,34	14,48	A-90	B2-90	B2-0
F85	0,5	90	1	3,55	11,76	A-0	A-90	B1-90
F85	0,5	90	2	1,63	5,33	A-90		
F85	0,5	90	3	3,68	12,39	A-0	A-90	
F85	0,5	90	4	4,42	14,72	A-90	B2-90	
F85	0,5	90	5	2,15	7,40	A-0	A-90	B1-90
F85	0,5	90	6	3,40	11,53	N/A		
F90	0,5	90	1	6,22	16,95	A-0	B1-0	B1-90
F90	0,5	90	2	2,98	9,22	A-90	B2-90	
F90	0,5	90	3	3,69	11,37	B1-0		
F90	0,5	90	4	4,10	12,88	B1-0		
F90	0,5	90	5	2,38	6,67	A-0	A-90	
F90	0,5	90	6	3,27	10,17	B1-0	B1-90	
F102	0,5	90	1	6,14	16,30	B2-90		
F102	0,5	90	2	6,33	16,91	B2-90		
F102	0,5	90	3	7,17	18,76	B2-90		
F102	0,5	90	4	6,59	18,54	B2-90		
F102	0,5	90	5	6,55	17,51	B2-90		
F102	0,5	90	6	6,41	18,64	B2-90		
F102	0,5	90	7	5,33	14,33	B2-90		

Table C.3 – *Each [0/90] specimen is labelled according to the classification in Table C.2. Short-Beam Strength and Normalized Short Beam Strength are also given.*

Bibliography

[1] S. Gantenbein, K. Masania, W. Woigk, J. P. W. Sesseg, T. A. Tervoort, and A. R. Studart, "Three-dimensional printing of hierarchical liquid-crystal-polymer structures", *Nature*, vol. 561, no. 7722, pp. 226–230, Sep. 2018, ISSN: 0028-0836.

[2] W. R. Burghardt, E. F. Brown, M. L. Auad, and J. A. Kornfield, "Molecular orientation of a commercial thermotropic liquid crystalline polymer in simple shear and complex flow", *Rheol Acta*, vol. 44, pp. 446–456, 2005.

[3] R. J. Young and P. A. Lovell, *Introduction to polymers*. CRC press, 2011.

[4] R. A. Chivers, J. Blackwell, and G. A. Gutierrez, "The structure of copoly(4-hydroxybenzoic acid/2-hydroxy-6-naphthoic acid): 2. An atomic model for the copolyester chain", *Polymer Papers*, vol. 25, no. 4, p. 435, 1983.

[5] T. S. Chung, M. Cheng, S. H. Goh, M. Jaffe, and G. W. Calundann, "Revisit the crystallization mechanism of vectra, a liquid crystal polymer", *Journal of Applied Polymer Science*, vol. 72, no. 9, pp. 1139–1150, 1999, ISSN: 00218995.

[6] S. L. Kwolek, P. W. Morgan, and L. W. Gulrich, "Synthesis, anisotropic solutions, and fibers of poly (1, 4-benzamide)", *Macromolecules*, vol. 10, no. 6, pp. 1390–1396, 1977.

[7] T.-S. Chung, S.-X. Cheng, and M. Jaffe, "Introduction to Liquid Crystalline Materials", in *Thermotropic Liquid Crystal Polymers: Thin-film Polymerization, Characterization, Blends, and Applications*, CRC Press, Lancaster, Pa: Technomic Pub. Co., 2001, pp. 1–18, ISBN: 1-56676-943-4.

[8] B. Wunderlich and J. Grebowicz, "Thermotropic mesophases and mesophase transitions of linear, flexible macromolecules", in *Liquid Crystal Polymers II/III. Advances in Polymer Science, vol 60/61*, Springer, Berlin, Heidelberg, 1984, pp. 1–59.

[9] E. M. Antipov, S. D. Artamonova, I. A. Volegova, Y. K. Godovksy, M. Stamm, and E. W. Fischer, "Temperature Evolution of the Structure of Liquid-Crystalline Main-Chain Copolyesters", in *Liquid-Crystalline Polymer Systems*, A. Isayev, T. Kyu, and S. Z. D. Cheng, Eds., ACS Symposium Series, Vol. 632, 1996, ch. 17, pp. 259–303.

[10] G. D. Butzbach, J. H. Wendorff, and H. J. Zimmermann, "Structure formation in a rigid chain polymer", *Macromolecular Rapid Communications*, vol. 827, pp. 821–827, 1985.

[11] S. Z. D. Cheng, "Kinetics of Mesophase Transitions in Thermotropic Copolyesters. 1. Calorimetric Study", Tech. Rep., 1988, pp. 2475–2484.

[12] W. Wang, G. Lieser, and G. Wegner, "Lyotropic liquid crystals of a soluble polydiacetylene. A comparative investigation by means of optical and electron microscopy", *Liquid Crystals*, vol. 15, no. 1, pp. 1–24, 1993, ISSN: 1366-5855.

[13] Celanese, "Vectra LCP Design Guide", Tech. Rep. VC-7R3_LCP-020_VectraLCPDesignGuideBro_AM_0613, 2013. [Online]. Available: https://www.celanese.com/-/media/Engineered%20Materials/Files/Product%20Technical%20Guides/LCP-027_VectraLCPDesignGuideTG_AM_0613.pdf.

[14] C. Houriet, *Online Appendix of the present thesis*. [Online]. Available: https://osf.io/p8h5t/?view%7B%5C_%7Donly=37810fc2ab5a4fb285faf100a7a63d27.

[15] P. Pisitsak and R. Magaraphan, "Rheological, morphological, thermal, and mechanical properties of blends of vectra A950 and poly(trimethylene terephthalate): A study on a high-viscosity-ratio system", *Polymer Testing*, vol. 28, no. 2, pp. 116–127, Apr. 2009, ISSN: 01429418.

[16] A. A. Mehmet-Alkan and J. N. Hay, "The crystallinity of poly(ether ether ketone)", *Polymer*, vol. 33, no. 16, pp. 3527–3530, 1992, ISSN: 00323861.

[17] F. Lederle, F. Meyer, G.-P. Brunotte, C. Kaldun, and E. G. Hübner, "Improved mechanical properties of 3D-printed parts by fused deposition modeling processed under the exclusion of oxygen", *Progress in Additive Manufacturing*, vol. 1,

[18] Y. Song, Y. Li, W. Song, K. Yee, K. Y. Lee, and V. L. Tagarielli, "Measurements of the mechanical response of unidirectional 3D-printed PLA", *Materials and Design*, vol. 123, pp. 154–164, Jun. 2017, ISSN: 18734197.

[19] K. Seo, "Rheology and Processing of Thermotropic Liquid Crystalline Polymers", in *Thermotropic Liquid Crystal Polymers: Thin-film Polymerization, Characterization, Blends, and Applications*, T.-S. Chung, Ed., CRC Press, Lancaster, Pa: Technomic Pub. Co., 2001, ch. 8, pp. 219–256, ISBN: 1-56676-943-4.

[20] S. M. Guskey and H. H. Winter, "Transient shear behavior of a thermotropic liquid crystalline polymer in the nematic state", *Journal of Rheology*, vol. 35, no. 6, p. 1191, 1991.

[21] S. Bakrani Balani, F. Chabert, V. Nassiet, and A. Cantarel, "Influence of the printing parameters on the stability of the deposited beads in fused filament fabrication of poly(lactic) acid", *Additive Manufacturing*, vol. 25, pp. 112–121, 2019.

[22] L. C. Sawyer, R. T. Chen, M. G. Jamieson, I. H. Musselman, and P. E. Russell, "The fibrillar hierarchy in liquid crystalline polymers", *Journal of Materials Science*, vol. 28, no. 1, pp. 225–238, 1993, ISSN: 0022-2461.

[23] B. Zülle, A. Demarmels, C. Plummer, T. Schneider, and H.-H. Kausch, "The morphology and tensile strength in filled and unfilled thermotropic liquid-crystalline polymer injection mouldings", *Journal of Materials Science Letters*, vol. 11, no. 21, pp. 1411–1413, 1992.

[24] L. C. Sawyer and M. Jaffe, "The structure of thermotropic copolyesters", *Journal of Materials Science*, vol. 21, no. 6, pp. 1897–1913, 1986, ISSN: 00222461.

[25] T. Weng, A. Hiltner, and E. Baer, "Hierarchical structure in a thermotropic liquid-crystalline copolyester", *Journal of Materials Science*, vol. 21, no. 3, pp. 744–750, 1986, ISSN: 00222461.

[26] C. J. Plummer, B. Zülle, A. Demarmels, and H. .-. Kausch, "The structure of filled and unfilled thermotropic liquid crystalline polymer injection moldings", *Journal of Applied Polymer Science*, vol. 48, no. 5, pp. 751–766, 1993, ISSN: 10974628.

[27] A. Kaito, M. Kyotani, and K. Nakayama, "Orientation distribution of liquid-crystalline polyester sheets studied by polarized infrared spectroscopy", *Journal of Polymer Science Part B: Polymer Physics*, vol. 31, no. 9, pp. 1099–1108, 1993, ISSN: 10990488.

[28] C. Liu and L. T. Manzione, "Process Studies in Precision Injection Molding. II: Morphology and Precision in Liquid Crystal Polymers", *Polymer Engineering & Science*, vol. 36, no. 1, pp. 10–14, 1996.

[29] T. J. White and D. J. Broer, "Programmable and adaptive mechanics with liquid crystal polymer networks and elastomers", *Nature Materials*, vol. 14, 2015.

[30] Y. Sawa, F. Ye, K. Urayama, T. Takigawa, V. Gimenez-Pinto, R. L. Selinger, and J. V. Selinger, "Shape selection of twist-nematic-elastomer ribbons", *Proceedings of the National Academy of Sciences of the United States of America*, vol. 108, no. 16, pp. 6364–6368, Apr. 2011, ISSN: 00278424.

[31] D. Cadogan, C. Sandy, and M. Grahne, "Development and Evaluation of the Mars Pathfinder Inflatable Airbag Landing System", *Acta Astronautica*, vol. 50, no. 10, pp. 633–640, 2002.

[32] H. Hoshiro, R. Endo, and F. Sloan, "Vectran: Super fiber from the thermotropic crystals of rigid-rod polymer", in *High-Performance and Specialty Fibers Concepts, Technology and Modern Applications of Man-Made Fibers for the Future*, The Society of Fiber Science and Technology, Japan, Tokyo: Springer Japan, 2016, ch. 10, pp. 171–190, ISBN: 978-4-431-55202-4.

[33] R. W. Gray IV, D. G. Baird, and J. Bøhn, "Thermoplastic Composites Reinforced With Long Fiber Thermotropic Liquid Crystalline Polymers for Fused Deposition Modeling", *Polymer Composites*, vol. 19, no. 4, pp. 383–394, 1998.

[34] R. W. Gray, D. G. Baird, and J. H. Bøhn, "Effects of processing conditions on short TLCP fiber reinforced FDM parts", *Rapid Prototyping Journal*, vol. 4, no. 1, pp. 14–25, 1998.

[35] C. Duty, J. Failla, S. Kim, T. Smith, J. Lindahl, and V. Kunc, "Z-Pinning approach for 3D printing mechanically isotropic materials", *Additive Manufacturing*, vol. 27, pp. 175–184, May 2019, ISSN: 22148604.

[36] B. N. Turner, R. Strong, and S. A. Gold, "Structural quality of parts processed by fused deposition", *Rapid Prototyping Journal*, vol. 20, no. 3, pp. 4–19, 2012.

[37] C. Bellehumeur, L. Li, Q. Sun, and P. Gu, "Modeling of Bond Formation Between Polymer Filaments in the Fused Deposition Modeling Process", *Journal of Manufacturing Processes*, vol. 6, no. 2, 2004.

[38] Q. Sun, G. M. Rizvi, C. T. Bellehumeur, and P. Gu, "Structural quality of parts processed by fused deposition", *Rapid Prototyping Journal*, vol. 14, no. 2, pp. 72–80, 2008.

[39] J. E. Seppala, S. Hoon Han, K. E. Hillgartner, C. S. Davis, and K. B. Migler, "Weld formation during material extrusion additive manufacturing", *Soft Matter*, vol. 13, no. 38, 2017, ISSN: 17446848.

[40] J. Yin, C. Lu, J. Fu, Y. Huang, and Y. Zheng, "Interfacial bonding during multi-material fused deposition modeling (FDM) process due to inter-molecular diffusion", *Materials & Design*, vol. 150, pp. 104–112, Jul. 2018, ISSN: 02641275.

[41] S. Costa, F. Duarte, and J. Covas, "Estimation of filament temperature and adhesion development in fused deposition techniques", *Journal of Materials Processing Technology*, vol. 245, pp. 167–179, Jul. 2017, ISSN: 09240136.

[42] A. K. Ravi, A. Deshpande, and K. H. Hsu, "An in-process laser localized pre-deposition heating approach to inter-layer bond strengthening in extrusion based polymer additive manufacturing", *Journal of Manufacturing Processes*, vol. 24, pp. 179–185, Oct. 2016, ISSN: 15266125.

[43] V. Kishore, C. Ajinjeru, A. Nycz, B. Post, J. Lindahl, V. Kunc, and C. Duty, "Infrared preheating to improve interlayer strength of big area additive manufacturing (BAAM) components", *Additive Manufacturing*, vol. 14, pp. 7–12, 2017.

[44] M. Spoerk, F. Arbeiter, H. Cajner, J. Sapkota, and C. Holzer, "Parametric optimization of intra- and inter-layer strengths in parts produced by extrusion-based additive manufacturing of poly(lactic acid)", *Journal of Applied Polymer Science*, vol. 134, no. 41, pp. 1–15, 2017, ISSN: 10974628.

[45] N. Aliheidari, J. Christ, R. Tripuraneni, S. Nadimpalli, and A. Ameli, "Interlayer adhesion and fracture resistance of polymers printed through melt extrusion additive manufacturing process", *Materials and Design*, vol. 156, pp. 351–361, Oct. 2018, ISSN: 18734197.

[46] M. A. Caminero, J. M. Chacón, I. García-Moreno, and J. M. Reverte, "Interlaminar bonding performance of 3D printed continuous fibre reinforced thermoplastic composites using fused deposition modelling", *Polymer Testing*, vol. 68, pp. 415–423, Jul. 2018, ISSN: 01429418.

[47] C. B. Sweeney, B. A. Lackey, M. J. Pospisil, T. C. Achee, V. K. Hicks, A. G. Moran, B. R. Teipel, M. A. Saed, and M. J. Green, "Welding of 3D-printed carbon nanotube-polymer composites by locally induced microwave heating", 2017.

[48] I. A. Malik, M. Mirkhalaf, and F. Barthelat, "Bio-inspired "jigsaw"-like interlocking sutures: Modeling, optimization, 3D printing and testing", *Journal of the Mechanics and Physics of Solids*, vol. 102, pp. 224–238, May 2017, ISSN: 00225096.

[49] M. Koziol, "Experimental study on the effect of stitch arrangement on mechanical performance of GFRP laminates manufactured on a basis of stitched preforms", *Journal of Composite Materials*, vol. 46, no. 9, pp. 1067–1078, May 2012, ISSN: 0021-9983.

[50] Z. Fan, M. H. Santare, and S. G. Advani, "Interlaminar shear strength of glass fiber reinforced epoxy composites enhanced with multi-walled carbon nanotubes", *Composites Part A: Applied Science and Manufacturing*, vol. 39, no. 3, pp. 540–554, Mar. 2008, ISSN: 1359835X.

[51] M. S. Islam and P. Prabhakar, "Interlaminar strengthening of multidirectional laminates using polymer additive manufacturing", *Materials and Design*, vol. 133, pp. 332–339, 2017.

[52] A. S. of Testing and Materials, "D2344M – Standard Test Method for Short-Beam Strength of Polymer Matrix Composite Materials and Their Laminates", 2006.

[53] *3D printing of Liquid Crystal Polymers: formation of interlayer features - YouTube*. [Online]. Available: https://www.youtube.com/watch?v=rmYYkqFYjIU&feature=youtu.be (visited on 11/28/2019).

[54] G. B. Mckenna, "Interlaminar Effects in Fiber-Reinforced Plastics-A Review", *Polymer-Plastics Technology and Engineering*, vol. 5, no. 1, pp. 23–53, 1975, ISSN: 1525-6111.

[55] S. Pimenta and P. Robinson, "An analytical shear-lag model for composites with 'brick-and-mortar' architecture considering non-linear matrix response and failure", *Composites Science and Technology*, vol. 104, pp. 111–124, Nov. 2014, ISSN: 02663538.

[56] M. Grossman, D. Pivovarov, F. Bouville, C. Dransfeld, K. Masania, and A. R. Studart, "Hierarchical Toughening of Nacre-Like Composites", *Advanced Functional Materials*, vol. 29, no. 9, pp. 1–9, 2019, ISSN: 16163028.